ABSTRACT

Title of Document: PERFORMANCE OF Ni/CEO_2/YSZ SOFC ANODES WITH CARBONACEOUS FUELS

Siddharth Patel, Master of Science, 2009

Directed By: Associate Professor, Dr. Gregory Jackson, Department of Mechanical Engineering

This study explores the impact of ceria incorporation into Ni/YSZ cermet anode support layers on the performance of button-cell solid oxide fuel cells operating with syngas and n-butane/steam fuel feeds. Ceria is incorporated into the porous anode support layer by co-firing ceria powders with NiO, YSZ, and graphite pore formers. Comparison of the performance with and without the co-fired ceria indicated improvements for operation with doped ceria for both syngas (by almost 20% higher power density) and direct n-butane/steam feeds (by over 25% higher power density). For initial cell performance, ceria addition to the support layer offered improved performance at high current densities with syngas suggesting that ceria may enhance water-gas-shift reactions and thereby increase H_2 availability for more effective electrochemical oxidation in the anode functional layer. For longer-term testing with direct-butane feeds, ceria doped cells not only showed better performance, but also indicated suppression of carbon deposition, thus improving long term operability. *Ex*

situ characterization of the ceria-doped anodes using SEM and Raman spectroscopy indicated that ceria addition helped the anodes maintain structural integrity.

To better understand experimental results, a previous through-the-MEA 1-D model has been updated and used with C-H-O microkinetics for Ni/YSZ anodes to characterize the experimentally observed cell performance. The model was enhanced to account for gas leakage through the electrolyte and to incorporate non-isothermal effects due to endothermic internal reforming and exothermic oxidation within the anode layers. Studies with internal methane reforming in a Ni/YSZ anode showed that the non-isothermal effects in 1-D button cell experiments are very small. This through-the-MEA model was used to fit experimental data and provided a basis for assessing key micro-structural parameters for the Ni/YSZ cells tested in this study. The model fits with syngas at various compositions provided a basis for assessing the most sensitive micro-structural parameters on the fuel cell performance such as anode support layer porosity and tortuosity.

PERFORMANCE OF Ni/CEO_2/YSZ SOFC ANODES WITH CARBONACEOUS FUELS

By

Siddharth Patel

Thesis submitted to the Faculty of the Graduate School of the
University of Maryland, College Park, in partial fulfillment
of the requirements for the degree of
Master of Science
2009

Advisory Committee:
Prof. Gregory Jackson, Chair
Prof. Christopher Cadou
Prof. Bao Yang

Dedication

For Ipshita

Acknowledgements

First and foremost, I would like to acknowledge Dr. Jackson for giving me an opportunity to come to this country and let me work in his group. Right from the start, he has mentored me on every step through my research. His easy personality and immense knowledge have not only guided me in completing my work, but made it possible to aspire for a career in this field. I thank him for making it a memorable and a great learning experience for me in this University and this country.

All my colleagues and friends in the SOFC and Ballard group deserve my deep gratitude for not only helping me in my research but making this office a great environment and a fun group. Steven and Paul deserve my sincerest thanks. Steven has not only helped me understand the modeling aspects of SOFC, but a significant part of this work builds upon the models that he created as part of his work. He has patiently answered all the questions that I have had in this regard. Paul introduced me to the experimental aspects of SOFC. His contribution in training me in aspects of manufacturing and setting up of SOFC experiments has made me take the protocols he painstakingly developed to the next level. It is thanks to him that I have been able to complete this work and pass on the knowledge to others who are to follow.

I want to mention Brian Eigenbrodt's contributions for doing Raman Spectroscopy analysis for my cells. His time and efforts have been very important in characterizing the cells. Jenny provided constant encouragement through her unique style and pep

talks. Ian helped out a lot for any equipment related issues from time to time. Atul, Josh, Chris and Anita, thank you all for your help and support.

I thank Dr. Cadou and Dr. Yang for graciously for taking time out and serving on my thesis defense committee. I thank Dr. Eichhorn and Dr. Walker for providing suggestions for improvement during SOFC group meetings. I graciously acknowledge the Petroleum Institute in Abu Dhabi for sponsoring this project. I thank Dr. Wen-An Chiou and especially Li-Chun Lai for assistance with SEM imaging in the NISP Lab. Dr. Zavalij deserves thanks for performing XRD studies which form a significant part of material characterization for this study.

Last but not the least; I must mention the constant support and encouragement that my parents provide me with. Without their belief in me, it would not have been possible to accomplish this task. Ipshita's constant encouragement and patient nature have helped me surpass difficult phases through my stay here. She is my source of inspiration. I can never thank these people enough.

Table of Contents

List of Tables

List of Figures

Chapter 1: Introduction to Solid Oxide Fuel Cells

1.1 Solid Oxide Fuel Cells

Solid oxide fuel cells (SOFCs) are energy efficient electrochemical devices that directly convert chemical energy of the fuel into electrical energy. This direct conversion can be much more efficient than conventional thermo-mechanical power generation technologies like internal combustion engines. Because of their high operating temperatures (≥ 700 °C), SOFCs, unlike low-temperature PEM fuel cells, have the ability to operate on a variety of fuel sources, including carbonaceous fuels. Gases such as carbon monoxide, methane, and other hydrocarbons that are poisonous to low-temperature PEM fuel cell anodes, can be a part of the fuel stream in an SOFC. SOFCs get their name from the solid electrolyte membrane made of a oxide-ion conducting ceramic, typically yttria stabilized zirconia (YSZ). The other main components of the SOFC are two porous electrodes – anode and cathode. Since the electrolyte pulls oxygen out of the cathode flow to the anode, SOFCs have the potential to produce concentrated CO_2 streams in anode exhaust, making them ideal for integration with carbon capture for large stationary plants.

SOFC-based power generation has been demonstrated over a wide range of applications: ~25 W portable devices for portable battery charges, to ~ 1 MW stationary power plants. Systems in the 1-5 kW are becoming commercially available for selected applications. The ability of SOFCs to facilitate internal fuel reforming for

carbonaceous fuels allows for the possible removal of the reformer used to break the hydrocarbon fuel into syngas.

SOFCs still face many challenges in the development of materials and reduction of costs to make them eligible for wide-scale commercialization. Sealing of fuel side feeds at high operating temperatures (> 700 °C) requires expensive and relatively inert materials with good matching of thermal expansion coefficients with fuel cell materials. Developing such seals with good performance and low cost remains a challenge [1]. Electrode and electrolyte materials with rapid-heating capabilities and minimal cracking would improve SOFC applicability for applications with numerous stop-start cycles. Another major issue is long term stability in performance of SOFC systems when operating on carbonaceous fuels or with fuels having impurities [2, 10-12]. Carbonaceous fuels can result in carbon deposition in the anode pores which deactivates the electrocatalyst and blocks the anode pores resulting in loss of performance.

SOFCs can produce power from gaseous hydrocarbons, such as oil well off-gases and furthermore because they pull the O_2 out of the air, SOFCs also provide a source of concentrated CO_2 for sequestration and/or enhanced oil recovery. The current study aims to explore fundamental issues in identifying preferred material combinations for durable SOFC anode operation with typical oil gas compositions characteristic of oil gases either with or without pre-reforming of the fuel stream. In addition, 1-D modeling of fuel cell performance has been carried out to assess SOFC membrane electrode assembly architectures for optimal operation with syngas.

1.2 Fundamentals of Solid Oxide Fuel Cells

1.2.1 Working of a SOFC

SOFCs are solid state devices that use an oxide ion-conducting ceramic material as the electrolyte. SOFC cells are composed of a membrane-electrode-assembly (MEA), which consists of the porous anode for fuel oxidation, dense oxide-ion conducting electrolyte, and porous cathode for O_2 reduction. A schematic of a SOFC MEA is shown below in Figure 1.1 with its components.

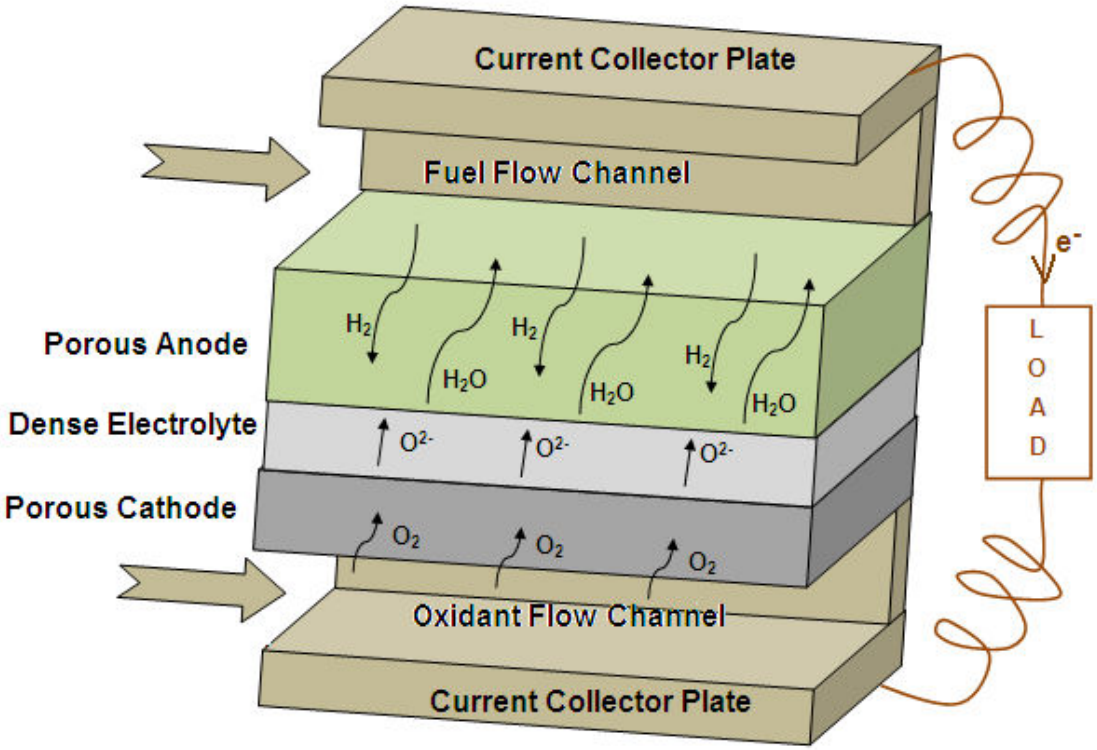

Figure1.1 A schematic of a SOFC showing the basic operation and its main components along with the flow channels and external electrical load.

Fuel and oxidant gases pass through the flow channels and diffuse through the respective electrodes. The electrodes are porous and loaded with electro-catalysts to

carry out the reactions necessary to produce electrical energy. The anode may also include other catalysts that promote internal reforming in the porous structure. On the cathode side, oxygen is converted to the negatively charged ion (O^{2-}) through an electro-catalyst which is then transferred from the cathode through the electrolyte to the anode as shown by Reaction 1.1. This oxide ion diffuses through the dense electrolyte to the anode where it combines with the fuel molecules to form final products as shown for H_2 in Reaction 1.2.

$$\frac{1}{2}O_2 + 2e^-_{ca} \rightarrow O^{2-}_{el} \qquad \text{(R1.1)}$$

$$H_{2(g),an} + O^{2-}_{el} \rightarrow H_2O_{(g),an} + 2e^-_{an} \qquad \text{(R1.2)}$$

Combining the two above reactions, a global reaction can be written for a SOFC as follows, where the subscripts indicate appropriate phases with '*an*' designating the anode, '*el'* the electrolyte, '*ca*' the cathode, and *(g)* the gas phase.

$$H_{2(g),an} + \frac{1}{2}O_{2(g),ca} \rightarrow H_2O_{(g),an} \qquad \text{(R1.3)}$$

In case the fuel happens to be a carbonaceous fuel, the global reaction is given as follows.

$$CO_{(g),an} + \frac{1}{2}O_{2(g),ca} \rightarrow CO_{2(g),an} \qquad \text{(R1.4)}$$

Planar MEAs are placed into a stack of cells that allow for electrons from one anode to flow up through a current collector plate with ribbed flow passages to the neighboring cathode. The outer anode provides electrons to an external circuit, performing electrical work on the load. These electrons re-enter the fuel cell through the outer cathode.

To study the effects of MEA micro-architecture, button cell geometry with a stagnation flow arrangement provides a useful configuration for making a 1-D configuration for readily correlating measurements to 1-D "through-the-MEA" models.

To understand the power production of the solid oxide fuel cell, the 'Gibbs free energy' G, of the gases must be accounted for. In the SOFC, *change* in this Gibbs free energy due to electrochemical oxidation of the fuel provides a basis for making voltage across the cell and providing the potential for making electrical power. The maximum voltage V_{rev}^{0} for a fuel cell is related to the change in G in Equation 1.1.

$$V_{rev}^{0} = \frac{G_{f,products} - G_{f,reactants}}{n_{el} * F} \qquad \text{(Eq. 1.1)}$$

where 'n_{el}' is the number of electrons released for each molecule of fuel reacted and F is Faraday's constant (96,485 C/gmol of electrons). If there are no irreversibilities in the fuel cell, then all this Gibbs free energy is converted into electrical energy.

The change in Gibbs free energy of formation in Equation 1.1 is a function of temperature T and partial pressures P_k of reactants and products as shown here in Equation 1.2:

$$\Delta G_f(T,P) = \Delta G_f^0(T) + \overline{R}T \ln\left(\prod_k (P_k^{\nu_k})\right) \qquad \text{(Eq. 1.2)}$$

In the above equation, ΔG_f^0 is the Gibbs free energy of formation at atmospheric pressure, $\overline{R}$ is the universal gas constant, and ν is the stoichiometric coefficient of species k (negative for reactants, positive for products). By inserting Equation 1.4 into 1.3, we can write the equation of OCV in its most commonly used form, known as the 'Nernst Equation'.

$$V_{rev} = -\frac{\Delta G_f^{\circ}(T)}{n_{el}F} + \frac{\overline{R}T}{n_{el}F} \ln\left[\prod_k P_k^{-\nu_k}\right] \qquad \text{(Eq. 1.3)}$$

V_{rev} is referred to as the 'Nernst Potential' and also as the thermodynamic open circuit voltage or OCV. For the H_2 oxidation reaction, the thermodynamic OCV is typically around 1.05 V at 800 ºC. The above equation assumes that the cell reactions occur reversibly. However, in actual cell operation, irreversibilities occur in reactions, and this makes the operating voltage typically less than the reversible voltage.

1.2.2 Voltage Losses in SOFCs

As current is drawn from the fuel cell, there are losses associated with the transport of reactants, the build-up of products, the conduction of ions and electrons, and the driving of the reactions in a forward direction. These losses are referred to as overpotentials. Activation overpotentials η_{act} are the voltage losses associated with driving the electrochemical (or charge transfer) reactions. Both the anode and the cathode contribute have activation overpotentials. Elementary charge-transfer reaction rates are governed by Butler-Volmer equation, given by Equation 1.4:

$$i = i_0 \left[\exp\left(\frac{\beta_f n_{el} F \eta_{act}}{\overline{R}T} \right) - \exp\left(\frac{-\beta_r n_{el} F \eta_{act}}{\overline{R}T} \right) \right] \qquad \text{(Eq1.4)}$$

In the above equation, i_o is the 'exchange current density' which is the equilibrium charge transfer rate in both the forward and the backward directions. β_f and β_r are the forward and reverse-reaction charge transfer coefficients. Raising the temperature of the cell reduces η_{act} by increasing the exchange current density [3]. More effective electrocatalysts, particularly for O_2 reduction, aid in reducing η_{act} as well. Increased surface area of the electrodes also aids in reducing activation loss.

A second type of voltage loss is the 'ohmic overpotential' that occurs due to the electrical resistance of the electrodes and also due to the resistance to the flow of oxide ions in the electrolyte. This loss is the least difficult to understand and the

easiest to model. Voltage drop due to electrical resistance is proportional to the current drawn from the cell.

$$\eta_{ohm} = i.R_{\text{bulk}} \qquad \text{(Eq. 1.5)}$$

Here, i is the external current density (Amps per geometric area of electrolyte membrane) and R_{bulk} is the area specific resistance (ASR). In the case of SOFCs, the greatest contribution to the ohmic overpotential comes from the oxide ion transport through the electrolyte. To minimize this kind of ohmic loss, electrodes should have high electron conductivities and even more importantly electrolytes must have high ionic conductivity. Ionic conductivity for electrolyte materials increases significantly with temperature, and this dependency governs SOFC operating temperatures (thus explaining why higher operating temperatures are advantageous for SOFCs). Thinner electrolyte membranes also help but too thin an electrolyte membrane can compromise the robustness of the cell.

The third overpotential associated with the SOFC is η_{conc}, which is related to the mass transport of gaseous species inside the electrodes. If the oxygen at the cathode of the fuel cell is supplied in the form of air, then it is evident that during the cell operation, there will be a slight reduction in the concentration of the oxygen in the region of the electrode, as the oxygen is extracted from the stream. This change in concentration causes a reduction in P_{O2}. On the anode side, there is a similar drop in partial pressure of the fuel gas (e.g., P_{H2}). In both cases, the reduction in reactant

partial pressures and increase in the product partial pressures results in the reduction in voltage as described by Nernst Equation (Equation 1.6)

$$V_{rev} = V_{rev}{}^{0} + \frac{\overline{R}T}{n_{el}F} \ln\left[\prod_k P_k^{-\nu_k}\right] \qquad \text{Eq. 1.6}$$

Partial pressures in Equation 1.6 are pressures inside the electrode functional layers. The reduction in V_{rev} from $V_{\text{rev}}{}^{0}$ can be accounted for as the transport overpotential in terms of η_{conc} given by Equation 1.7.

$$\eta_{\text{conc}} = \frac{\overline{R}T}{n_{el}F} \ln\left[1 - \frac{i}{i_l}\right] \qquad \text{Eq. 1.7}$$

Equation 1.7 gives the relation between concentration overpotential and a 'limiting current density i_l' at which the fuel is used up at a rate equal to its maximum supply rate. The current density cannot rise above this value, because the fuel cannot be supplied at a greater rate. This overpotential becomes dominant at higher current densities when the fuel and oxidant utilization becomes very high. It is also non-linear in nature like the activation overpotential. Increasing porosity and lowering tortuosity in porous electrodes can help reduce partial pressure drops for reactants coming into electrochemically active functional layer and reduce buildup of product partial

pressures in the anode functional layer. This can help reduce the concentration voltage loss to some extent. Equation 1.7 explains how the decrease in reactant partial pressure and increase in product partial pressure can reduce reversible cell voltage. First term in Equation 1.7 is called the EMF (electro motive force) of the cell. Figure 1.2 below gives an idea of how the different overpotentials affect the net operating voltage of the fuel cell.

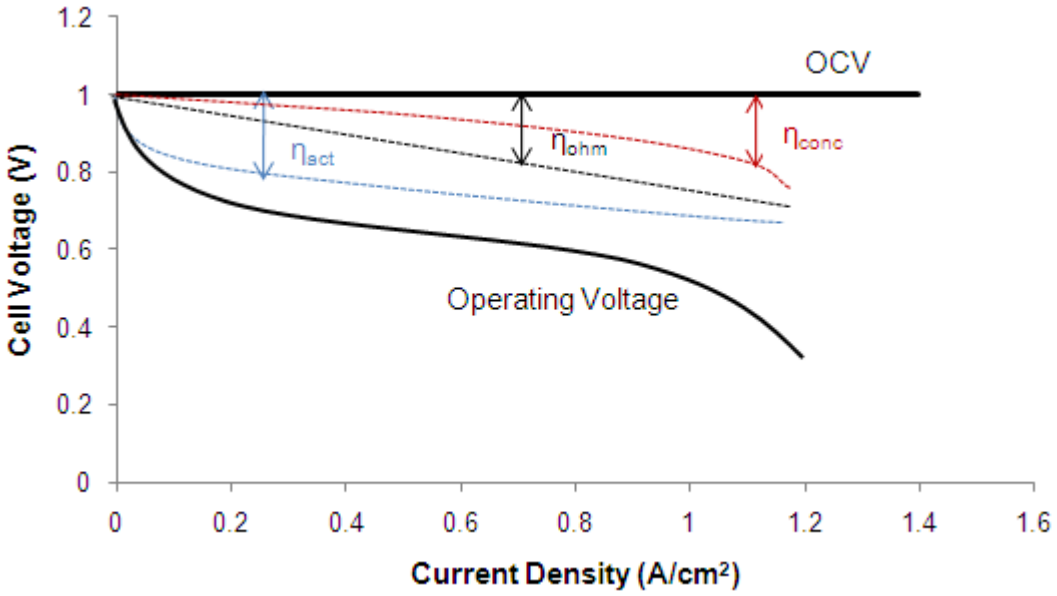

Figure 1.2 A typical *V-i* curve, with various sources of overpotential along with the OCV and the operating cell voltage.

Taking into account all the three overpotentials, the expression for the operating cell voltage is captured in Equation 1.8.

$$V_{cell} = V_{OCV} - \eta_{act} - \eta_{ohm} - \eta_{conc} \qquad \text{(Eq. 1.8)}$$

1.2.3 SOFC Components

The most common SOFC electrolyte material is zirconia doped with 8 to 10 mol % yttria, i.e., yttria-stabilized zirconia (YSZ). YSZ is highly stable in both the reducing and oxidizing environments found inside the two electrodes. The ability to conduct oxide ions is brought about by the fluorite crystal structure of zirconia in which some of the Zr^{4+} ions are replaced with the Y^{3+} thereby creating vacancies in the lattice. Oxide ion transport occurs between these vacancies located at tetrahedral sites in the perovskite lattice, as had been studies in detail at the atomic and molecular level [2]. The ionic conductivity of YSZ (0.02 S/cm at 800 °C and 0.1 S/cm at 1000 °C), and it can be made very thin ~10 μm to reduce ohmic losses and provide ASRs of 0.1 Ωcm^2.

A common anode material set is a Ni/YSZ cermet, often used in commercial SOFCs. The presence of YSZ provides mechanical stability to the anode along with minimizing the coefficient of thermal expansion (CTE) mismatch with the electrolyte. The anode support layer has porosity (30 – 50%) to allow for adequate gas transport of the reactant species to the electrolyte and also for the product gases to escape out to the channel flow. A functional layer is also used for the anode that is much thinner (20 μm) and has higher catalyst content with lower porosity (~ 25 %). In order to obtain high power densities from the SOFC, an anode supported design is typically followed, in which the anode acts as a 'support layer' with thickness around 1 mm. It should be noted that this is just one of the designs to make the MEA. There are electrolyte supported cells as well as cathode supported cells being studied by various groups with a variety of materials like gadolinium-doped ceria (GDC), yttrium doped

ceria (YDC) for anodes [19, 26] and lanthanum strontium cobalt ferrite (LSCF) for cathodes [26]. In this study, a small amount of ceria is added to improve the tolerance of the anode to temperature cycling and redox reactions. Ceria may also aid in reducing the deposition of carbon inside the anode gas diffusion layer (GDL) thereby preventing disintegration on prolonged exposure to carbonaceous fuels. Oxidation of fuel in the anode occurs through charge transfer reactions when gaseous species come in contact with the electro-catalyst and the electrolyte in a region called the three phase boundary (TPB). All three phases come in contact with each other here. This region must be very close to the electrolyte and this is typically called the 'functional layer' of the anode. It typically also has high nickel content in order to increase catalytic activity and is therefore less porous. An illustration of electrochemically active regions is given in Figure 1.3.

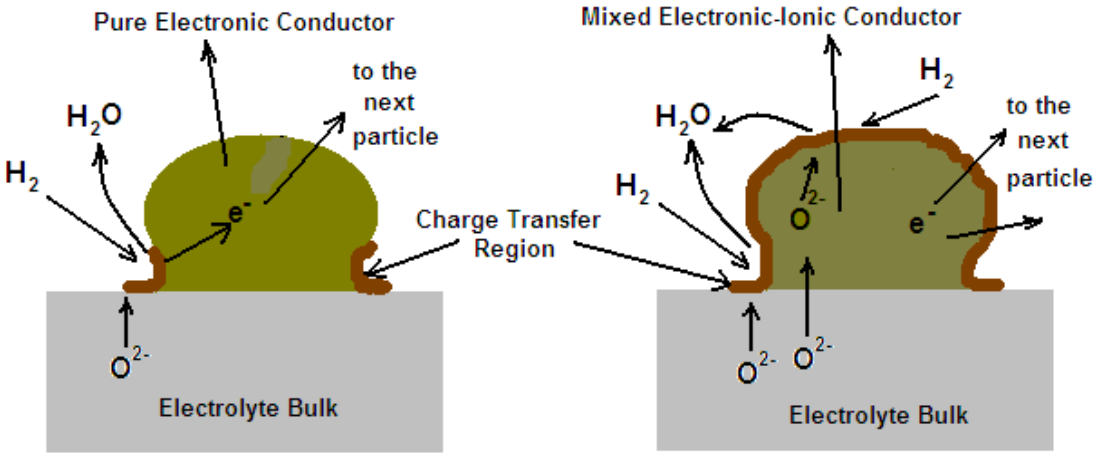

Figure 1.3 An illustration of the charge transfer region for: (a) pure electronic and (b) MEIC conductors. In case of pure electronic conductors, charge transfer reactions are restricted to a narrow three-phase-boundary (TPB) region where gas, catalyst, and

electrolyte interact. In MIEC catalysts, fuel oxidation can occur over the entire physical extent of the catalyst surface.

Nickel is a pure electronic conductor, and hence does not conduct oxide ions. This restricts the TPB region to a very narrow region by the Ni-electrolyte interface as shown in Figure 1.3a. Some oxides like ceria with multi-valent states can behave as mixed electronic ionic (MEIC) conductors and allow the electrochemical oxidation of fuels all over the surface area of the particle. This leads to a broad distribution of electrochemically active regions as illustrated in Figure 1.3b.

The cathode is also a porous structure in order to allow rapid mass transport of the oxidant to the electrolyte. A 50-50 mixture of strontium-doped lanthanum manganite ($La_{0.80}Sr_{0.20}$) MnO_3 and YSZ (LSM/YSZ) is used to make the cathode. This is a p-type semiconductor that has a perovskite structure exhibiting mixed ionic and electronic conductivity. There have been other materials proposed for SOFC cathodes like lanthanum strontium cobaltite (LSC) and lanthanum strontium ferrite (LSF) that operate better than LSM as they are mixed conductors, however their long term degradation and stability issues have caused problems.

1.3 Operation of SOFC s with carbonaceous fuels

As described in previous sections, SOFCs have the potential to be fuel-flexible on account of their high operating temperatures. Carbonaceous fuels like

syngas and lighter hydrocarbons can be fed directly into SOFCs. [10, 11, 12] Although conventional SOFC anodes are made up of Ni/YSZ due to low cost and high catalytic activity of nickel [13, 17], their use with carbonaceous fuels can have detrimental effects on performance and durability of the cells. Ni/YSZ anodes are prone to failure from sulfur poisoning [14, 15], and carbon deposition [10, 12, 16, 19].

For syngas and direct hydrocarbon fuel feeds, the following reactions are important to study in order to understand the effect on cell performance. Reaction 1.5 is called the 'water gas shift reaction' in which CO is transformed into H_2 upon reaction with steam.

$$CO_{(g)} + H_2O_{(g)} \Leftrightarrow CO_{2(g)} + H_{2(g)} \qquad \left[\Delta H = -\frac{41kJ}{mol}\right] \qquad \text{(R 1.5)}$$

The above reaction occurs in conjunction with the steam reforming. The thermodynamics of the water gas shift reaction is such that the higher temperature shifts the reaction to the left, thereby producing more carbon monoxide. It is this required to cool the product gas from the steam reformer and to pass it through a reactor containing catalyst, which promotes the shift reaction. A steam reformer running on natural gas and operating at atmospheric pressure with an outlet temperature of 800 °C produces a gas comprising some 60% hydrogen, 22% steam, 13% carbon monoxide, 5% carbon dioxide and traces of methane [11].

For direct hydrocarbon feed to the SOFC, reforming reaction can provide internal cooling of the fuel cell. In addition to reforming and water gas shift, the Boudouard reaction in Reaction 1.6 can occur particularly on Ni surfaces to encourage surface carbon build-up.

$$2CO_{(g)} \Leftrightarrow C_{(s)} + H_2O_{(g)} \qquad \text{(R 1.6)}$$

This reaction explains the formation of solid carbon, which is highly undesirable for an SOFC not just from performance point of view, but also from long term durability point of view [12, 17, 19-20].

Carbon formation can occur in several areas of the system where hot fuel gas is present. On more pathway of forming solid carbon is by way of pyrolysis of hydrocarbons. Natural gas, for example, will decompose when heated in the absence of air or steam at temperatures above about 650 °C. Solid carbon can deposit on the anode surface, thereby covering reforming and oxidation sites, reducing porosity, and negatively affecting cell durability. This carbon formation can clog pores and deactivate electrochemically active surface sites in the anode. Carbon formation can be mitigated by altering testing conditions. Lin et al. [18], for example, found that maintaining a high current density allowed for stable operation under methane. Low operating temperatures (<700 °C) also avoid carbon deposition as reported by Barnett et. al. [19], however, these conditions put severe constraints on the operation of an actual fuel cell application.

Higher hydrocarbons like n-butane can undergo pyrolysis readily in SOFC conditions [10]. To minimize this risk, steam is added to the fuel stream, and if the steam concentration is high enough, thermodynamic equilibrium will lean more heavily towards the formation of CO and H_2 via Reaction 1.5 than towards the formation of solid carbon via Reaction 1.6. In general, a steam/carbon ratio (*S/C*) of 2.0 to 3.0 is normally employed in steam reforming so that carbon deposition may be avoided with a margin of safety [17]. However, because steam is made through the electrochemical oxidation of H_2 in the SOFC anode, lower inlet *S/C* can be used in SOFC anodes. Steam also aids the reduction in coking is by carbon gasification reaction, given here in Reaction 1.7.

$$C_{(s)} + H_2O_{(g)} \Leftrightarrow CO_{(g)} + H_{2(g)} \qquad \text{(R 1.7)}$$

A syngas feed is created a product of external steam reforming outside of the fuel cell. Instead of directly exposing SOFC anodes to hydrocarbons and letting the cell reform the fuel internally, hydrocarbons can be reformed externally and the product gases (CO and H_2) fed to the cell. The advantages of external reforming are that the syngas products are more easily electrochemically oxidized in the cell than the parent hydrocarbons. Performance is better and coking is less of an issue, since the pyrolysis route can be avoided. However, the overall system complexity increases due to addition of extra components like reformer and costs go up.

With internal reforming, the reforming reactions are carried out within the SOFC anode. Product steam from the anode electrochemical reaction can be used for reforming hydrocarbons. In large scale systems, endothermic effect of steam reforming can help mitigate some of the issues of offsetting the heat of the electrochemical reaction thereby reducing sealing issues to some extent. Internal reforming usually results in loss of performance and increases the risk of coking.

Another problem that occurs with carbonaceous fuels is sulfur poisoning of the Ni/YSZ anode GDL [21 – 23]. Natural gas and petroleum liquids contain organic sulfur compounds that normally have to be removed before any further fuel processing can be carried out. Sulfur level as low as 2 ppm is detrimental to SOFC performance even at high operating temperatures [15]. With the use of novel materials like lanthanum strontium vanadate (LSV) [23] and doped strontium titanate doped with ceria [24], tolerance to sulfur can be significantly increased. CeO_2, a mixed ionic-electronic conductor (MIEC), has been shown to improve SOFC anode resistance to both carbon deposition and sulfur poisoning [25]. In traditional electro-catalysts, charge transfer reactions are restricted to a narrow three-phase-boundary (TPB) region where gas, catalyst, and electrolyte interact. In MIEC catalysts, fuel oxidation can occur over the entire physical extent of the catalyst surface.

1.4 Incorporation of cerium oxide in the SOFC anode

Several studies [12, 16, 17, 19, 20, 25-30] have shown that ceria-doped composite anodes in SOFCs can mitigate several challenges like carbon deposition

and sulfur poisoning faced by the conventional nickel based anodes when it comes to operating stably with carbonaceous fuels, particularly direct hydrocarbon feeds. In the context of direct utilization of available hydrocarbon fuels in SOFCs, the materials with mixed ionic and electronic conducting oxide may be desirable. Mixed conductivity extends the active zones that electrochemical reactions can occur by allowing O^{2-} ions to any position of interfaces between the anode and gas phase. The efficacy of CeO_2 based ceramics lies in the fact that exhibit mixed ionic and electronic conductivity in a reducing atmosphere due to reduction of Ce^{4+} to Ce^{3+}. Stimming and co-workers [26] have presented extensive review on alternative anode materials for SOFCs. It has also been reported that the ability of cerium to change its oxidation states in addition to good catalytic activity of CeO_2 based materials stems from the oxygen-vacancy formation and migration associated with reversible CeO_2–Ce_2O_3 transition [27, 28].

Ceria's electronic conductivity, however, is too low (~0.2 S/cm) to be able to use it as the sole current conductor. In this regard, efforts have been made to add a supplemental material that provides a lower resistance path for electrons. Research group at the University of Pennsylvania, by Gorte and coworkers [29, 30] has done extensive work in copper based ceria anodes. Their work focuses primarily on porous YSZ anode structures impregnated with Cu-CeO_2 mixtures, for use in the oxidation of hydrocarbons fed directly into the SOFC. The group has reported that Cu-YSZ is essentially inert to methane, and the addition of ceria to the anode gives rise to reasonable power densities and stable operation over a period of at least 3 days without deactivation due to carbon deposition.

Barnett and co-workers have investigated the use of composite SOFC anodes with various levels of gadolinium coped ceria (GDC), Ni, and Lanthanum Strontium Chromite (LSC). The results provide additional evidence on the stability of ceria-based anodes operating under a variety of hydrocarbons, including methane, ethane, propane, octane, and butane [31, 32]. Stable power densities have been demonstrated for all these fuels and in case of butane, for more than 400 hours of stable operation have been reported. The authors describe a SOFC design that combines a Ru-CeO_2 catalyst layer with a conventional Ni-YSZ anode that allows internal reforming of iso-octane without coking and yields stable power densities of 0.3 W/cm^2 to 0.6 W/cm^2 for operating temperatures in the range of 670 °C – 770 °C. Barnett and coworkers conclude that, while the catalytic activity of CeO_2 by itself is insufficient for HC reforming, especially at lower operating temperatures as corroborated by Gorte el. al.[12], its MIEC properties and tolerance to conventional sources of anode degradation coupled with modest catalytic activity make it an attractive candidate for inclusion in composite anodes [16].

1.5 SOFC Button Cell Modeling and Optimization of Electrode Microstructures

In a SOFC, several processes occur simultaneously: multi-component gas diffusion through porous electrode GDLs, chemical reactions of fuel and oxidant inside the porous electrodes, electrochemical reactions at the TPB, and ion transport through the electrolyte. In order to manufacture SOFCs for high power densities, it is imperative to understand the effect that the micro-structure of the electrode GDLs has on the cell performance along with the effect of thermo-kinetic parameters on

reaction rates that produce power in terms of current. Sophisticated models become critical to optimize the micro-architecture of the SOFCs. Recent computational efforts have improved the ability of physical models to predict performance for traditional Ni-YSZ anodes. A lot of work [33-38] has been done to develop models for capturing the influence of various parameters on SOFC cell performance.

Deutschmann and co-workers [33] have demonstrated a model with the capability to represent elementary heterogeneous chemical kinetics in the form of multistep reaction mechanisms. Goodwin et al. [34] have reported the need to understand thermodynamic models of TPB that describe the coupling of electrochemically active intermediates with gas phase reactants. Their model describes the behavior of various reaction pathways including hydrogen spillover, oxygen spillover, and interstitial hydrogen transfer. Many groups have come up with physical models that highlight the importance of anode microstructure [35-38], with some work aimed particularly at modeling direct internal reforming with methane inside an anode supported SOFC [35,36] that highlights the importance of electrochemical polarizations. Decaluwe et al. [38] have developed a one-dimensional button-cell model that couples porous-media gas transport and elementary electrochemical kinetics for a porous Ni–YSZ cermet anode, a dense YSZ electrolyte membrane, and a composite LSM–YSZ cathode. The effects of micro structural geometric factors have been borne out with respect to their overpotential contributions to the performance.

1.6 Objectives of the Present Study

The aim of this study is to develop SOFC micro-architectures for high power density applications with carbonaceous fuels, both reformate and direct n-butane feeds. It is an effort to investigate the efficacy of using ceria in the porous Ni-YSZ anode matrix in obtaining reasonable power densities with carbon-based fuels, especially direct internal reforming of n-butane without significant carbon deposition and associated degradation of performance and structural integrity of the anode. Another part of this study will focus on using one-dimensional model of the button cell to assess the effects of geometrical parameters like length of TPB, tortuosity, porosity and catalyst on the performance. The model includes porous media gas transport described by 'dusty gas model' along with detailed electro-chemistry involving surface reactions for both fuel and oxidant and charge transfer reactions at the TPB.

The reformate mixture of steam reformed n-butane was chosen to study the effect of ceria addition to the composite anode on cell performance. The motivation behind this study is to develop SOFC MEAs for oil well-off gas applications, where instead of flaring off the gases, they can be used as fuel feed for SOFCs. Many studies have looked into Ni/CeO_2 based anodes for operation on methane or reformed methane [12, 16-20, 25-30], but not much literature is available for butane or its reformed products. Some preliminary work has been done on Steam reforming of n-butane on Pd/ceria [41] but the cost of using palladium as the electro-catalyst, especially in large scale systems, rules out its commercial use. Another study shows the use a small-scale SOFC system running on internally reformed butane fuel [42].

Although the study concluded that butane partially oxidizes in the presence of the CeO_2/Ni /YSZ anode and gives rise to a gas mixture suitable for the fuel cell, it was found that steam reforming of butane is inadequate for the operation of micro-tube SOFCs.

Optimum anode architectures derived from a previous study by Jawlik [4] will be tested and comparison will be made between Ni/YSZ and Ni/CeO_2/YSZ anodes with regard to their operation with syngas and n-butane fuel feeds. CeO_2 will be introduced into Ni/YSZ anode support layer using the co-firing method, explained in more detail in Chapter 3. Co-firing involves mixing CeO_2 with nickel and YSZ during early stages of fabrication. It has been reported [43] that sintering ceria at very high temperatures can results in deactivation of its catalytic activity, yet at the same time it is important that the YSZ electrolyte be densified at high temperatures in order to eliminate grain boundaries and to reduce 'pin holes' or pores through which oxygen can diffuse as gas. A balance has to be struck in terms of sintering of the electrolyte and the anode support. Performance of Ni/CeO_2/YSZ anodes made with co-firing method will be compared to a baseline Ni/YSZ anode, also made with the same technique. The two types of cells will be exposed first to syngas reformate characteristic of a reformed butane mixture for a steam to carbon ratio of 1.5 at near equilibrium conditions at 800 °C. The experiments will aim at evaluating performance effects of adding CeO_2 to Ni/YSZ cells in terms of its long stability on exposure to direct butane feed and also how ceria minimizes carbon deposition that can be detrimental to anode structural integrity, as will be borne out by similar studies

on Ni-YSZ cell. The effect of ceria will also be corroborated with material characterization by way of Raman Spectroscopy and X-Ray Diffraction studies.

In the chapters that follow, fabrication and experimental testing along with analysis of different MEA architectures is given with an emphasis on variation in the anode structure and materials. Chapter 2 deals with the fabrication of both Ni-YSZ and Ni-CeO_2-YSZ cells along with the experimental setup required to test these cells for various conditions that are explained in Chapter 3. The performance curves bases on LSV and EIS measurements are followed by long term stability testing for both types of cells. In what follows, material characterization has been done through Raman spectroscopy and X-Ray diffraction studies to help explain how ceria achieves higher power densities in case of direct hydrocarbon feed and the reasons for its long term stability are highlighted. Chapter 4 details the model and the performance results with H_2 and CO electrochemical oxidation on anode-supported SOFCs with Ni-YSZ anodes operating on syngas. The model is validated against the experimental data presented in Chapter 3. Chapter 5 will present conclusions and recommendations for future research.

Chapter 2: Fabrication of the Ni/YSZ and Ni/CeO_2/YSZ cells

Solid oxide fuel cell (SOFC) membrane electrode assemblies (MEAs) comprise three main components – anode, electrolyte and the cathode. Various methods were employed to make SOFC MEAs, and after comparing the durability of performance of MEAs from the different approaches, a protocol was developed in collaboration with Paul Jawlik [4] that produces cells with repeatable micro-architecture for acceptable power densities. This method follows that of other previous studies in which all anode components and layers are co-fired in making the anode which provides structural support for the MEA [5-7]. This work incorporated ceria into the anode support layer following the work of Jawlik at the University of Maryland. The ceria was co-fired with traditional Ni/YSZ materials in order to form a support layer that was expected to provide improved resistance to carbon deposition in accordance with work by Gorte and co-workers [12, 20, 25, 29]. Because this study focused on variation in anode microstructure and performance, critical attention was focused on creating high activity anodes with both a support and functional layer as promoted in other studies by Zhao, Virkar and Jiang [39, 64]. In the current study, a functional layer on the anode side with relatively low porosity and high concentrations of both electrocatalyst and electrolyte provided improved performance. A higher porosity anode support layer enabled good transport of fuel to and products away from the high activity functional layer to promote electrochemical oxidation of fuels. Methods for introducing ceria into the anode support layer were also investigated in the literature [8-9] and a protocol for CeO_2 addition to the support layer was also developed to enable comparison between Ni/YSZ and Ni/CeO_2/YSZ cells.

2.1 Cell Geometry & Microstructure

The cells that were made as a part of this study utilized 'button cell' geometry with the diameter of about 2.5 cm and an overall thickness of about1 mm. The following picture shows the schematic of the button cell geometry along with the cell components – electrodes, the electrolyte and the functional layer.

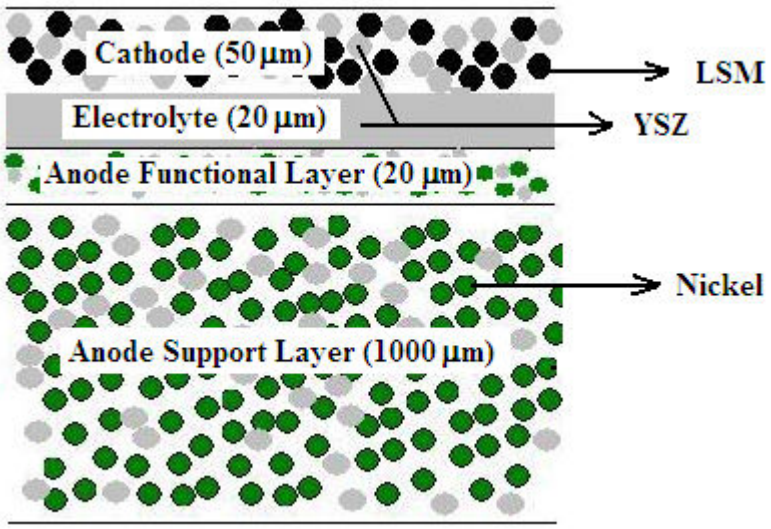

Figure 2.1: Schematic of cell geometry for a porous Ni/YSZ cell (not to scale)

The button cell MEAs tested in this study used anode-supported geometry with a (1000 µm ± 50 µm) thick support layer composed of a porous cermet of either Ni/CeO_2/YSZ or Ni/YSZ. A thin anode functional layer (~ 20-30 µm thick) composed of Ni/YSZ and a near fully-dense thin YSZ electrolyte (~ 10-20 µm thick). LSM-YSZ was chosen as the composite cathode material because of its stability and relatively

well-understood electrochemical behavior [46, 47], a composite that is used in most commercial SOFC development efforts. The cell fabrication processes were adopted and modified from methods described in earlier references [5-9]. Scanning electron microscopy (SEM of a cross-section of a typical Ni/YSZ in Figure 2.2.) reveals the MEA micro-structure.

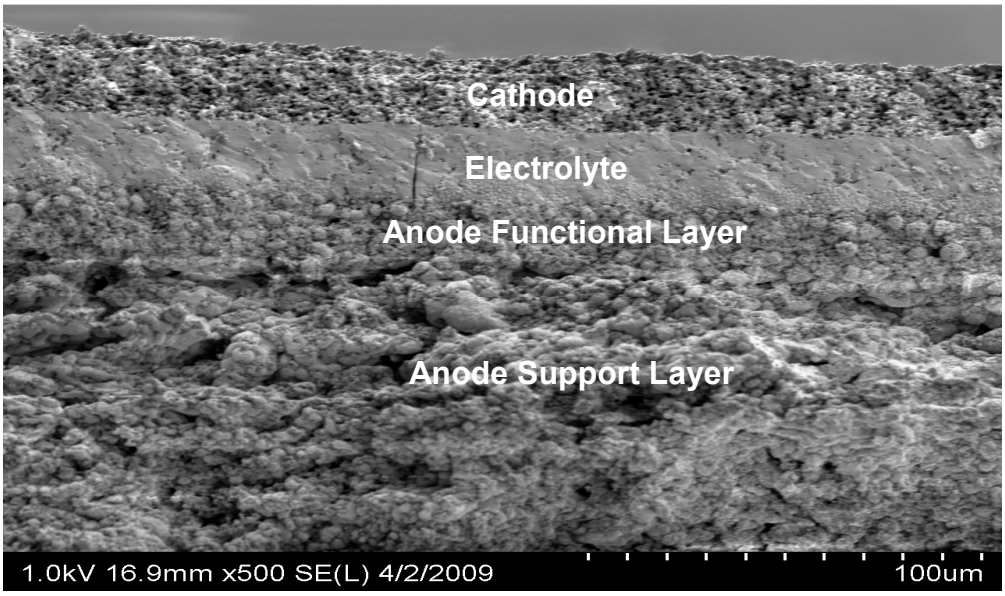

Figure 2.2: SEM Image of a reduced Ni/YSZ cell post testing.

2.2 Fabrication of Ni/YSZ Cells

The Ni/YSZ anode support layer was fabricated using NiO, YSZ, and graphite powders. 70% wt. Nickel (II) Oxide (Fisher Scientific, NiO) and 30% wt YSZ (Tosoh, $(Y_2O_3)_{0.08}(ZrO_2)_{0.92}$) were mixed in ethanol to create a slurry and ball milled for ~24 hours. Graphite powder (Timcal, 44μm average particle diameter) was then

added to compose 30% of the total solid by weight to act as a pore-former followed by further ball milling for a minimum of 4 hours. The slurry was then dried and passed through a 125 μm sieve to remove agglomerates. 2 gm worth of dried powder was then pressed for five to ten minutes at a pressure of at least 10 metric tons to form a ~3 cm diameter solid pellet with a thickness of about 1 mm. The pellets were then placed in a furnace and heated to 900°C over 10 hours and held there for 3 hours to burn out the graphite. The pellets cooled down to room temperature over 10 hours to form a porous anode support structure. During heating, the pellet tended to curl and become concave when viewed from top. In order to minimize the curling to maintain the planarity of the cells, porous alumina plates, each weighing about 6 to 6.5 gm, were placed on top.

After the graphite was burned off, the cells had an anode support layer with the porosity of 30%. This was not the final porosity of the support layer as the reduction of NiO to Ni during operation further increased porosity. Next step was to add the anode functional layer on the support layer. The powder for the functional layer was created in an analogous manner to that for the support layer only with a NiO:YSZ ratio of 6:4 instead of 7:3. The functional layer was intended for high catalytic activity to ensure fuel oxidation and hence the graphite pore-former was not added. The desired porosity of the functional layer was achieved through the reduction of NiO to Ni by H_2 feeds at high temperatures. After the powder was dried and sieved, it was ultrasonically dispersed in isopropanol using the sonicator for about 30 minutes. It was found that the powder did not dissolve in isopropanol. In order to ensure uniformity of the solution and prevent particle settling, a very small

quantity of polyvinyl-butyral (PVB) was added to the solution. This solution was then 'drop-coated' onto the anode support layer. Drop coating essentially meant pipetting the solution on to the anode support layer in a fixed amount to ensure the desired thickness of the functional layer and left to air dry for 20 minutes. This was followed by 10 minutes of drying under heat gun to ensure that isopropanol was evaporated. This resulted in a thin, uniform NiO/YSZ functional layer. Care was taken to mix the solvent, dispersant, and powder in appropriate ratios. Initial ratios were taken from Koh et al. [5] and adjusted as needed to give the best results. The appropriate quantities of powder, solvent, and dispersant for the functional layer are tabulated below in Table 2.1. The table also shows the quantities for electrolyte (also drop-coated) which was later added onto the support layer. After drying under heat gun, the cells were taken back to the furnace and were subjected to the same heating cycle as before for the support layer. This heating was done to ensure that there were no unnecessary remnants left onto the functional layer from the drop-coating process.

Table 2.1 Compositions used for drop-coating the functional layer and electrolyte per cell. (Note: Powder for the functional layer was a 60% NiO /40% YSZ by weight and for electrolyte was 100% YSZ)

Components	Isopropanol	Powder	PVB	Thickness
Functional Layer	700 µL	0.06 gm	0.010 gm	~ 20 µm
Electrolyte	700 µL	0.06 gm	0.015 gm	~20 µm

As for the electrolyte, the powder consisted of just the YSZ. The solution for drop-coating it onto the anode functional layer was prepared in a manner very similar to the functional layer. PVB was again added to the YSZ isopropanol solution to decrease particle settling thereby achieving a uniform solution. The solution was sonicated for 30 minutes and then drop-coated onto the cell. After drying out the isopropanol at room temperature, the cells were taken back to the furnace to sinter the dense electrolyte and the functional layer. The sintering cycle involved heating the cells from room temperature at a rate of 1°C/min. to 1450°C and holding them at 1450°C for 3 hours. The cells were cooled down to room temperature at 1°C/min. Exposure to such high temperatures resulted in the cells shrinking to about 80% of the original diameter. As the electrolyte tended to shrink more than the anode, cells without proper loads became concave when viewed with the electrolyte facing up. To prevent this, two alumina plates and one zirconia plate (total weight ~20 g) were stacked on top of the cell with one of the alumina plates placed directly on top of the electrolyte. Zirconia plates tended to stick to the electrolyte. As nickel-oxide reacts with alumina at these temperatures, cells were also placed NiO side down on top of zirconia plates.

After firing the electrolyte, the cathode was fabricated using a 50/50% by weight LSM/YSZ composite paste purchased from Fuel Cell Materials. The paste was attritor milled for 3 minutes with 10% graphite as pore-former. The average particle size for the graphite powder, purchased from Timcal, was 4 μm. This was done to increase the porosity of the cathode paste to ensure desired oxidant diffusion. 150 μL of isopropanol per gm of paste was added to decrease the viscosity. After attritor milling, the paste was slurry caste over a 9.5 mm circular opening on a 50 μm thick Kapton tape mask. The cathodes were dried under heat gun for 15 minutes before removing the mask. The cells were again put into the furnace to sinter the cathode to the electrolyte. The heating cycle consisted of heating the cells from room temperature to 400°C over a course of 21 hours and held for 1 hour. This was followed by heating to 1300°C over 15 hours with a dwell period of 1 hour, the cells were then cooled down to room temperature over 16 hours and 40 minutes. This process resulted in cathodes of thickness in the range of 50 μm ± 20 μm (with variation due to the uncertainty in slurry casting process).

Figure 2.1 shows a cross-section of the cell and Figure 2.3 shows the cathode side of the cell where the black 'button' is the 9.5 mm diameter cathode. The electrolyte extends all the way to the outer edge of the cell. Beneath the electrolyte in Figure 2.3 the anode appears green before it is reduced in a H_2 rich environment, when it turns grey. The active cell area is thus equal to the area of the cathode, which has the limiting area in all the three components.

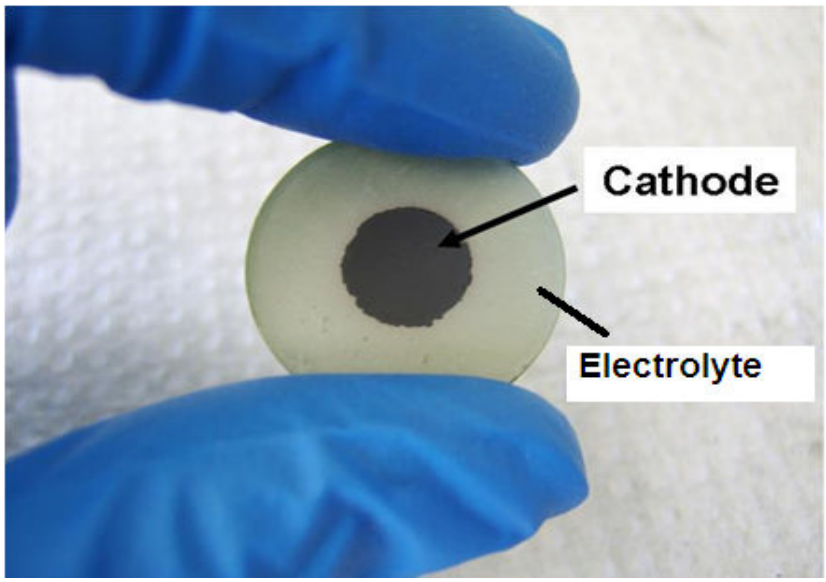

Figure 2.3: Photograph of a fully fabricated but unreduced cell. The electrolyte is transparent, making only the cathode and the anode visible**.**

2.3 Fabrication of Ni/CeO_2/YSZ Cells

Ceria was introduced in only the support layer for an alternative cell microstructure in hopes of demonstrating improved tolerance of carbonaceous fuels [25-30]. The ceria (Alfa Aesar, cerium (IV) oxide) was co-fired with Ni/YSZ while the graphite pore-former was burned out to form the porosity in the support layer. The powder for the support layer was made in an identical manner to the one for Ni/YSZ except that the percentage compositions by weight of various materials were as follows: NiO (65%), YSZ(25%), CeO_2(10%). The mixture was ball milled for 24 hours after adding isopropanol and later dried and sieved to create a fine powder. The cells were heated with the same cycle as the Ni/YSZ anodes to burn out the 30%

graphite pore-former to make a porous matrix. The functional layer for Ni/CeO_2/YSZ cells was made out of a 6:4 by weight ratio of NiO and YSZ without any ceria content in it. The electrolyte and the cathode were made in an identical manner as for the Ni/YSZ anode support. After firing the cells, and baking out the pore formers, anode porosities were estimated by first measuring the volume of a fully fabricated anode. The determined porosities for the anode functional layer using the volume measurement techniques were estimated to be around 60% for the cells discussed in this study.

After the fuel cell has undergone various cycles of heating and cooling for all of its components (anode, electrolyte and the cathode), its thickness and diameter are measured using a vernier caliper. The pellet is typically 1 mm thick (after subtracting the electrolyte and anode functional layer thicknesses of 20 μm each) and has an average diameter of 23 mm. This gives the anode support a volume of about 400 mm^3. Before the anode support undergoes calcinations to burn off the pore-formers, it contains 30% by weight of graphite. The pellet has a total weight of 2 gm. This gives the following weights of the various substances in the pellet: NiO – 0.98 gm, YSZ – 0.42 gm (after burning off 0.6 gm of carbon). Densities of Ni metal and YSZ at 25 °C are 8.9 gm/cm^3 and 6.1 gm/cm^3. It is important to note that during the cell operation, the anode support layer undergoes reduction (on exposure to H_2) and NiO gets reduced to nickel. Since the atomic weights of nickel and oxygen are 58.7 and 16 amu respectively, almost 78.6 % of NiO is nickel. After reduction, amount of nickel left in the support layer is 0.77 gm. Hence, the volumes occupied by nickel and YSZ can be calculated by dividing the masses of these substances by the respective densities and

added to get the total volume of 155 mm^3 occupied by the support layer matter. Hence, the porosity can be calculated by the following equation, and comes out to be ~ 61%.

$$\varphi_{\text{support layer}} = 1 - \frac{(\text{vol.of nickel} + \text{vol.of YSZ})}{\text{total volume of support layer}} \qquad \text{Eq. 4.21}$$

Current collection was done by attaching silver meshes (325 mesh) on top of both electrodes by pasting the meshes with silver paste. 1 mm silver wires were used to provide low lead resistance and pull the current out from the alumina tube structures. Table 2.2 below summarizes the amounts of substances in each layer of both Ni/YSZ and Ni/CeO_2/YSZ cells.

Table 2.2 – Compositions of various substances in both Ni/YSZ and Ni/CeO2/YSZ cells.

Materials	Ni/YSZ Cell			Ni/CeO_2/YSZ Cell		
Pre-Calcination	**Support Layer**	**AFL**	**Cathode**	**Support Layer**	**AFL**	**Cathode**
NiO	49%	60%	-	45.5%	60%	-
YSZ	21%	40%	50%	17.5%	40%	50%
CeO_2	-	-	-	7%	-	-
LSM			50%			50%
Pore-former	30%	-	10%	30%	-	10%
Post-Calcination	**Support Layer**	**AFL**	**Cathode**	**Support Layer**	**AFL**	**Cathode**
NiO	70%	60%	-	65%	60%	-
YSZ	30%	40%	50%	25%	40%	50%
CeO_2	-	-	-	10%	-	-
LSM			50%			50%
Porosity	61%	23%	26%	61%	23%	26%

Chapter 3: Experimental Setup and Cell Performance

The button cell MEAs were tested inside a clamshell furnace, which provided cell temperatures (T_{cell}) up to 800 °C in this study. Cells were mounted at the top of an outer cast Al_2O_3 tube and sealed using an Al_2O_3 paste (Cotronics) as exemplified by the call out photo in Figure XX. An Al_2O_3 inner tube concentric to the outer cast tube provided the anode feed flows in a stagnation flow arrangement and the anode exhaust returned along the annulus between the inner and outer tubes. For the cathode, a similar flow arrangement with an inner and outer tube was provided coming down to the cathode surface. Electrochemical measurements were taken including linear sweep voltammetry (LSV) and electrochemical impedance spectroscopy (EIS).

3.1 Cell Wiring and Rig Setup

Before putting the cells inside the furnace for testing, they were mounted onto cast alumina tubes (*AC Technologies, Cast Alumina Tubes*), and placed inside a clamshell furnace capable of heating to temperatures in excess of 800 °C. The range of temperatures for the testing was between 700 °C and 800 °C, which warranted the use of sealing material on the anode side. Sealing of the anode prevented the risk of fuel leakage and damages that could occur to the cell on account of direct fuel combustion with the surrounding air. Fuel and oxidant feeds were provided through a

series of mass flow controllers (Brooks 5850E), which were controlled and sense with a National Instruments data. Electrochemical testing was then performed to gain insight into the cell performance and fundamental behavior.

3.1.1 Cell Wiring and Current Collection

For effective current collection during cell operation, the cells needed to be wired up by pasting silver meshes onto both the electrode surfaces using silver paste (Fuel Cell Materials). This silver mesh (50 mesh, Alfa Aesar) was first spot welded to a current-collecting silver wire (~2 inches long, 0.5 mm in diameter) before pasting it onto the cell (Ag paste was applied in a similar manner as the cathode in chapter 2, hence the final thickness of the current collector was around 50 μm ± 20 μm) . The free end of the wire was then wound around a 1 mm diameter silver lead. The 1 mm diameter lead decreased ohmic resistance while measuring the current through the leads. However, spot-welding the thicker lead directly onto the mesh resulted in undue stress on the current collector and resulted in mesh delamination. Thus, a thinner more flexible wire (5 cm long and 0.5 mm in diameter) was attached to the mesh and then to the thicker lead allowing the stress to be minimized without adding significant resistance. The two wires were wound up together at their ends using the same Ag paste used to paste the mesh onto the cell surface and dried under a heat gun for 15 minutes. After pasting the mesh-wire assembly onto the cell, it was allowed to dry for 30 minutes. A dab of Al_2O_3 paste (Ceramabond 552-VFG, Aremco) was applied on the thin wire lead near the periphery of the mesh to further secure the mesh/wire assembly to the cell surface.

The current collector wiring was almost identical on both the anode and the cathode side except that in case of the anode, after the 0.5 mm wire was wound around the 1 mm wire (as seen in Figure 3.1 (b)), the wiring and mesh were fed through a cast alumina tube. The tube and wire were then vertically oriented and placed above the anode surface of the cell. The wire was then lowered down until the mesh, bent at a 90º angle, laid flat across the cell. The mesh was then pasted to the cell using the same methods used for pasting the cathode mesh by applying pressure onto it to ensure good adhesion. After drying, a small dab of Al_2O_3 paste was also applied to the wire to further secure it to the cell. This was done to further reduce the anode side lead resistance. The lead wire on the cathode side was threaded through Al_2O_3 tubing (Omega Engineering) for insulation.

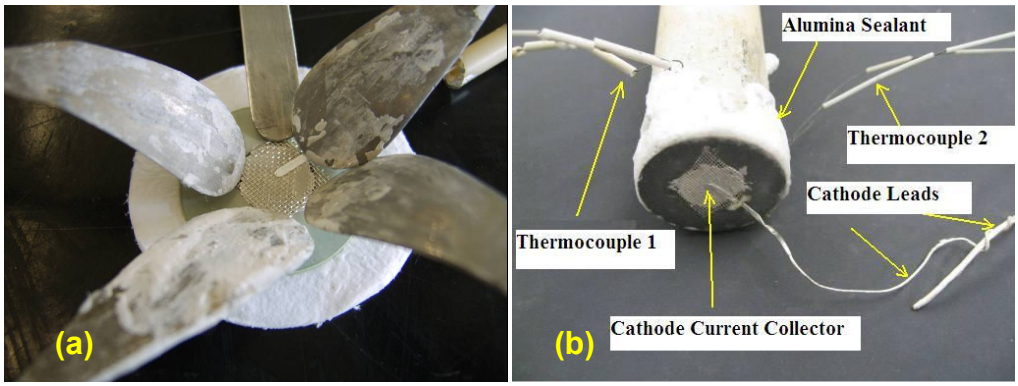

Figure 3.1: (a) Attaching the current collecting mesh to the cathode. (b) Cell-tube-assembly with current collector & thermocouples attached, ready to be mounted on rig.

3.1.2 Cell Mounting and Rig Assembly

After wiring, the cell was sealed onto the anode side alumina tube to prevent leakage during testing (Figure 3.1 (b)). At such high temperatures, it was necessary to prevent any direct contact of fuel with the surrounding air. For this purpose, the same ceramic paste sealant of Al_2O_3 paste was used that was also used to secure the mesh/wire assembly onto the cell. Sealing was done by applying several layers of the paste around the cell periphery and onto the outer alumina tube. The paste was allowed to dry for 30 min before moving the assembly to the testing rig. A gap of ~ 5 mm was left intentionally between the cell and the cathode side outer alumina tube to prevent contact after expansion due to the CTE mismatch between the tube material, the cell and the sealing paste. This allowed the cell and the tubes to expand without worrying about coming into contact and thereby preventing undue stress onto the cell which was known to cause cell failure by way of cracking the cell in some of the previous configurations investigated by Jawlik [4].

A narrow cast alumina tube was inserted inside the existing outer alumina tube on the anode aide. This tube supplied fuel to the cell surface. A rubber stopper attached at one end of the inner tube was wedged into the outer tube to create a seal and keep the inner tube in place. An additional Teflon tube (1/8" OD - Swagelok) was fed through the stopper to allow direct anode exhaust gases up to the exhaust vent in the fume hood in which the tests took place. A similar arrangement was utilized to deliver air on the cathode side.

A test rig supporting a clamshell furnace and properly aligned air and fuel tubes was used that was developed by Jawlik [4]. A picture of the rig assembly is

shown in Figure 3.2. The rig was kept in vertical configuration in such a way that anode feed tube was on the bottom and cathode on top. This allowed buoyancy effects to take the lighter fuel like H_2 upwards and spread over the surface of the cell. This configuration also allowed the tubes to be properly aligned so that the cathode tube was on top of the anode tube to ensure proper gas feeds to the cell. A small gap of approximately 1 mm was maintained between the outer anode tube and the MEA surface so as to reduce the impact of the CTE mismatch between the cell, the tube and the sealing material. K-type thermocouples placed on the cathode and the outer anode feed base tube were used to monitor the temperature of the cell during operation.

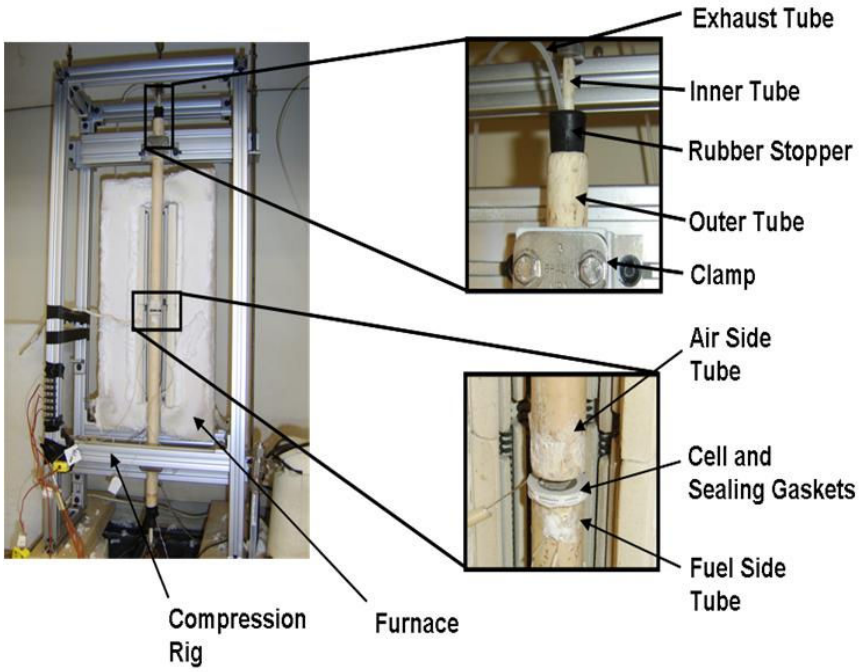

Figure 3.2: Photographic image of single-cell SOFC test rig showing the furnace and the spring loaded compression of the feed tubes, the feed tube configuration, and the mounted cell sealed to the outer anode feed tube.

The tubes were clamped onto the rig using Teflon clamps to ensure that the tubes stayed aligned in place during testing. Two K-type thermocouples were placed inside the furnace. One was used to control the heating and cooling of the furnace (TC1), the other (TC2) was used as a temperature check and for identifying temperature fluctuations characteristic of gas leaks. TC1 was pasted using alumina paste on the fuel side tube, just below the cell. TC2 was left free between the anode tube and heating element. Temperatures determined from TC1 are the reported temperatures in this study. The thermocouple wires were insulated with similar ceramic tubing as the electrical leads, but of a smaller diameter. The insulated thermocouple wires were then sandwiched in between the clamshell furnace. The furnace temperature was ramped up at a rate of 1 °C / minute to 800 °C from the room temperature using a temperature controller (*Athena, series 16C*).

3.1.3 Mass Flow Controllers

Fuel and air supply to the cell was controlled through a series of Brooks 5850E series mass flow controllers to achieve different partial pressures and test conditions for this study. These mass flow controllers were fed by compressed gas tanks. Anode gases were passed through a temperature-controlled humidifier (Fuel Cell Technologies) which utilized Nafion tubes to saturate the gas at the desired H_2O partial pressure. Signals to and from the mass flow controllers were routed to data acquisition boards (National Instruments SCXI system with PCI-6034 motherboard) which interfaced with Labview-based control software to allow for gas flow rate control and sensing of the mass-flow meter outputs and thermocouples. Flow rates to

each electrode were in the range of 300 to 400 sccm for the anode. The cathode feed was kept constant at 700 sccm dry air. This amounted to less than 3% O_2 utilization, which implied negligibly small gradients in O_2 concentration across the face of the cathode. A basic schematic of the flow configuration is shown in Figure 3.3.

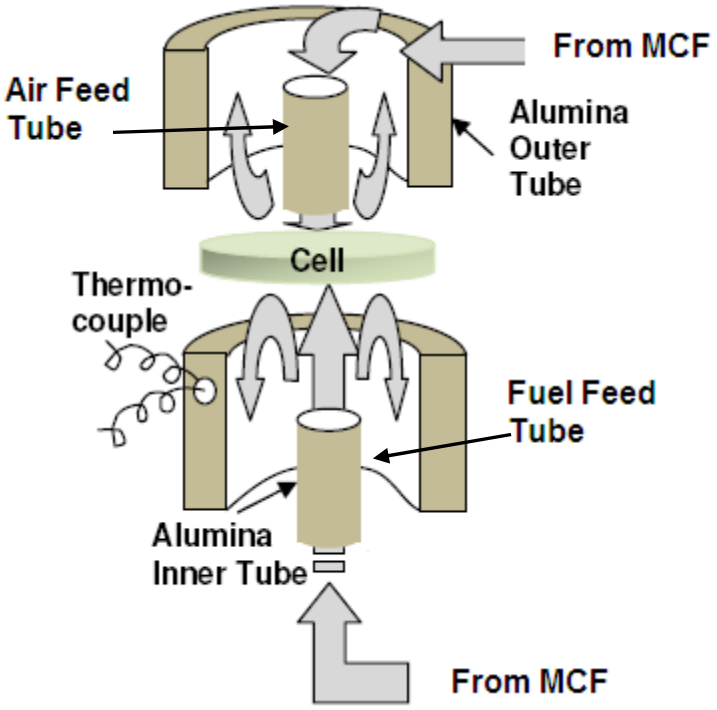

Figure 3.3: Schematic of the stagnation flow configuration for a button cell.

3.2 Electrochemical Testing Methods

After the rig assembly, the furnace temperature was programmed to ramp up to the desired temperature of 800 °C. While the cell was heating up, it was subjected to low H_2 flow (~10 sccm) overnight, so as to reduce the NiO to nickel. The current

collecting leads from both anode and cathode were connected to an electrochemical workbench (EcoChemie Autolab 30), which was utilized in a potentiostatic mode for all measurements including linear sweep voltammetry (LSV) and electrochemical impedance spectroscopy (EIS). EIS measurements were performed at a range of over-potentials determined by the voltage drop relative to the open-circuit voltage. Both the LSV and EIS tests were used to evaluate cell performance and to gain insight into the fundamental processes that determine cell behavior.

3.2.1 Linear Sweep Voltammetry

LSV measurements were performed from OCV (open-circuit voltage, typically ranging from 0.85 to 1.0 V) down to only 0.3 V to minimize risk of nickel oxidation in the anode functional layer. The cell voltage was decreased, starting from the OCV in steps at a set sampling rate. This voltage and the corresponding currents were recorded and plotted against one another to generate a *V*-*i* curve, where *i* is current density per area of cathode, which provided the limiting active geometric area of the cell. To get a better sense of cell performance and for comparison among different fuel conditions, the output power density ($V \cdot i$) was also plotted on the same graph. An example *V*-*i* curve with power density is shown in the Figure 3.4.

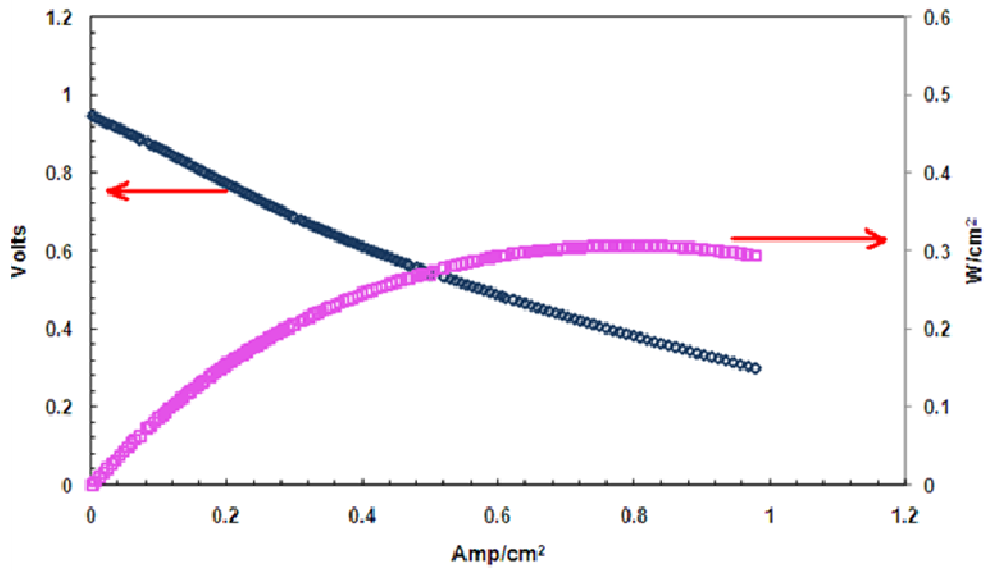

Figure3.4: *V-i* curve and power density of a Ni/YSZ cell operating on humidified H_2:Ar (1:1) with 3% H_2O at 800 °C.

3.2.2 Electrochemical Impedance Spectroscopy

EIS testing measures complex impedance of the cell over a range of voltage frequencies. Using Euler's Formula to express the sinusoidal voltage and current signals, impedance Z can be expressed as follows where Z_0 is the ratio between voltage and current amplitudes and φ is the phase difference between signals.

$$Z = Z_o\left(\cos(\phi) + i\sin(\phi)\right) \qquad \text{(Eq. 3.1)}$$

EIS measurements were performed from 10 kHz down to 0.1 Hz for a range of total MEA overpotentials. For SOFCs, the impedance always has a real component and for most frequencies also has an imaginary component. By plotting the real

component against the imaginary component for a range of voltage frequencies an impedance curve can be generated. A sample EIS curve is shown in Figure 3.5. The points corresponding to the high frequencies are on the left and the points corresponding to lower frequencies are on the right. For negative imaginary impedance values, current lags behind the voltage. Hence for SOFCs, conventionally the negative of the imaginary component is plotted instead of the actual value. Measurements of the high frequency intercept with the real axis for the impedance measurements provide a measure of the bulk resistance R_{bulk} of the electrolyte. It changes with overall current density and in general, R_{bulk} increases by as much as 10% with the highest current densities. This trend can be explained by the increased electrochemical utilization thickness with increased current density.

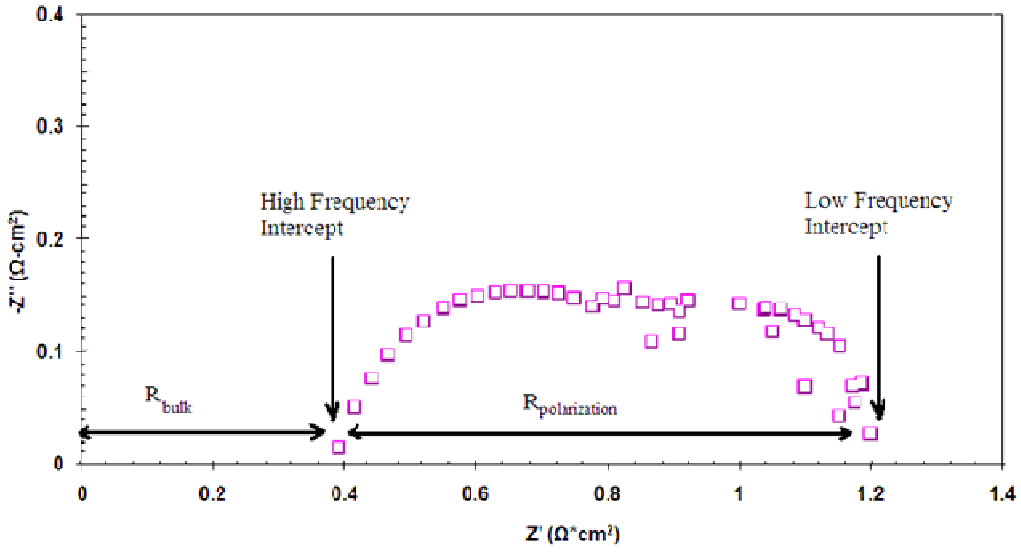

Figure 3.5: Sample Impedance curve of a Ni/CeO_2/YSZ cell operating under humidified H2:Ar (1:1) with 3% H_2O at 800 °C. High frequency intercept is an indicator of the bulk resistance of the cell.

EIS testing is a valuable tool because SOFC processes have a wide range of characteristic frequencies. Electron and O^{2-} ion conduction are very fast and provide the real impedance R_{bulk} at the highest frequencies. Thus, the high frequency intercept with the x-axis provides a measure of R_{bulk}. As the frequency is decreased from the high value of 10 kHz, the electrochemical and surface chemistry processes begin to impede current flow by both allowing charge to flow and to build up at the phase interfaces, in particular the 'three phase boundary' where charge transfer takes place. The low frequency intercept is therefore the total DC resistance, which includes the high frequency R_{bulk} and all resistances associated with surface chemistry, transport, and charge transfer processes, which summed to together are referred to as the polarization resistance, R_{pol}. R_{pol} depends strongly on cell microstructure and testing conditions, and it is difficult to definitively assign processes to certain frequencies or curve features. Some processes, however, can be associated with a range of frequencies. Charge transfer processes, for example, normally respond to high frequencies near 10 kHz while gas diffusion processes normally respond to lower frequencies.

Insight from the impedance spectra can be gained by changing the gas composition over one electrode while keeping it constant over the other. This is because the electrolyte behavior in SOFCs is largely independent of electrode conditions. Any resulting change in shape in the impedance curve can then be attributed to the electrode experiencing the changing fuel compositions. Varying the constant DC voltage about which the signal oscillates can also lead to changes in the

impedance curve. Nyquist plots reveal two dominant arcs – a smaller high frequency arc and a larger low frequency arc. Comparing impedance curves at very high overpotentials where transport losses become significant with impedance curves at very low overpotentials where activation losses are more significant, for example, can indicate frequencies over which gas diffusion or activation processes are most important.

3.2.3 Test conditions for fuel and air

After exposing the cell to H_2 flow diluted with Ar on the anode and air on the cathode side for over 12 hours, the flow rates for fuel and air were increase in steps over the course of 2 hours from ~ 10sccm H_2 and 100 sccm Ar to 200 sccm for both these gases. On the cathode side, air flow rate was simultaneously increased over the same time range from ~ 100 sccm to 700 sccm. Over the course of increasing the flow rates, when at 100 sccm H_2, the anode side gases were made to flow through the humidifier by switching the flow through the flow control valve and its temperature was set so as to flow 3% H_2O. Final conditions just prior to testing were at P_{H2} = 0.485 bar, P_{Ar} = 0.485 bar, and P_{H2O} = 0.03 bar. Overnight exposure made the cell reach an OCV in the range of ~ 0.83V. Over the course of increasing the flow rates, the OCV climbed up to ~0.95 V. It was made sure that NiO was fully reduced to Ni before starting the measurements. This was done by observing the increase in OCV and decrease in fluctuation of its value with fuel flow rate. After assuring that the OCV stabilized, the testing began.

LSV and EIS tests were performed for several gas compositions and for temperatures ranging from 700 to 800 ºC. The cells were first exposed to different anode gas compositions at 800 ºC. To compare the performance of reformate-fed fuel cells to direct-hydrocarbon-fed fuel cells, both syngas and butane/steam feeds were fed to the anode at different compositions. The cathode overpotentials were relatively constant for a fixed T_{cell} and current density i on account of low air utilization (~ 3%). For the anode feeds, syngas compositions were designed to match those for an equilibrium outlet of a steam reformer operating at 800 °C with n-butane (n-C_4H_{10}) fuel and a steam-to-carbon (S/C) ratio of 1.5. The syngas was then input at various degrees of H_2 and CO % conversion to simulate different locations down the channel of a planer SOFC cell. These syngas compositions (at 0, 25, and 50% conversion of H_2 and CO) are shown in Table 3.1. These compositions were compared against n-butane steam feeds directly to the cell at steam-to-carbon (S/C) ratios of 1.0 and 1.5. For the butane feeds the flows were diluted by 50% in Ar to facilitate humidification of the stream without butane flowing through the humidifier. In general, the anode flows were maintained between 300 and 400 sccm total flow and fuel conversion was generally well below 5% of the total flow such that the variations in gas concentrations at the outer anode interface were quite small.

Table 3.1 – Syngas and butane/steam feed compositions in bar for this study. For butane feeds, balance to 1 bar supplied by Ar.

	P_{H2}	P_{H2O}	P_{CO}	P_{CO2}	P_{C4H10}
syngas					
0% conv.	0.651	0.082	0.215	0.052	0.0
25% conv.	0.499	0.234	0.151	0.116	0.0
50% conv.	0.328	0.405	0.105	0.162	0.0
n-butane					
S/C = 1.0	0.0	0.400	0.0	0.0	0.100
S/C = 1.5	0.0	0.429	0.0	0.0	0.071

For all flows at 800 °C, at least two LSV tests were performed over a period of 30 minutes. In between the two LSV data sets, EIS tests were conducted at 100 and 300 mV overpotentials using the FRA (Frequency Response Analyzer) software. Since H_2 contributes little to the anode overpotential, the data for 3% H_2O (with H_2:Ar flow of 1:1 ratio) was important to isolate the cathode overpotential by fitting the experimental data with the model. Since the cathodes were made identical in all the cells, it provided a basis for isolating the anode overpotentials for various types of carbonaceous fuels tested later on. After recording the LSV and EIS data for H_2 with 3% water vapor, the flow conditions were shifter to match the 0% conversion syngas composition. The same procedure was used to record the data for LSV and EIS measurements as with the H_2 feeds after finishing the syngas testing for 0% and 25% conversion, the flow conditions were changed to n-butane on the anode side. The temperature of the humidifier was increased so as to ensure *S/C* = 1.5. The cell was kept under ~50 to 100 mV overpotential whenever there was a change in fuel flow

rate or fuel composition in between different test. This was done so as to maintain the transport of oxides through the electrolyte. After finishing tests for 800 ºC, the temperature was reduced to 700 ºC and the cell tested for the same flows. The cell was again heated back to 800 ºC at a rate of 1 ºC/min. It was then subjected to sustained exposure to n-butane for stability testing. This was necessary to study the effects of carbon deposition on the cell performance and structural integrity. It also formed the basis for comparison with the Ni/YSZ cell to show how CeO_2 addition aided in minimizing performance degradation. Upon completion of testing, the cell was cooled down at a rate of 1 ºC/min. Air was flown on the cathode side and a dilute H_2 mixture was flown on the anode side. H_2 was flown during cool down to ensure nickel remained in its reduced form. The apparatus was then inspected for faulty seals, proper tube alignment, and cell cracking. The cell was then removed and the microstructure explored using a Hitachi SU-70 scanning electron microscope (SEM). Additionally, elemental composition was characterized using energy-dispersive X-ray spectroscopy (EDX with Bruker XFlash Silicon Drift Detector). This was done to verify that the presence of desired materials in the appropriate locations. It also indicated the extent to which graphite, which was generated due to sustained exposure to carbonaceous fuels, especially due to steam reforming of n-butane, penetrated inside the anode GDL. More material characterization was done using Raman spectroscopy (Renishaw in-Via Raman microscope) and XRD (Bruker C2 Discover diffractometer) to further substantiate the claim that ceria does inhibit carbon deposition in the depths of the anode.

3.3 Performance of Ni/CeO_2/YSZ anodes (include repeatability of anode OP)

This section details the results obtained for the co-fired Ni/CeO_2/YSZ when operated upon using syngas and n-butane fuel feeds. Anode-supported MEAs with thin YSZ electrolytes (~ 10 μm thick) and LSM/YSZ functional cathode layers were tested for T_{cell} ranging from 700 to 800 °C on syngas for a variety of fuel conversions, and on n-butane with H_2O added at *S/C* = 1.5 and 1.0. The MEAs were characterized with LSV measurements and with EIS at total cell overpotentials (η_{tot}) between 100 and 300 mV.

The standard procedure was to test the cells first with H_2 and Ar in the ratio 1:1 in the anode with 3% H_2O. The anode overpotential due to H_2 was found to be negligible and the voltage losses were assumed to be made up of ohmic and cathode losses. This data, when fitted with the model gave a way to isolate the cathode overpotential. Since the cathode was fabricated using the same method each time, it provided a basis to subtract the cathode from the cell performance with syngas and n-butane to see the effect of fuels on anode overpotential.

After testing with 0% conversion syngas, 25% syngas and n-butane, the cell was then subjected to sustained n-butane flows for up-to 50 hours. This was done to assess the durability of the cell and its resistance towards carbon deposition. In order to assess the role of ceria in carbon suppression, similar durability testing was done on Ni/YSZ cells and the two performances were compared. The cells were then characterized by *ex* situ Raman Spectroscopy at room temperature conditions to explore the depth to which carbon penetrated the anode GDL in two types of cells.

The presence of cerium zirconates was substantiated by XRD studies on the Ni/CeO_2/YSZ anode support layer. SEM and EDAX analysis further showed the difference in micro-architecture for the two types of cells.

3.3.1 Initial Testing With Hydrogen

The cell was tested with P_{H2} = 0.485 bar, P_{Ar} = 0.485 bar and P_{H2O} = 0.03 bar flow conditions on the anode with ~700 sccm of air on the cathode. This formed the baseline case to be used later for isolating the cathode overpotentials. The following figure shows the V-I curve and impedance data for this case. The electrolyte thickness was kept at ~20 µm for most of the cells to allow for comparison with Ni/YSZ cells.

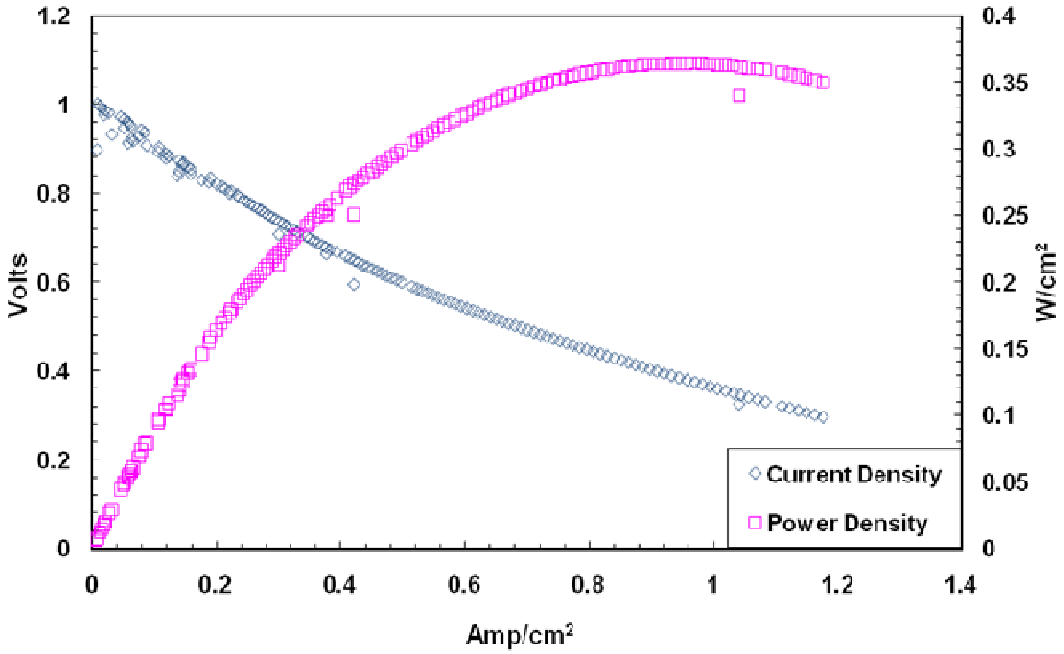

Figure 3.6 *V-i* curve and power density of a Ni/CeO_2/YSZ cell operating on humidified H_2:Ar (1:1) with 3% H_2O at 800 °C.

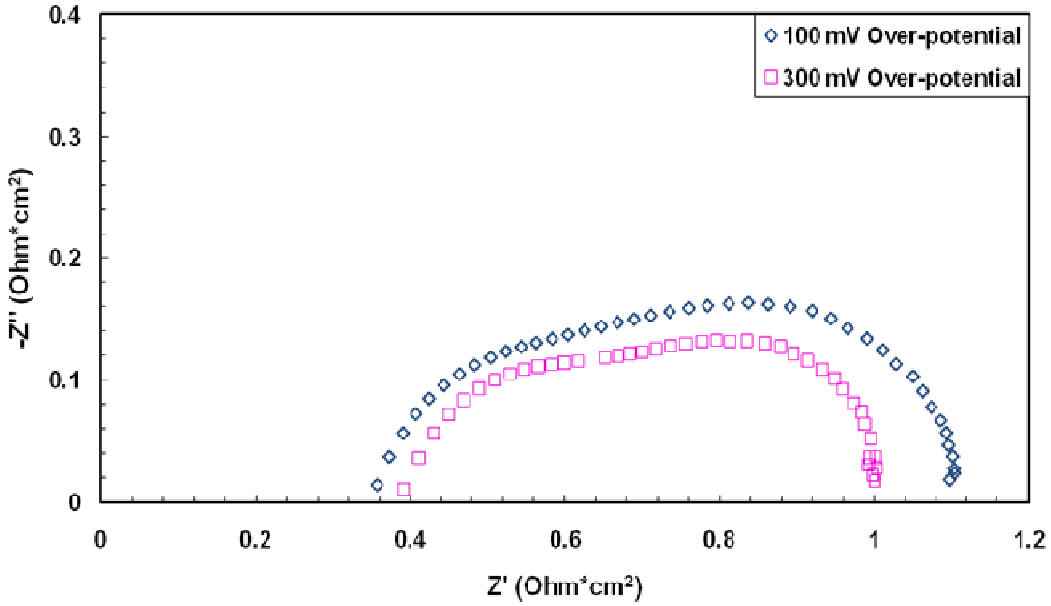

Figure 3.7 Impedance data for Ni/CeO_2/YSZ cell operating on humidified H_2:Ar (1:1) with 3% H_2O at 800 °C. Data shown for two overpotential values of 100mV and 300mV less than OCV.

The open circuit voltage for the cell was ~ 1.014 V and the maximum power density obtained for the baseline case was 0.36 W/cm^2. EIS measurement showed the presence of a high frequency and a low frequency arc. The measurement was done for two different total cell overpotentials, 100 and 300 mV. The high frequency R_{bulk} intercept for the 300 mV case (0.38 Ω·-cm^2) was 10% higher than for the 100 mV case (0.35 Ω·-cm^2). The increase in bulk resistance with the increase in current density has been borne out from simulation work by Decaluwe et.al. [38] and with experiments by Zhao and Virkar [39], who showed that the oxide ions travel further distances through the anode or cathode bulk at higher current densities. Polarization

resistance for 100mV case is ~ 0.75 Ω·-cm^2 and that for 300 mV case is ~ 0.62 Ω·-cm^2.

3.3.2 Testing With Carbonaceous Fuels – Syngas

After testing the cells for baseline wet H_2 case, cells were exposed to syngas. As explained in Chapter 2, two different syngas compositions were tested. First, 0% syngas case was tested followed by 25% and 50% case. Tests were also conducted at different temperatures to study the effect of temperature on cell performance. Syngas performance is shown in the Figure 3.8 below.

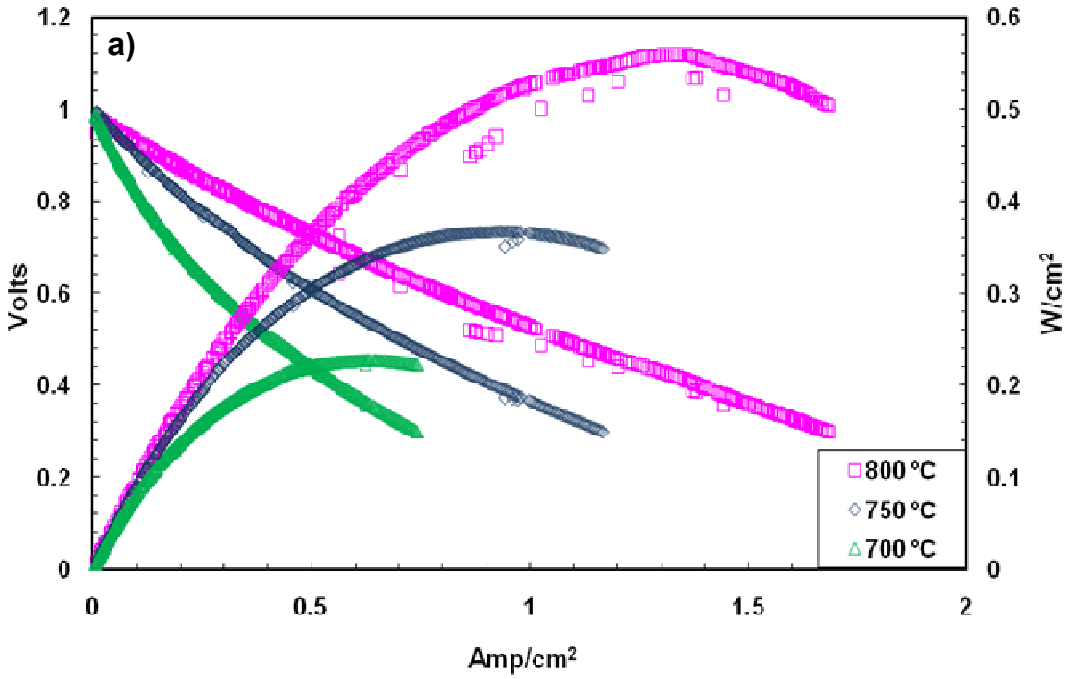

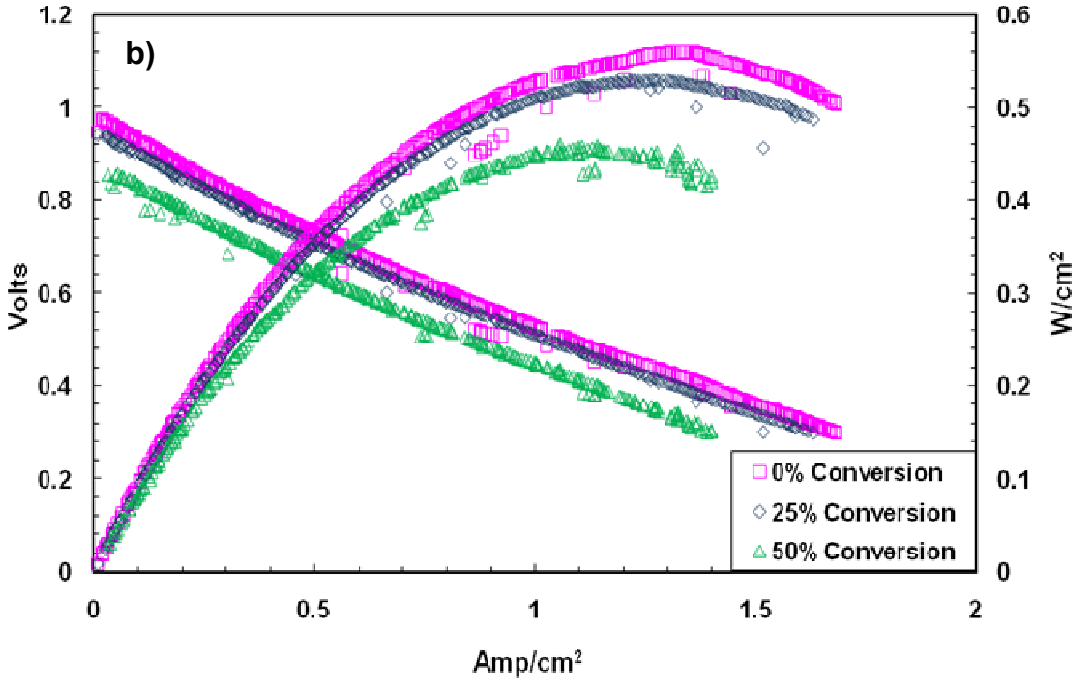

Figure 3.8 *V-i* curve and power density for Ni/CeO_2/YSZ anode-supported thin-electrolyte MEAs (a) operating on 0% conversion syngas for a range of T_{cell} and (b) operating at T_{cell} = 800 °C for a range of syngas conversions.

LSV curves for the Ni/CeO_2/YSZ cells with thin electrolytes running at different temperatures on 0% conversion syngas feeds are shown in Figure 3.8(a). The results indicate a significant decrease in activation overpotentials (η_{act}) and iR_{bulk} losses with the increase in T_{cell}, such that at 800 °C, maximum power densities reach 0.6 W/cm2. At a reasonable operating voltage of 0.75 V/cell that avoids Ni oxidation, power densities at 800 °C are as high as 0.32 W/cm^2. As T_{cell} is reduced to 750 and 700 °C, power densities at 0.75 V drop to 0.19 and 0.12 W/cm^2 respectively. These

results belie the trade-off between lowering T_{cell} down to 700 °C where sealing issues are greatly simplified and reducing power density by a factor of more than 2.5X for an SOFC plant with external reforming. This trend was to be expected given that all three overpotentials increase with decreasing temperature. R_{bulk} increase because YSZ O^{2-} ion conductivity drops strongly with temperature, activation overpotentials increase because the electrochemical reaction rates slow down, and concentration overpotentials increase because gases diffuse more slowly and cannot penetrate the porous electrodes as quickly. Interestingly, the MEA performance on syngas was very similar to the performance on humidified H_2 at similar P_{H2}/P_{H2O} suggesting that CO did not negatively impact electrochemical oxidation rates at the low overall fuel utilization in these button cell experiments. This similarity between the different fuels is likely caused by the excess H_2 in the flow dominating the electrochemical reactions. Also at these temperatures CO and H_2O were likely shifted into H_2 and CO_2 (Reaction 1.5) and as a result CO probably did not significantly impact the electrochemical reactions.

Increases in R_{bulk} and η_{act} for the cathode likely drive the reduction in power density with decreasing temperature since it is known that both bulk O^{2-} diffusion and O_2 reduction on LSM cathodes have relatively high effective activation barriers ~80 kJ/mol for bulk diffusion [48] and 120 to160 kJ/mol for O_2 reduction [46]. However, to explore anode variations, syngas composition was varied by exploring different amounts of conversion of H_2 + CO for the button cell anode feeds to simulate different locations in a typical SOFC channel flow. Figure 3.8(b) shows that at 800°C, anode performance does decline due to loss in P_{H2} and P_{CO} (as indicated in

Table 3.1) due to increased syngas conversion. The difference in performance seems to be in part due to a thermodynamic shift in the open circuit voltage (OCV). Otherwise, the slopes for the different syngas compositions are similar indicating little change in the anode polarization resistance, $R_{pol,anode}$ with the change in anode feed concentrations. At 0.75 V, there is not significant drop in power density from 0% conversion to 25% conversion – 0.34 W/cm^2 to 0.30 W/cm^2. At 50% syngas conversion the power density drops only to 0.20 W/cm^2. This relatively slow drop in power density with increased fuel conversion suggests the value of running SOFCs with reformate because of the relatively shallow decline in power density with increasing fuel conversion across the length of an anode flow path.

EIS measurements for syngas as shown in Figure 3.9 indicated that R_{bulk} was almost identical for different syngas compositions. Cell experienced only minor drops in performance when operating under reduced fuel and increased product conditions, implying relatively even performance down the channel for a planar SOFC up to 50% syngas conversion. Ohmic resistances increase at lower temperatures because of drop in ionic conductivity of O^{2-} with temperature. Bode plot in Figure 3.9(b) shows more clearly that R_{bulk} was almost identical for different syngas compositions.

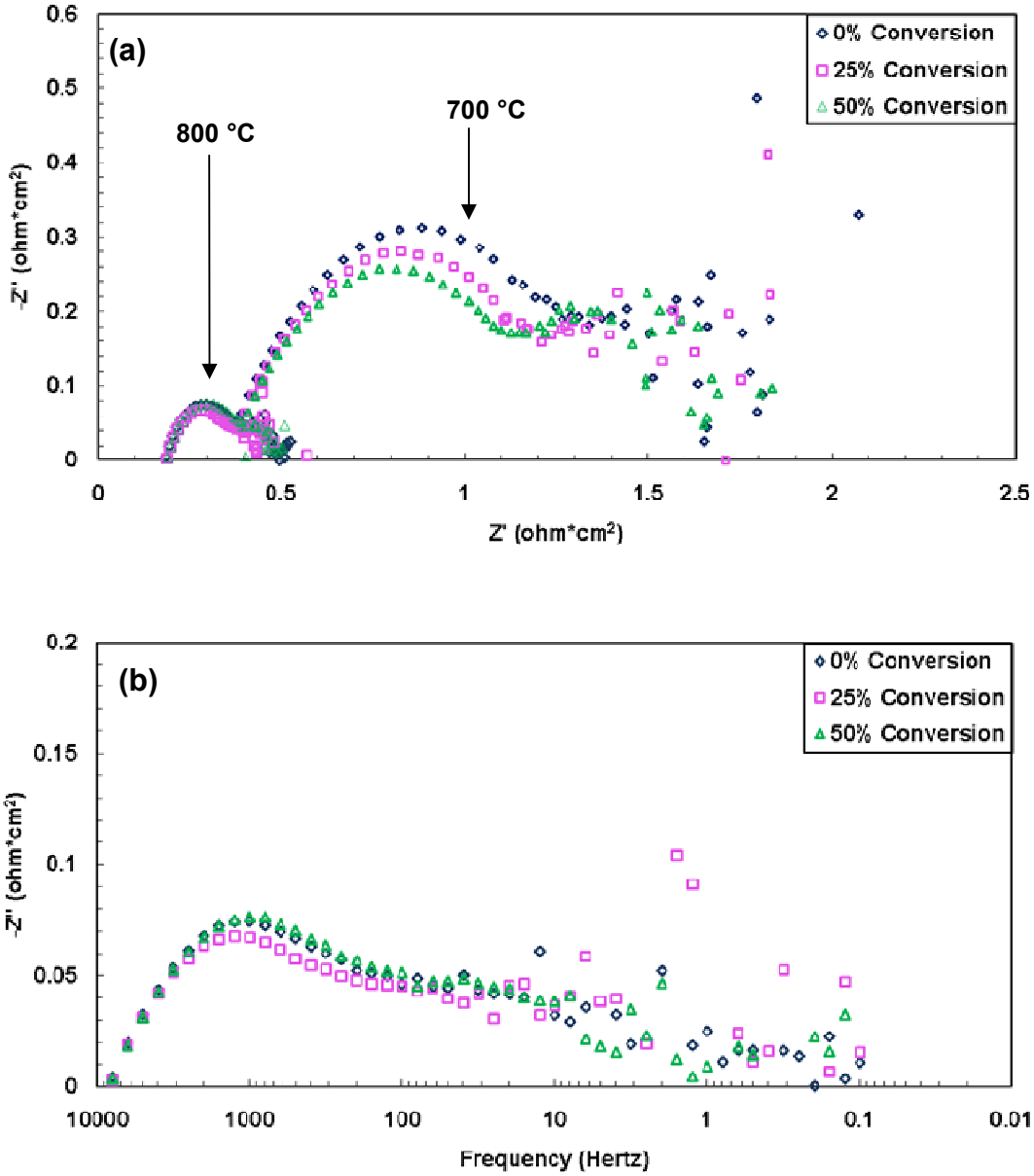

Figure 3.9: Impedance data for $Ni/CeO_2/YSZ$ cell operating on various syngas compositions (0%, 25% and 50% conversions) (a) at two different operating temperatures and (b) for a range of frequencies at 800 °C. Both parts (a) and (b) show impedance data for 100mV overpotential.

3.3.3 Testing with Carbonaceous Fuels – n-butane

Further testing on the co-fired Ni/CeO_2/YSZ-anodes was performed with *n*-C_4H_{10} feeds mixed with H_2O at two different *S/C* ratios of 1.5 and 1.0. As stated earlier, these flows were diluted in Ar by 50% in order to facilitate humidification. The *S/C* ratios are lower than a typical steam reformer value (usually more than 2.0 for higher hydrocarbons) because the production of steam in the SOFC allows for a carbon-resistant catalyst (like CeO_2) to be effective at suppressing surface carbon formation, even at lower *S/C* feed ratios. Some studies on Cu/CeO_2 anodes have even suggested adequate suppression of surface carbon formation even under dry hydrocarbon fuel feeds [20]. The steam created from H_2 electrochemical oxidation can suppress surface carbon build-up in the Ni/ CeO_2/YSZ cells, even though the inlet C-H-O ratio is initially in the region where such graphitic carbon is expected based on equilibrium calculations [49].

Performance at T_{cell} = 700 and 800 °C is shown in Figure 3.10 for the Ni/CeO_2/YSZ MEA with the 10 μm thick electrolyte operating on n-C_4H_{10} anode feeds at S/C ratio of 1.5. At 800 °C, power density reaches 0.20 W/cm^2 at an operating voltage of 0.75 V and peaks at 0.33 W/cm^2. Performance at 800 °C and S/C of 1.0 was found to be comparable in power density to the *S/C* = 1.5 condition. Lowering T_{cell} to 700 °C reduced the power density at 0.75 V to 0.08 W/cm^2 for both *S/C*. In comparison to the syngas operation, direct n-butane feeds with internal reforming in the anode lower the power density by over 30-40%. This may in part be due to temperature reductions in the internal pores caused by the endothermic reforming. Also, at low *i*, the polarization resistance seems higher for butane than for

syngas (as seen from Figures 3.9 and 3.11), suggesting that the electrochemical oxidation step is slower for steam reformed butane. Barnett et al. [18] report similar findings when comparing steam reformed methane with hydrogen. The results indicate the critical need for the development and coupling of microkinetic reforming models (as have been developed for CH_4 anode feeds [33, 36]) to understand heterogeneous reforming chemistry in the support layer impacts electrochemistry in the functional layers with hydrocarbon SOFC feeds.

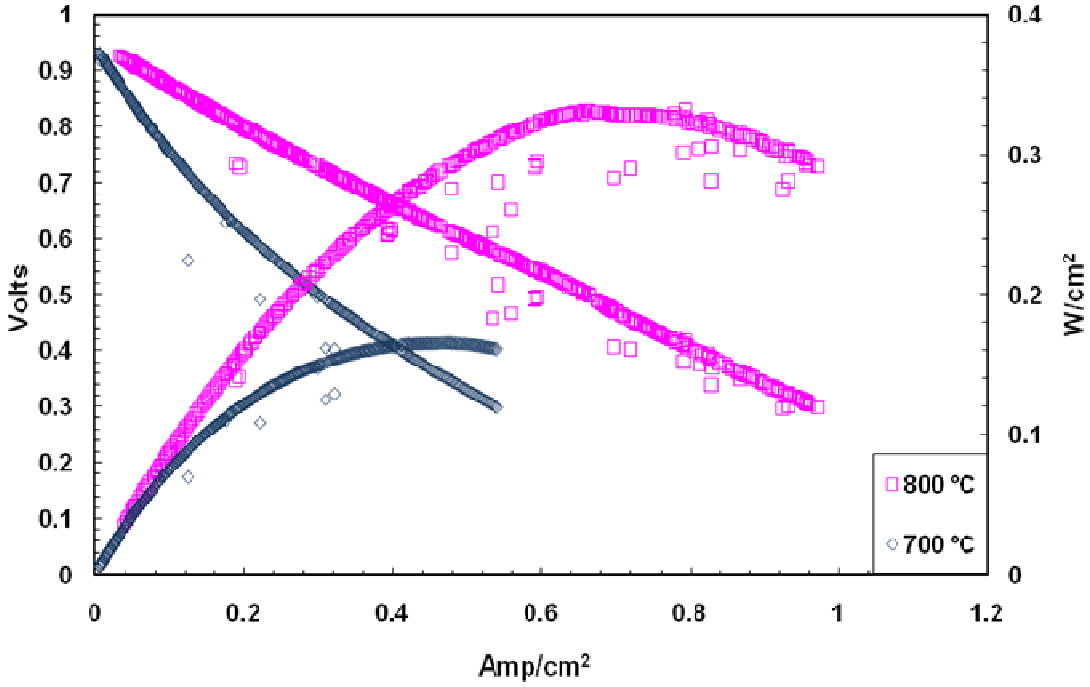

Figure 3.10: *V-i* curve and power density for Ni/CeO_2/YSZ anode-supported thin-electrolyte MEA operating at two T_{cell} on an n-butane feed with a steam-to-carbon ration of 1.5 to 1. 50% of total anode flow was composed of Ar.

The EIS data for n-C_4H_{10} is shown in the figure below. Interestingly, when comparing the impedance spectra of a Ni/CeO_2/YSZ MEA operating on n-C_4H_{10}/H_2O with the spectra of the same cell operating on syngas, the butane feed shows a broader low-frequency arc with a slower relaxation frequency (100 Hz). This means that even though R_{bulk} for syngas and *n*-C_4H_{10} are comparable, the higher $R_{pol,anode}$ for n-C_4H_{10} dominates the resistance. The high R_{pol} for the direct butane feeds indicates that surface chemistry and associated charge transfer processes all occur less effectively in case of n-C_4H_{10}. Barnett et al. [18] report similar results when comparing humidified hydrogen with direct internal reforming of methane. Their study suggests that the electrochemical oxidation step is slower for methane than for H_2 and CO.

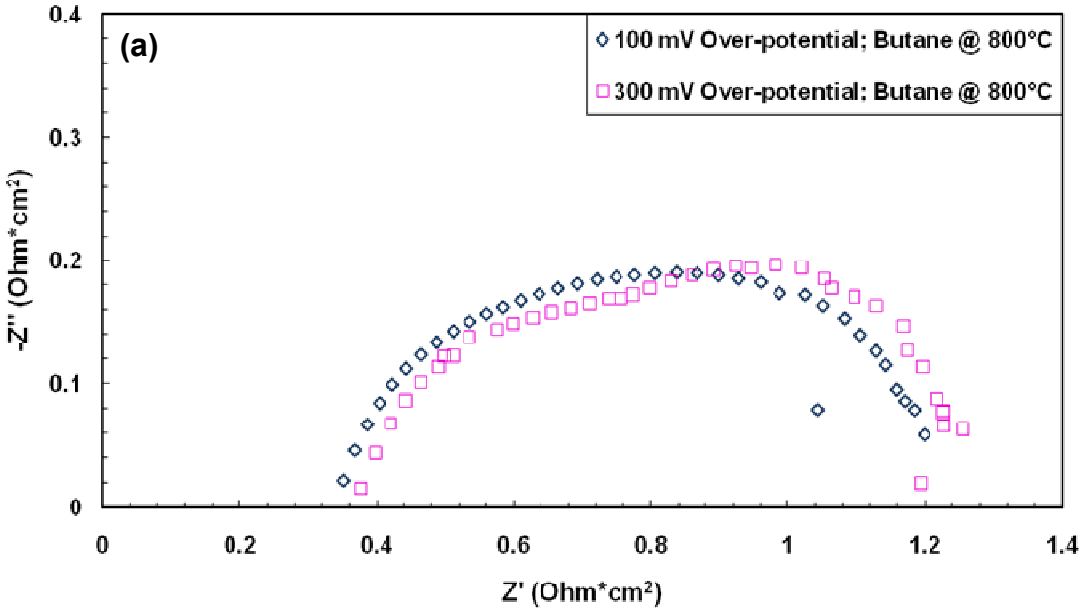

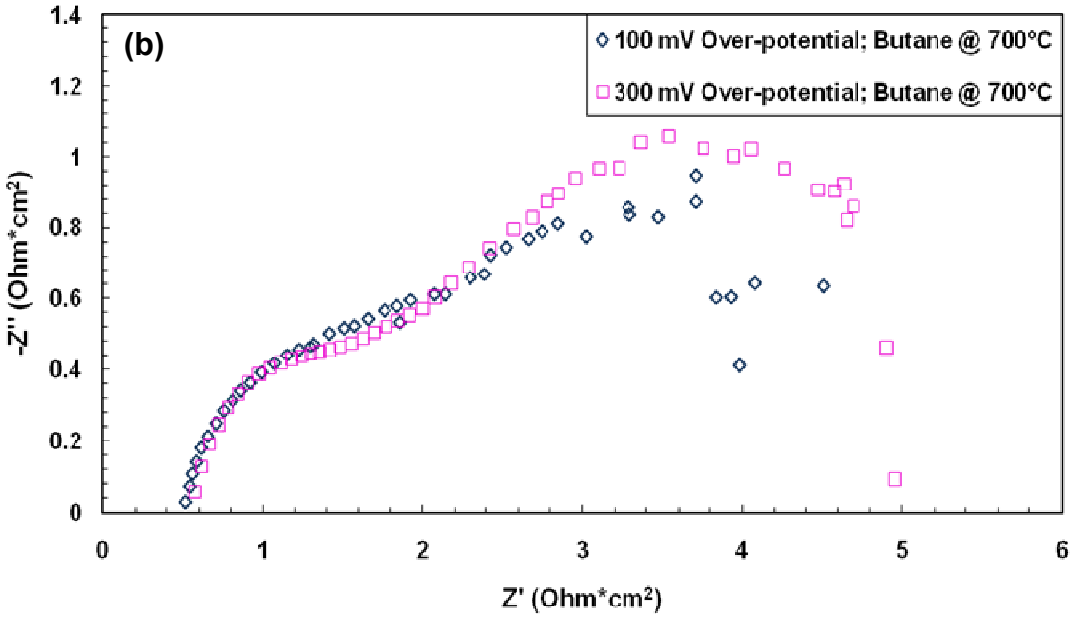

Figure 3.11: Impedance data for Ni/CeO_2/YSZ cell operating on steam reformed n-C_4H_{10} at (a) 800 °C and (b) 700 °C. For both cases, S/C ratio is 1.5 to 1. 50% of total anode flow was composed of Ar.

The EIS data at 700 °C clearly shows much higher polarization resistance compared to 800 °C. Also noteworthy is the much higher R_{bulk} at lower temperature. This is also corroborated by the much steeper LSV curve for lower temperature case. Impedance data at lower temperature has been consistently seen to be much noisier at lower frequencies as well. This might suggest that processes are much more stable at higher temperatures than at lower temperatures.

3.3.4 Stability testing with n-butane

After testing with n-butane for 800 °C and 700 °C for *S/C* ratios of 1.5 and 1.0, the cells were subjected to sustained exposure to butane for several hours. *S/C* ratio of 1.5 was chosen as the desired condition for stability testing, as 1.0 case tended to cause more coking. The flow conditions for *S/C* = 1.5 are given earlier in Table 3.1, require ~30 sccm of n-butane to the anode with the flow humidifier kept at ~78 °C to achieve the desired H_2O partial pressure. The corresponding Ar flow rate was kept at 200 sccm. On the cathode side, the air flow rate was maintained at ~700 sccm.

The humidifier temperature was found to fluctuate to ± 2 °C from the set point. In case of performance testing as discussed in section 3.1.2, the temperature was manually adjusted each time it was found to deviate from the set point to keep it within ± 1 °C of the desired temperature to achieve the required S/*C* ratio. But since the stability testing was done over several hours, it was not possibly to sit and manually adjust the temperature of the bubbler; hence an error of ± 7% in the output P_{H2O} was present in the stability tests. This translated into an average uncertainty of 12.4% in the actual *S/C*.

The stability testing was done by fixing the cell at an overpotential of 140 mV with respect to OCV and by plotting the output current was plotted with time. The current vs. time plot for stability of the $Ni/CeO_2/YSZ$ cell is shown in Figure 3.12. Each data point was recorded after duration of 10 seconds with respect to the previous one.

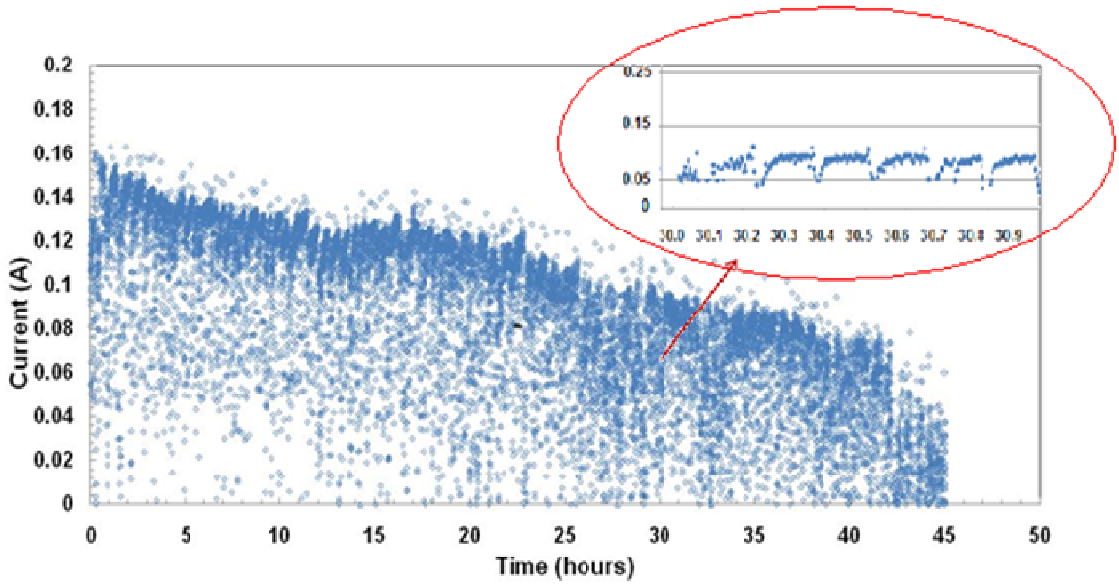

Figure 3.12: Stability test for Ni/CeO_2/YSZ cell operating on n-C_4H_{10} over 45 hours with S/C ratio of 1.5 (with 50% of total anode flow as Ar). Test conducted at a constant voltage of 0.7V. T_{cell} during stability test maintained at 800 °C.

It can be seen from the plot that the cell did deteriorate steadily in performance with time. The initial current obtained was ~0.15 A and it dropped to ~0.05 A over a span of 45 hours. The cell was still functional however, when the rig was disassembled and there were no cracks found on the cell. Thus, the cell withstood the impact of steam reforming of butane over several hours without losing its structural integrity. However, a regular fluctuating current was observed during the stability testing. This can in part be explained due to the fact that the water vapor out of the humidifier condensed inside the lines en route to the anode feed tube. This might have led to the steam being injected in bursts, leading to fluctuation in current output. However, as will be shown in a later section, same procedure was applied to

test the stability for Ni/YSZ cells, and hence the consistency in procedures provides somewhat of a basis for comparing stability for the two different types of cells.

3.4 Comparison of performance between Ni/CeO_2/YSZ and Ni/YSZ cells

Since a principal aim of this work was to establish the importance of ceria in improving the cell performance and durability of the SOFC anodes, it was important to compare the ceria based anodes to Ni/YSZ anodes. In this section, the two cells have been compared for both syngas and *n*-butane. After electrochemical characterization, the cells have been characterized with SEM, energy-dispersive X-ray spectroscopy (EDX), Raman spectroscopy and X-ray diffraction (XRD) to assess how the ceria impacts the microstructure, stability, and carbon deposits during electrochemical oxidation of carbonaceous fuels.

3.4.1 Performance with syngas

In the previous section, Ni/CeO_2/YSZ cells showed high power density with a sample cell having a thin electrolyte (10 μm thick). The sensitivity of these thin electrolytes to cracking during testing and thermal cycling encouraged many tests with more robust MEAs having 20 μm thick electrolytes. Primary reason for cracking seems to be the CTE mismatch between the cell and the mounting tube. Also, the alumina paste used for sealing the cell on to the tube may have contributed to cracking as it too has a CTE mismatch with the cell. The thicker electrolytes reduced power density due to the increase in R_{bulk} but ohmic losses associated with

$i \cdot R_{bulk}$ could be readily subtracted such that the overpotentials associated with the electrode activation and transport losses could be readily compared independent of the electrolyte thickness. The thicker electrolytes were used with both Ni/YSZ and Ni/CeO_2/YSZ cells in order to facilitate comparison of the two anodes for longer periods of operation without having cell cracks. Figure 3.13 shows the general trend that was observed with syngas feeds that the co-fired CeO_2-containing anodes outperform the Ni/YSZ anodes with maximum power densities about 20% higher for the CeO_2 cells. The primary difference for this increase in power density is a higher OCV for the ceria cells when compared to the Ni/YSZ cells. This could be due to more pinhole leaks in the electrolyte for the Ni/YSZ cells than for the Ni/CeO_2/YSZ cells. There is also a stronger reduction in total polarization resistance R_{pol} at higher current densities (> 0.5 A/cm^2) for the Ni/CeO_2/YSZ anode. The reason for this could be that ceria becomes active at high current densities. At around i >0.5 A/cm^2 activity for CO becomes more important because the local P_{H2} can be depleted. Ceria accelerates water-gas-shift and CO electrochemical oxidation and this effect manifests at the high overpotentials when P_{H2} locally in the pores becomes more depleted. This could explain the improvement in the slope of the V-i curve thereby improving the performance of the cell.

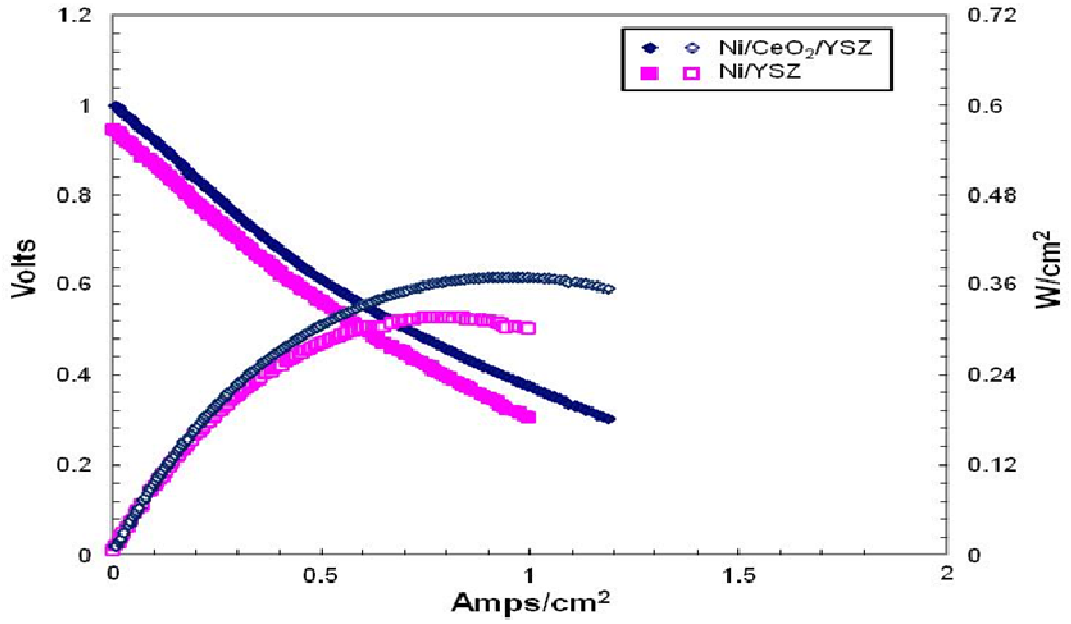

Figure 3.13: Comparison of *V-i* and power density curves for Ni/CeO_2/YSZ and Ni/YSZ anode-supported MEAs with 20 μm thick electrolytes – operating on 0% conversion syngas at T_{cell} = 800 °C.

While R_{pol} at high current densities for the two different anodes differed, at low current densities R_{pol} for the two types of anodes were very similar as shown in the impedance spectra of Figure 3.14 for both a Ni/YSZ cell and Ni/CeO_2/YSZ cell with 20 μm electrolytes at a constant η_{tot} = 100 mV (corresponding i = 0.1 A/cm^2). For syngas at 0% conversion, the impedance spectra for the two cells show two dominant processes with characteristic frequencies of 316 and 10 Hz respectively. Both characteristic frequencies increase with increasing η_{tot}, and as illustrated in the *V-i* curve of Figure 3.14, total R_{pol} decreases with increasing η_{tot} (i.e., i). Further, the CeO_2 cells have slightly stronger decrease in R_{pol} with η_{tot}.

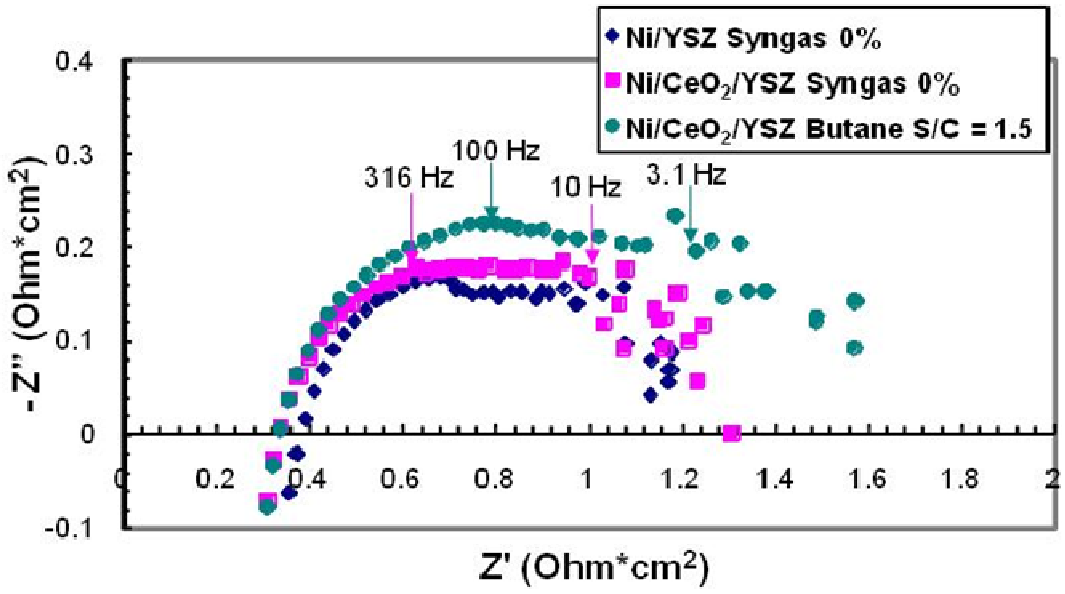

Figure 3.14: Electrochemical impedance spectra at 100 mV total cell overpotential for Ni/YSZ cell with syngas feed at 0% conversion and with Ni/CeO_2/YSZ cell operating on syngas at 0% conversion and n-butane with *S*/C = 1.5. Electrolytes for both cells were approximately 20 µm thick. T_{cell} = 800 °C for all cases.

3.4.2 Performance with direct n-butane feeds

Cu/CeO_2/YSZ cells have been shown to be effective at suppressing surface carbon formation in SOFC anodes operating on a range of hydrocarbon feeds [12, 25]. However, this study sought to assess whether the addition of CeO_2 to Ni/YSZ could suppress carbon deposits associated with direct carbon feeds to the more active Ni electrocatalysts. Figure 3.15 shows LSV curves for MEAs with a Ni/CeO_2/YSZ anode and a Ni/YSZ anode operating with *n*-C_4H_{10}/H_2O feeds at *S/C* of 1.0 and 1.5 respectively. Both cells had 20 µm thick electrolytes. These curves were taken early on during the testing of each cell with n-butane feeds because the Ni/YSZ cell

performance degraded over a period of ~20 hours of testing (Figure 3.17). Such rapid degradation was not observed in Ni/CeO_2/YSZ cells. In general, the CeO_2 addition results not only in improved stability as well as initial performance. The improved performance is most significant at current densities > 0.3 A/cm^2 where a significant reduction in the R_{pol} (as indicated by the reduction in slope of the *V-i* curves in Figures 3.15 for the Ni/CeO_2/YSZ cell. The cause for this change in R_{pol} is uncertain but may likely be due to the enhanced water-gas-shift reaction rates caused by inclusion of ceria in the anode support layer [66]. Water gas shift becomes important particularly at higher current densities where higher fuel utilization can cause local P_{H2} to deplete inside the anode functional layer. At this point, ceria/nickel composite's role as a water-gas-shift promoter assumes importance because it can increase P_{H2}. Sukeshini et al. [69] have shown that CO electrochemical oxidation is 2 to 3 times slower than H_2 and that a mixture of H_2 & CO with 25% or higher H_2 behaves similar to pure H_2 in performance, further suggesting that water-gas-shift makes significant contribution to the cell performance with H_2/CO mixtures.

The cell performance in terms of initial *V-i* curves before degradation show little dependence on *S/C* for the range of *S/C* studied (1.0 to 1.5). *S/C* ratio of 1.0 however, did accelerate cell degradation due to enhanced carbon deposition due to the reduced amount of H and O available with the lower *S/C*.

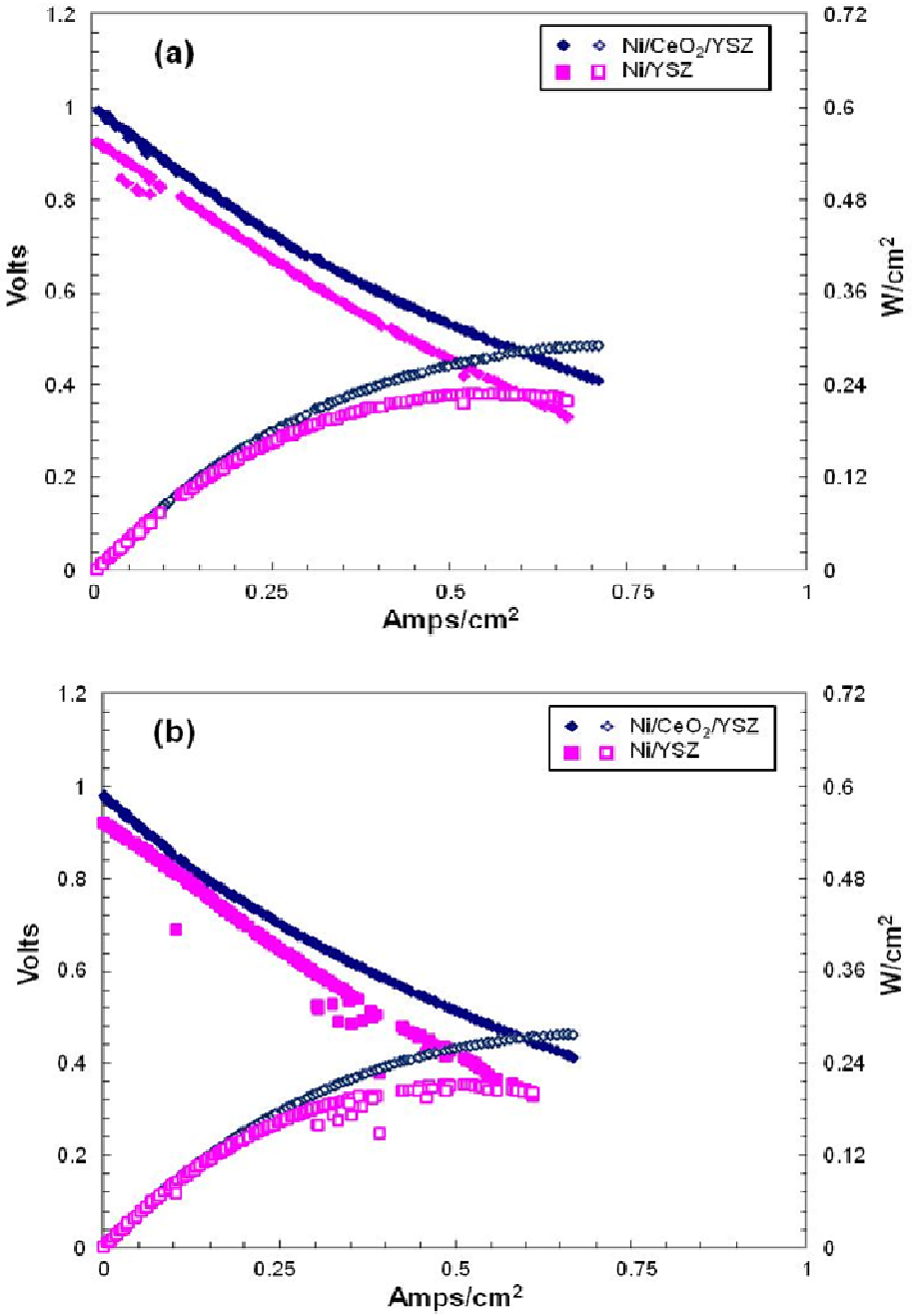

Figure 3.15: Comparison of voltage and power density vs. current density curves for $Ni/CeO_2/YSZ$ and Ni/YSZ anode-supported MEAs with electrolyte thicknesses of ~ 20 µm for n-butane feeds with (a) T_{cell} = 800 °C and S/C = 1.0 and (b) T_{cell} = 800 °C and S/C = 1.5.

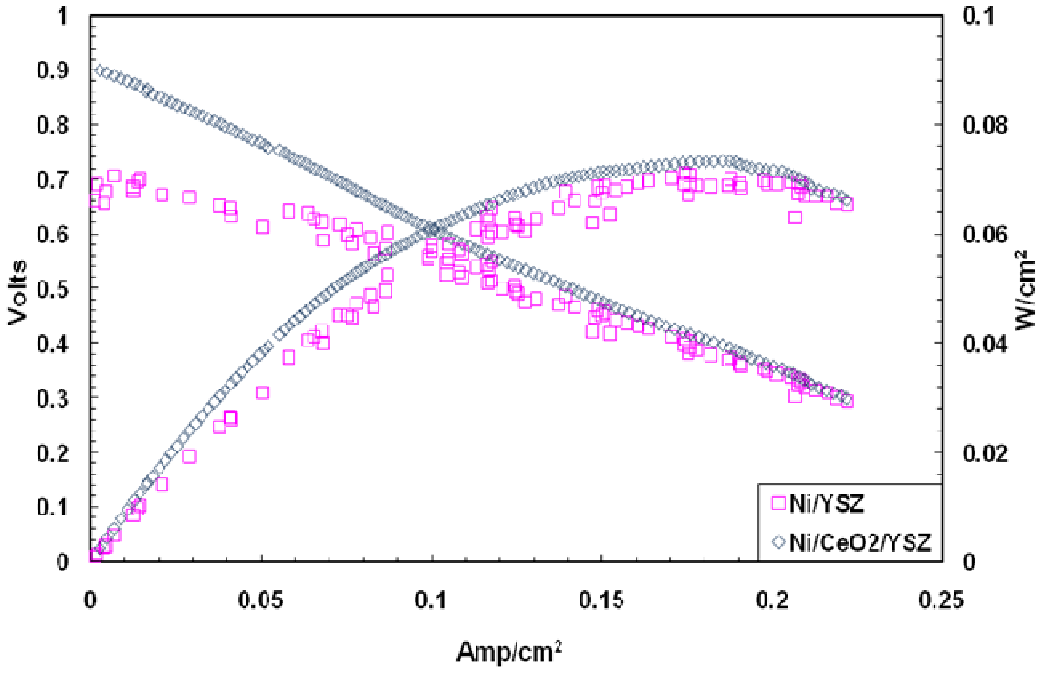

Figure 3.16: Comparison of voltage and power density vs. current density curves for $Ni/CeO_2/YSZ$ and Ni/YSZ anode-supported MEAs with electrolyte thicknesses of ~ 20 µm for n-butane feeds with T_{cell} = 700 °C ad S/C = 1.5.

Performance comparison at 700 °C showed no significant difference between the two types of cells, except that the $Ni/CeO_2/YSZ$ cells started off with much higher OCV (~ 0.9V) compared to the Ni/YSZ cells (OCV ~ 0.7V) Power densities of the two cells were comparable to each other, although Ni/YSZ seemed to peak at 0.071 W/cm^2 compared to $Ni/CeO_2/YSZ$ which had the highest power density of 0.073 W/cm^2. Only notable difference seems to be the higher OCV for $Ni/CeO_2/YSZ$ cells. It could be explained through high leakage in the Ni/YSZ cells that reduces OCV.

Shown below are the i.R_{bulk} corrected curves for both Ni/YSZ and Ni/CeO_2/YSZ cells. Using the respective impedance data, η_{ohm} was subtracted from both the cells in order to compare them in terms of their polarization resistance. Notwithstanding OCV differences (which are assumed to be due to higher leakage through the Ni/YSZ electrolyte pinholes), the higher slope for Ni/YSZ cell indicates higher R_{pol} compared to Ni./CeO_2/YSZ. Tests were performed for steam reformed n-C_4H_{10} at *S/C* ratio of 1.5 to 1. T_{cell} was recorded as 800 °C.

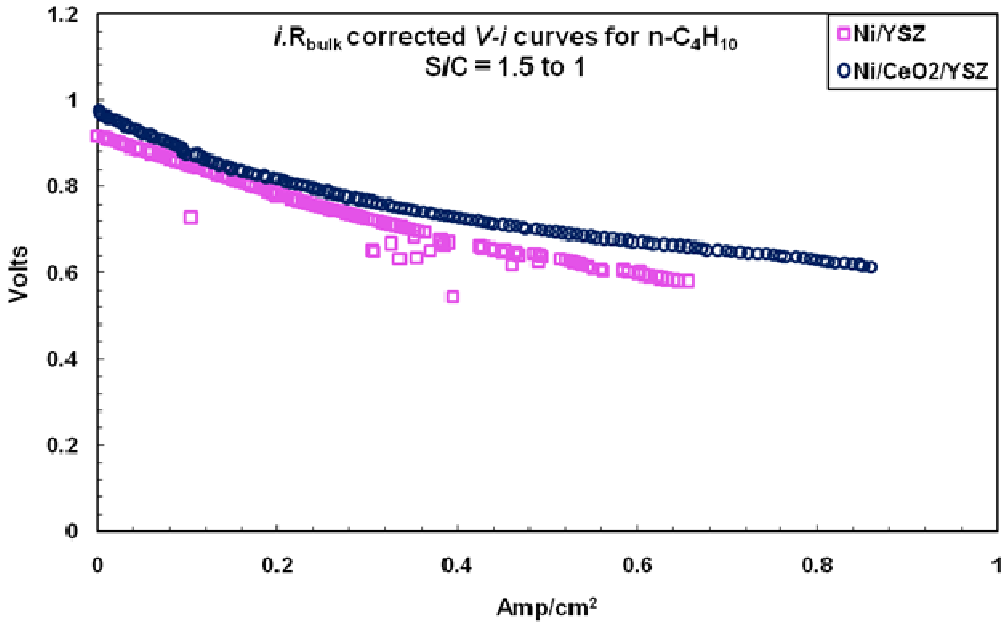

Figure 3.17: *V-i* curves for Ni/YSZ and Ni/CeO2/YSZ cells after subtracting *i*.R_{bulk} for n-C_4H_{10} feeds with *S/C* = = 1.5and T_{cell} = 800 °C.

Figure 3.18 shows the comparison of both types of cells in terms of their stability for continuous operation on steam reformed n-butane feed. Cells were kept at

total overpotential of 140 mV with respect to OCV in n-C_4H_{10} steam feeds at *S/C* = 1.5 and T_{cell} = 800 °C. OCV for Ni/YSZ was 0.71 V and that for Ni/CeO_2/YSZ was 0.84 V. Regular periodic oscillations observed could be attributed to condensation inside the lines out of the humidifier to the anode feed tube. This might have resulted in the steam being supplied in bursts, leading to fluctuations in current. The temperature of the humidifier also had a tendency to deviate from the programmed temperature. The controller fluctuated by ± 2 °C around the set point. This could have led the *S/C* ratio to deviate from the desired value of 1.5.

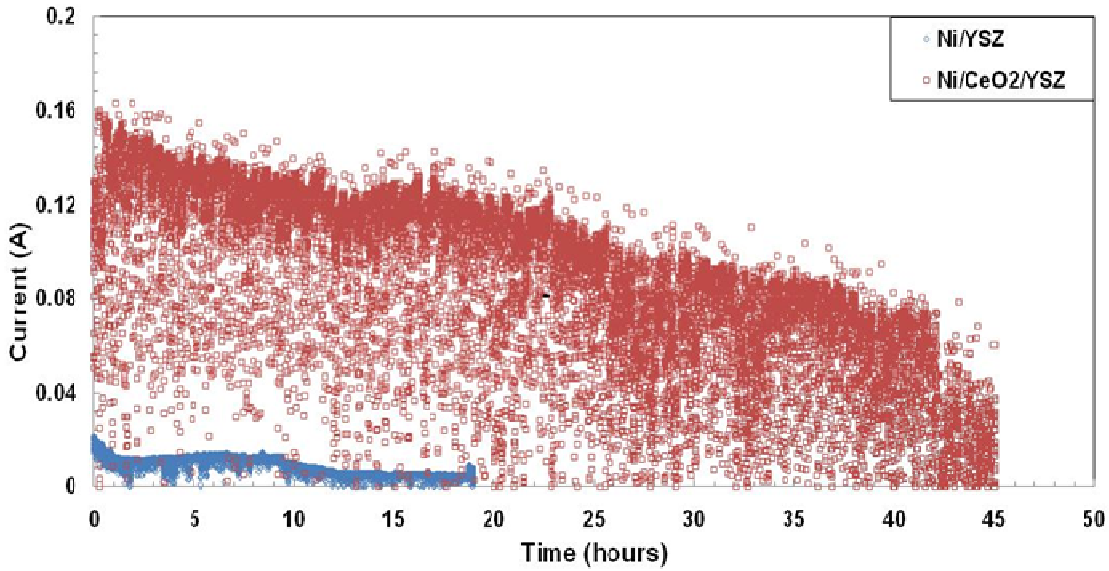

Figure 3.18: Long term stability testing for n-butane feed at S/C = 1.5. Cells kept at a constant total overpotential η_{tot} =140 mV.

As is evident from the Figure 3.17, the Ni/CeO_2/YSZ cell outlasts the Ni/YSZ cell not only in terms of the no. of hours of stable operation (Ni/CeO_2/YSZ cell

performs stably for 25 more hours than Ni/YSZ) , but also in terms of the power density that can be obtained using these cells. Both cells were kept at a constant voltage at 140 mV below their respective OCVs. Ni/CeO_2/YSZ cells provide ~ 20% higher (for syngas) and 25% higher (for steam reformed n-C_4H_{10}) performance in terms of the power density (although degrading slowly with time) compared to their un-doped counterparts.

3.4.3 Material Characterization of the Ni/CeO_2/YSZ cells post testing

Post testing, the Ni/YSZ cell was found to have a crack large enough to split the cell into fragments. It is believed that long term exposure to butane and the subsequent carbon formation in the GDL pores was found to have structurally degraded the anode support layer. At this point, the experiment was terminated and the cells were cooled down from 800 °C to room temperature in Ar environment (100 sccm Ar with 5% H_2 on the anode side) and low air flow on the cathode side (75 sccm) at a cooling rate of 1 °C/min. to minimize further cell damage. The ceria doped cells also developed cracks during some of the tests, but on fewer occasions. In one case, the ceria doped cell lasted for 5 days even after exposure to butane for over 45 hours. Both the Ni/YSZ and Ni/CeO_2/YSZ cells were then analyzed with ultra-high resolution scanning electron microscope, Hitachi SU-70 at the Nanocenter at the University of Maryland. The images in Figure 3.19 show the anode support layer microstructures of the cells at high resolution. In Figure 3.19, the ceria-containing anode supports do not show the large pores that developed at the top surface of the Ni/YSZ cathode support. It is believed that these large pores were formed due to the

carbon particles growing inside the anode support layer microstructure [65]. A macroscopic image in Figure 3.20 was also taken with a digital camera that shows the disintegration of the anode surface of Ni/YSZ cell more clearly.

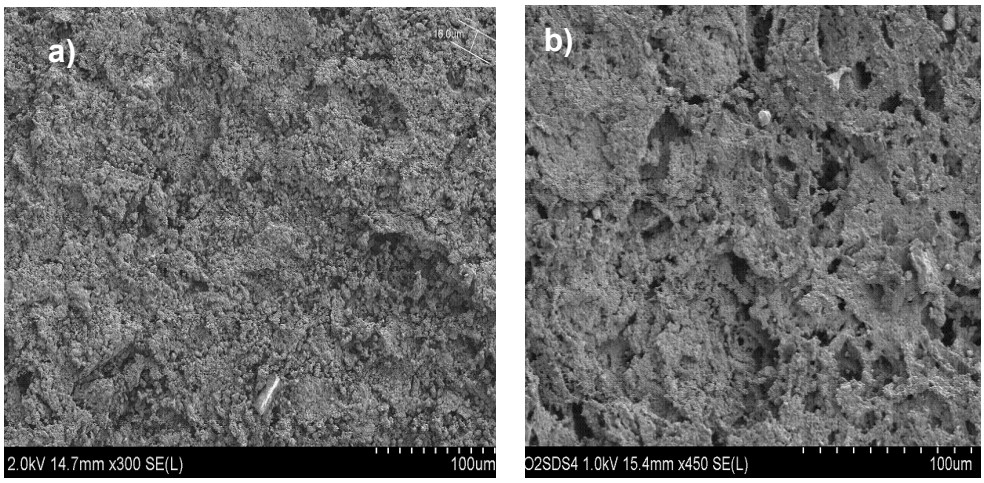

Figure 3.19: SEM image of a) Ni/CeO_2/YSZ and b) Ni/YSZ anode support layer microstructure after exposing the two cells for over 45 hours under steam reformed butane at *S/C* = 1.5.

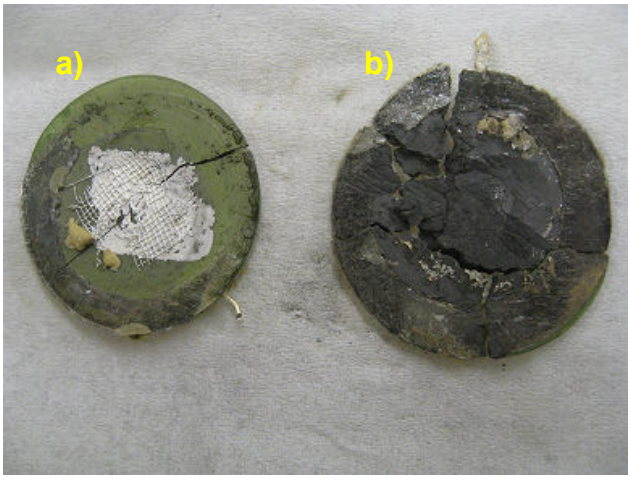

Figure 3.20 Photographic images of a) Ni/CeO_2/YSZ and b) Ni/YSZ anode support layer after exposing the cells for over 45 hours (Ni/CeO_2/YSZ) and over 20 hours (NiYSZ) under steam reformed butane at *S/C* = 1.5.

The anode support layer images taken from a digital camera in Figure 3.20 show the results of long term exposure and the resulting loss of structural integrity of the anode support layer, especially in the case of Ni/YSZ. Such disintegration is not observed in case of the Ni/CeO_2/YSZ cell, probably due to the formation of meta-stable cerium zirconates, as discussed in the following sections. Ni/CeO2/YSZ cell also developed a crack (although it lasted for 5 days before the experiment was terminated) possibly due to CTE mismatch between the cell-tube-sealant assembly. Also seen on the periphery of the cells are the remnants of the mica seal.

Energy-dispersive X-ray spectroscopy (using Bruker's silicon drift detector) was used to perform an elemental line scan to find the presence of carbon formation near the surface of the anode support layer. The scan was performed starting from the anode free surface up to a depth of about 300 microns in case of both Ni/YSZ and Ni/CeO_2/YSZ. The line scan is only a qualitative indication of the presence of graphite as it gives the relative intensity of the substance in percentage, but it provides further evidence of the location of carbon deposition in the anode support layer. The scans, however, do not reveal much information in terms of the amount of carbon deposition that can be used for comparing the cells. Hence, EDX was not pursued further. In the case of Ni/CeO_2/YSZ cell, small amount of carbon does form

near the anode surface. As will be shown by Raman studies, carbon deposition is suppressed further into the depth of the anode support layer. In case of Ni/YSZ cell, there is a steady growth of carbon through the depth of the anode support layer.

In order to compare the amount of graphite inside Ni/YSZ and Ni/CeO_2/YSZ anode support layers after several days of testing, depth profiling was pursued by measuring the Raman signatures of graphite, NiO and YSZ at four different locations of the anode using the Renishaw In-Via Raman microscope. This technique [10] has been shown to be effective in characterizing graphite formation on Ni/YSZ cermet anodes in solid oxide fuel cells for different hydrocarbons, and is a fairly quick means of detecting the presence of graphite and other substances inside the GDL. Samples were irradiated with the 488 nm output of an Ar+ ion laser (25 mW) focused to a narrow spot on the desired locations in the cross section of the anode. The laser beam bouncing off of the sample was recorded over a span of 10 minutes and then filtered for improved signal-to-noise ratio to eliminate the constant background of solar radiation.

Figure 3.21 shows the Raman spectra form the depth profiling. The spectra indicate two features associated with the formation of graphitic carbon. The vibrational band at a wave number of 1500 cm^{-1} arises due to the presence of highly ordered graphite and is generally labeled “G”. The band at 1360 cm^{-1} is much broader and corresponds to tetrahedral carbon defects within a graphite lattice and is labeled as “D”. Also featuring prominently are the signatures of NiO at ~1100 cm^{-1} and that of YSZ at ~590 cm^{-1} [10].

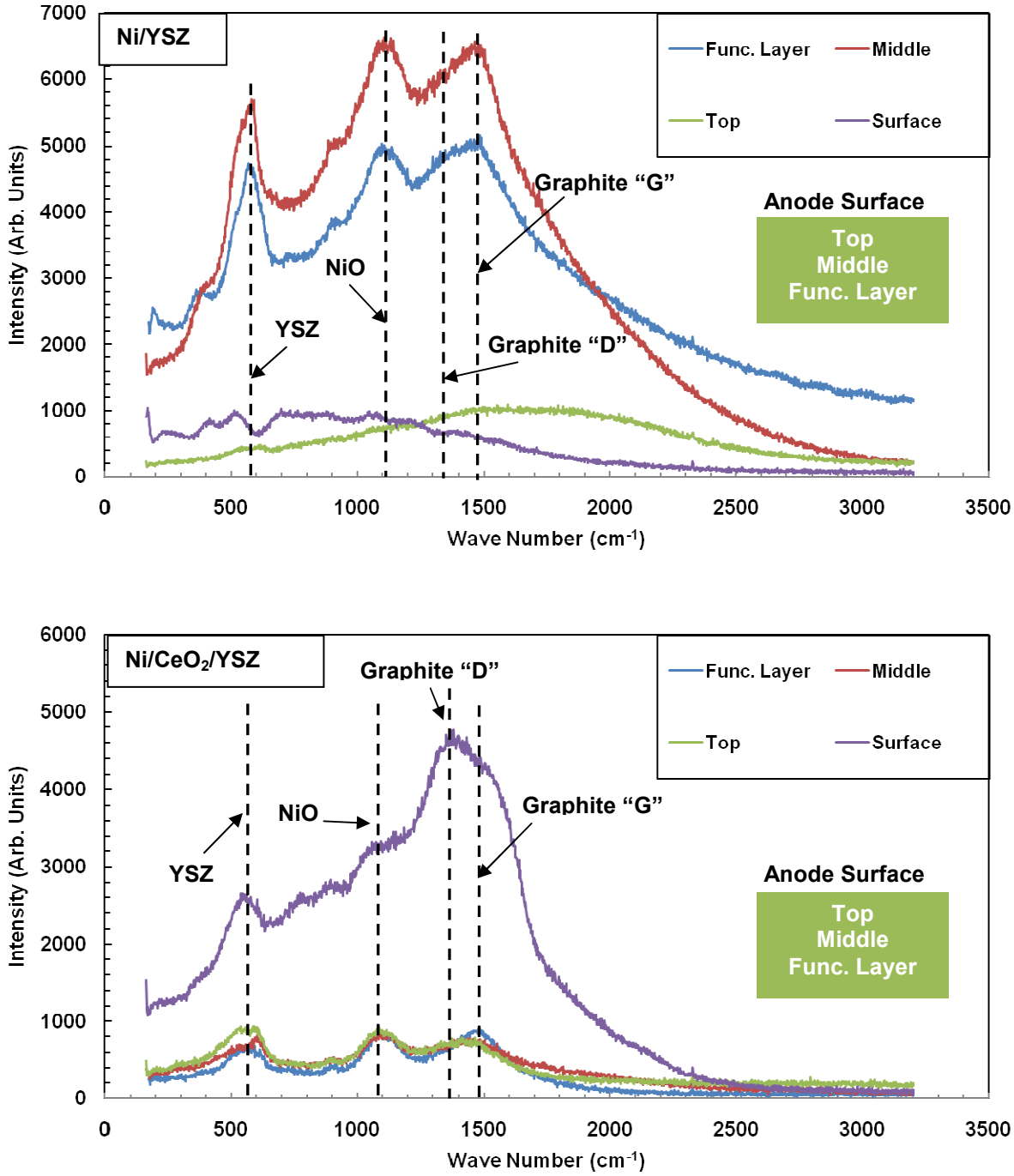

Figure 3.21: *Ex-situ* Raman spectroscopy on Ni/YSZ & Ni/CeO_2/YSZ anodes at three different locations starting from the anode free surface through the depth of the GDL. Peak intensities are absolute.

Although Figure 3.21 reveals the presence of carbon inside both Ni/YSZ and Ni/CeO2/YSZ cells, the absolute intensities of the peaks do not reveal much in terms of whether the carbon deposition grows inside the GDL or is minimized inside the GDL. The variation in reflectance of the different cells can lead to changes in signal strength and can provide misleading conclusions with regard to the amount of carbon deposition. For this purpose, strength of the graphite peaks relative to YSZ peak (at wave-number 588.3 cm^{-1}) would provide a better indication of how the graphite amounts compare for different cells. The measurements were done using the same lens (10X magnification) and the same laser wavelength (488 nm) for both Ni/YSZ and Ni/CeO_2/YSZ. An interesting feature about Figure 3.22 is the growth of graphite inside the depth of the GDL in case Ni/YSZ. Relative intensity of graphite "D" is lesser (0.8) on the surface but grows significantly through the depth and increases to more than 2.0 at the 'top' layer and then comes down to about 1 at the functional layer. This trend is reversed in case of the Ni/CeO_2/YSZ cells where relative intensity of graphite "D" is more on the surface (about 1.7) but is suppressed as one goes down to the 'top' layer (0.8) & functional layer (where it reduces to 1.0).

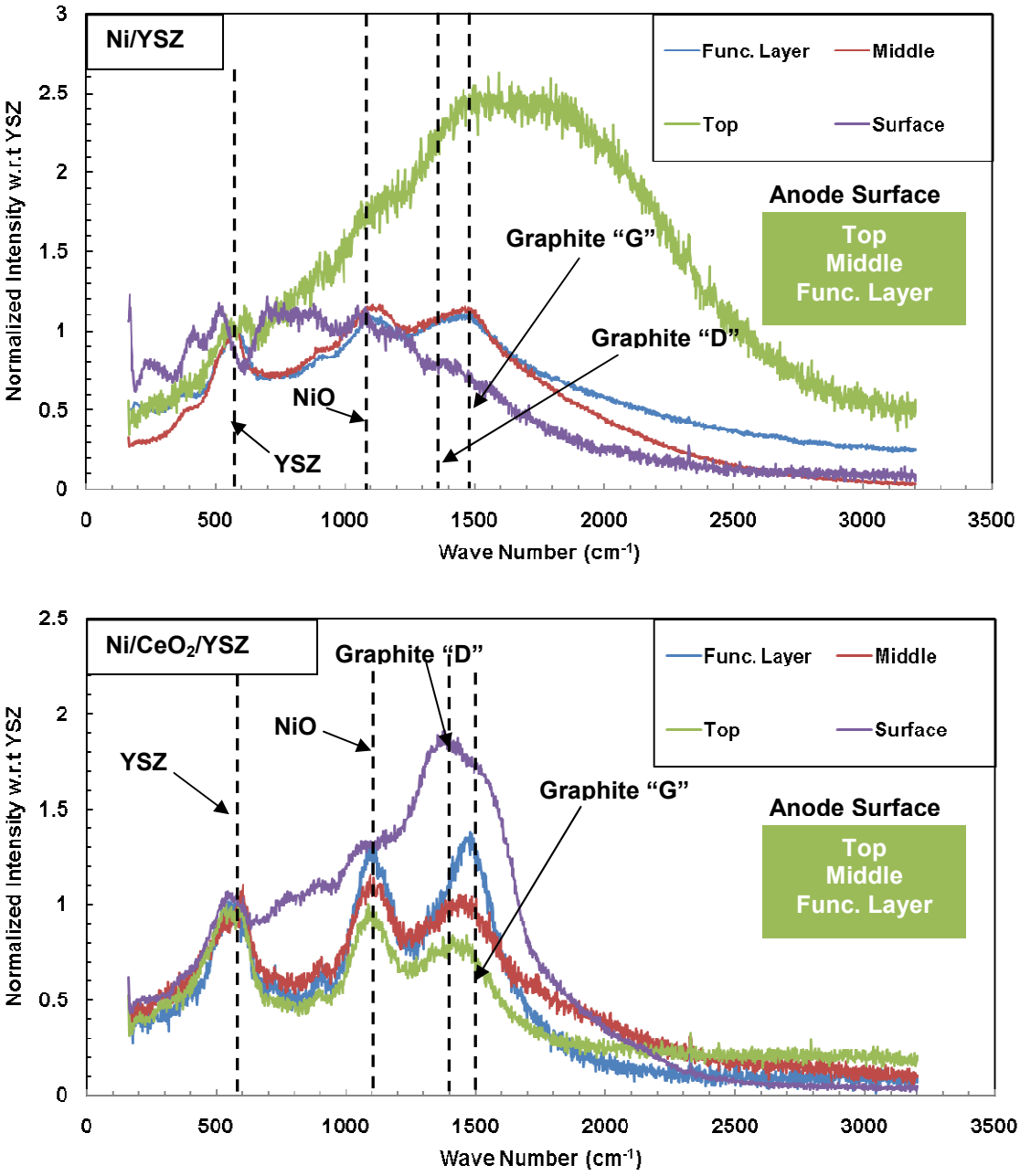

Figure 3.22: *Ex-situ* Raman spectroscopy on Ni/YSZ & Ni/CeO_2/YSZ anodes at three different locations starting from the anode free surface through the depth of the GDL. Peak intensities are relative to YSZ at 588.3 cm^{-1}.

The above experiments provide evidence for the suppression of graphite inside the anode support layer doped with ceria. However, when it comes to the mechanical strength of the anode to withstand the long term exposure to carbonaceous fuels, more characterization is needed. X-Ray Diffraction studies were done in order to study the reason for enhanced durability of the ceria doped anode support. It has been reported by Menzler et al. [66] that due to re-oxidation of nickel on account of leakage through electrolyte pinholes, serious risks are involved in terms of mechanical integrity of the anode support. Conventional Ni/YSZ based anodes disintegrate due to volumetric expansion occurring due to nickel re-oxidation inside the GDL. Presence of cerium zirconates in SOFC anodes can provide mechanical stability to the porous matrix and allow the cells to function even on exposure to carbon deposition. Cerium zirconates are known to be stable in redox cycles at temperatures in excess of 800 K [44, 45]. For fabrication of solid oxide fuel cell anodes, doped ZrO_2 are extensively employed to prevent undesirable mechanical or chemical transformation of the material under workable conditions. It has been reported [44] that the martensitic tetragonal-to-monoclinic transformation is responsible for the high fracture toughness of zirconia ceramics.

As reported by Trovarelli [44] in the chapter on structural properties and thermal stability of ceria-zirconia and related materials (Chapter 6, Figure 6.2), at temperatures below 1000 °C the phase diagram shows a monophase region of monoclinic (m) symmetry for CeO_2 molar contents less than ~ 10 %. The variation of the structural properties of the ceramic type of the CeO_2-ZrO_2 mixed oxides has been

investigated in detail by various researchers. The structural properties of the mixed oxides can be related to the parent simple oxides.

In case of doped CeO_2-ZrO_2 systems, the main reason for doping is to prevent the undesirable phase separation which can occur upon high temperature ageing. For cerium zirconates with ~ 10 mol % of yttria, phase transition from 't' to a cubic phase has been detected. In another investigation of ceramic type of materials of the $0.9(Zr_{1-x}Ce_xO_2)$ - $0.1(Y_2O_3)$, cubic flourite type solid solutions have been detected over the whole range of CeO_2-ZrO_2 compositions. It has also been reported that in addition to the stabilization of the cubic phase, use of dopants may favor both phase purity and surface area.

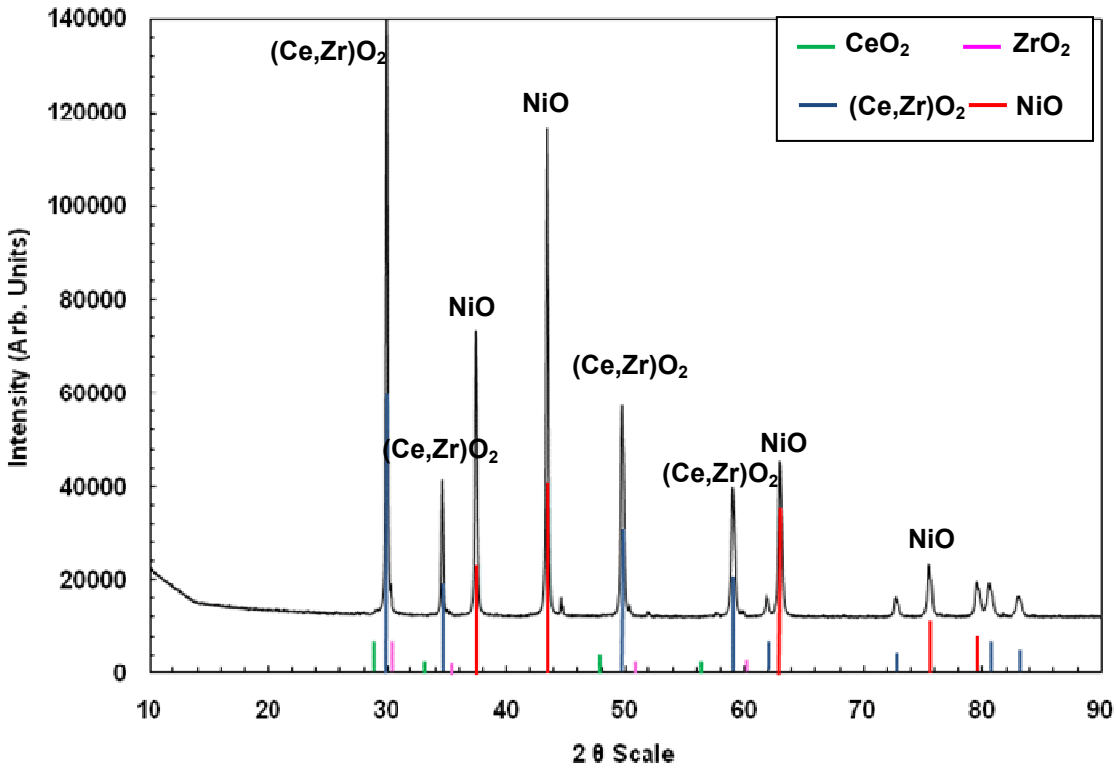

Figure 3.23: Rietveld plot of the X-Ray Diffraction pattern obtained at 25 °C from the powder of anode support layer for Ni/CeO_2/YSZ cell after sintering it at 1450 °C. In addition to NiO, cerium zirconate peaks indicate solid phase reaction between CeO_2 and ZrO_2.

Figure 3.23 shows the presence of cerium zirconates through XRD pattern. Note that the intensity peaks correspond to values on 2-θ scale that lie in between the values for pure CeO_2 and pure ZrO_2. NiO peaks are also shown above. All these oxides (NiO, CeO_2, ZrO_2 and cerium zirconate) exist as cubic lattices. The lattice dimension for pure CeO_2 is 5.4124 Å and that for pure ZrO_2 is 5.1280 Å. Based on the intensity peaks that lie in between CeO_2 and ZrO_2, one can interpolate to get the lattice dimension corresponding to the peaks. It comes out to be 5.1926 Å, which indicates that crystalline material different from both CeO_2 and ZrO_2 is formed. This proves the evidence of cerium zirconates in the ceria doped cells, explaining their mechanical durability.

3.5 Summary and Discussion

In this chapter, Ni/YSZ and Ni/CeO_2/YSZ cells were compared in terms of their *V-i* curves and power densities. Ni/CeO_2/YSZ outperform Ni/YSZ cells by ~20 % higher power densities for syngas and ~25% higher power densities for steam reformed n-C_4H_{10}. The improvement shown in this study for Ni/CeO_2/YSZ cell over Ni/YSZ, notwithstanding higher leakage seen in Ni/YSZ (the reason for lower OCV for Ni/YSZ compared to Ni/CeO_2/YSZ) could be attributed to increased water-gas-

shift reaction rates due to ceria addition. Also, ceria aids in CO electrochemical oxidation, providing alternate charge transfer pathways that can explain the reduced polarization resistance observed for cells with ceria in support layer.

The motivation behind adding ceria in the support layer, besides improving performance for syngas and steam reformed n-butane, was to reduce carbon deposition and improve long term operability with carbonaceous fuels. To this end, material characterization was done through Raman spectroscopy and XRD studies to first show the presence of graphite and further to compare carbon deposition in both the cells. Trovarelli [44] reports that ceria and zirconia undergo a solid phase reaction when sintered at around 1400 – 1500 °C to form cerium zirconates that are highly stable in redox cycles at higher temperatures. XRD studies did in fact reveal the presence of such compounds and the mechanical strength of Ni/CeO_2/YSZ anode support layer is attributed to them. Depth profiling through Raman spectroscopy showed that carbon deposition grows from the anode surface toward the anode functional layer through the cell depth in case of Ni/YSZ. Similar analysis in case of Ni/CeO_2/YSZ shows a reverse trend, lending credence to the belief that ceria aids in suppressing carbon formation inside the anode GDL.

The fact that ceria addition to Ni-YSZ cermet improves performance by enhancing the water-gas-shift reaction rates can in part also explain how ceria minimizes carbon formation inside the GDL. Any carbon formed near the electrochemically active region can be converted to H_2 and CO_2 by the presence of ceria. Hence, it is of certain advantage to add ceria in the anode support to achieve not only better performance compared to Ni/YSZ but also to gain long term operability.

Chapter 4: 1-D SOFC Modeling with Detailed Electrochemistry and Porous Media Gas Transport for Syngas

In order to develop SOFCs capable of high power densities on carbonaceous fuels as well as H_2, researchers have focused on developing materials that can operate for several 1000 hours for continuous operation with minimal degradation in performance of such cells. The U.S. Department of Energy's Solid-State Energy Conversion Alliance (SECA) has targeted a degradation of no more than 2% over 1000 hours [NETL, News Release – March 2009] Although there has been significant success in developing micro architectures and material sets that provide such durability, cost affordability (< $400/kW target for SECA [Williams 2007]) for materials and processing for large-scale commercial application remains a hindrance. Hence, researchers have to look at other ways of improving performance with the low cost materials such as nickel. One such approach to reducing costs is to optimize the 'micro-architecture' of SOFC electrodes in order to minimize gas transport resistance and to increase activity for beneficial heterogeneous reactions (reforming and water-gas-shift) and electrochemistry. Many groups have established the state of the art manufacturing approaches to produce SOFC electrodes with both functional layers and functionally graded support layers to enhance SOFC performance [39, 50-51]. However, it is still desirable to determine how electrode micro-structural parameters can be optimized to improve SOFC performance.

For such micro-architecture design, detailed modeling of the porous media can provide a methodology for rapidly assessing designs and material sets for improving SOFC performance at the micro-structure level. Previous modeling studies of SOFC porous electrodes and MEAs formulate the micro-architecture in terms of bulk geometrical parameters that characterize the porous-media structure [33, 36, 38, 54-55]. These parameters include porosity φ, tortuosity τ, specific catalyst and electrolyte areas per unit volume a_{cat} and a_{elec}, and electrochemically active three-phase-boundary per unit volume l_{TPB}. Although the parameters are often specified independently, DeCaluwe et al. [38] have shown that they are correlated for typical electrode architectures. The model considers porous-media gas transport using the dusty-gas model (DGM) which provides a basis for calculating transport fluxes as a function of porous media properties. Detailed microkinetic chemistry models provide a basis for relating reaction rates as a function of the specific areas and three-phase boundary lengths. Such models of this detail provide a basis for assessing how geometric parameters impact SOFC performance over a wide range of conditions.

Modeling efforts in the past have represented electrochemistry by single-step Butler–Volmer equations and Knudsen gas diffusion through the porous electrodes without reference to supporting surface chemistry on both the catalyst and electrolyte phases of the electrodes [56-57]. Models developed by Deutschmann et. al. [33, 55], DeCaluwe et. al. [38] and Kee et al. [33, 55, 59] incorporate heterogeneous surface chemistry and electrochemistry with elementary mass-action kinetics.

This study builds upon the 1-D isothermal model developed by previous studies, in particular by DeCaluwe et al. [38, 58], and extends it to simulate syngas at

various compositions described in more detail in chapter 3. The model also incorporates a 'leakage mechanism' to account for the discrepancies encountered in OCV observed in the experiments and the OCV predicted from the porous electrode model. Further, the effects of various parameters like tortuosity, porosity, three phase boundary length, the specific catalyst area and the effect of operating temperature on the cell performance have been investigated. Attempts have also been made to gain insight into the difference in OCVs observed between Ni/YSZ and Ni/CeO_2/YSZ cells and how this can be attributed to micro-structural parameters. In addition, the current model extends DeCaluwe's efforts by adding the energy equations to explore the effects of non-isothermal conditions particularly when internal reforming occurs within the anode support layer.

4.1 Importance of Micro-structural Parameters

A lot has been already discussed about various parameters of the SOFC that control the micro-structures of its various components. It is useful to visualize what these parameters mean to be able to predict the performance of the cell based on changes in these parameters. The most important aspect of doing this exercise is to predict the optimum micro-architecture of the SOFC components that can provide high performance, enabling the manufacture and subsequent testing of this optimized geometry. Figure 4.1 helps visualize these parameters in detail:

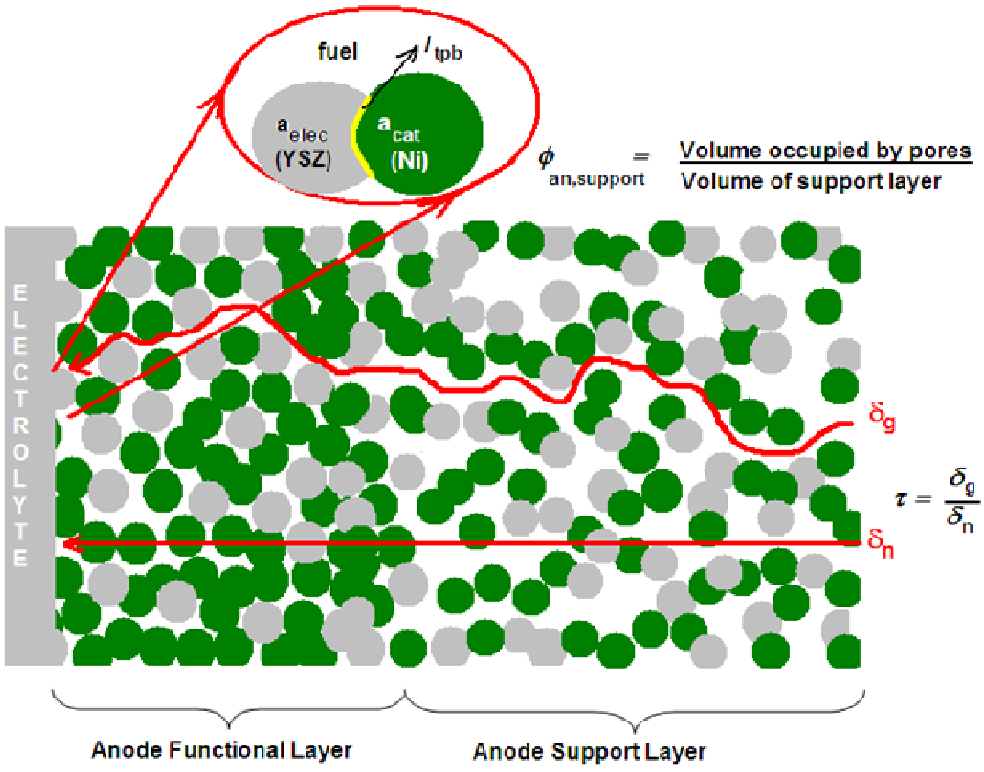

Figure 4.1 An illustration of the micro-architecture of the SOFC anode. Shown here are three important parameters porosity, tortuosity and the three phase boundary length.

φ is the measure of how much of total volume of the electrode is available for the gas phase species to penetrate down to the electrochemical region of the electrodes. It can vary through the depth of SOFC electrodes and usually different values are desired in support layers and functional layers. The current model has the capability to define variable porosities for different layers. τ, as indicated by Figure 4.1 is a measure of the diffusion path length (δ_g) through the pores relative to the linear length (δ_n). τ tends to increase with decreasing porosity as discussed in

DeCaluwe et al. [38]. Third important micro-structural parameter that has a direct bearing on the performance of the cell is l_{TPB}. TPB has been already discussed in previous sections and is the actual length where the electrolyte, the electrocatalyst (electron-conducting) and the reactant species come in contact and the charge transfer reactions take place.

4.2 Isothermal Model Formulation

The model is based on transient integration of differential algebraic equations which solve for, pressure P, species fractions (gas, bulk, and surfaces), and electric potential of the necessary phases in a finite volume discretization of the porous electrodes and the dense electrolyte. The model takes as the input an array of current densities from the user and performs transient integration over a sufficiently long time span to achieve steady state values for all the independent variables. The computational domain consists of the following seven different zones:

(i) anode channel flow passage, (ii) porous anode support layer (ASL), (iii) porous anode functional layer, (iv) dense electrolyte membrane, (v) porous cathode functional layer, (vi) porous cathode support layer, and (vii) cathode channel flow passage. A schematic representation of the button cell cross section along with different zones laid out above is shown in Figure 4.2.

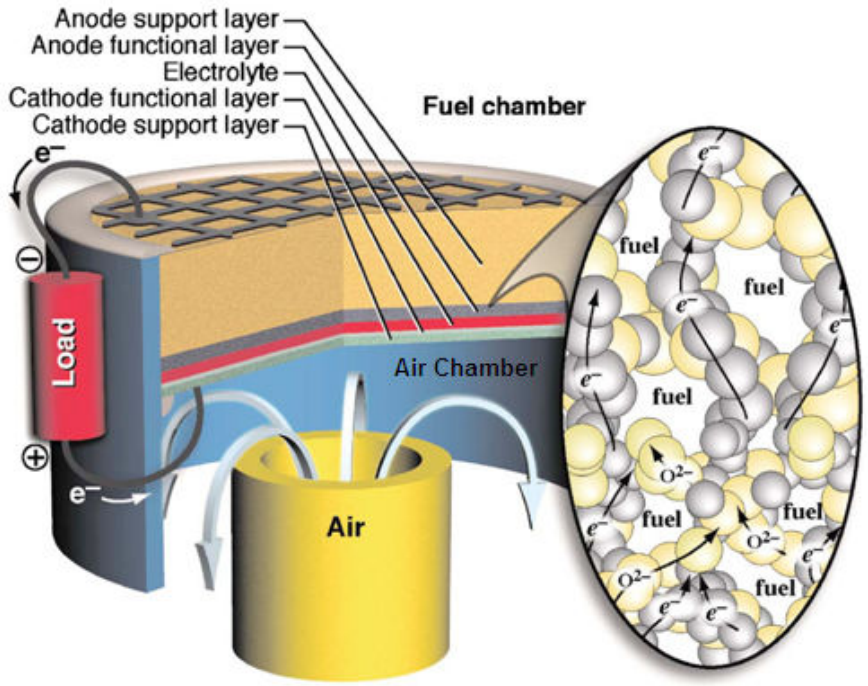

Figure 4.2 Schematic of a typical button cell illustrating ion and electron current paths near the interface between anode support and functional layers as sketched by Prof. R.J. Kee [11].

As explained in chapter 2, the thickest component of the fuel cell is the anode support layer (~ 1 mm). The anode functional layer and the electrolyte are of comparable thickness (~20 µm), followed by the cathode which is ~50 µm thick. The model is set up in such a way that it is possible for the user to define a functional layer for the cathode side as well, in addition to adjusting the thicknesses of all the components. The other parameters that are pre-defined before the simulation procedure begins are the geometrical parameters (τ, φ, a_{cat}, a_{elec}, three phase boundary lengths l_{TPB}) for both the electrodes along with their functional layers and the electrolyte conductivity. Also given as a user input is the cell operating temperature.

The computational zones are discretized into finite volumes (or slices) with anode and cathode fuel channels providing boundary conditions for each of the two porous electrodes. This boundary condition is based on a transport flux of species and mass to/from the channel to the electrode. For the current model, the closest discretized slice of the anode functional layer next to the electrolyte is assumed to sustain all of the electrochemical reactions and is referred to henceforth as the 'utilization thickness', δ_{util}. Models developed by Janardhanan and Deutschmann [33] incorporated a fixed utilization thickness which was provided as a user input to the model. DeCaluwe et al. [38, 58] showed that a fixed utilization thickness tended to over predict the cell performance at near limiting current densities, and some recent models [DeCaluwe and Zhu & Kee] incorporate distributed electrochemistry model where δ_{util} is calculated by the number of cells participating in electrochemistry through the functional layer. DeCaluwe showed that the utilization thickness parameter $\delta_{util,anode}$ tends to vary with changes in $\varphi_{g,anode}$ because changes in mass-transport resistance impact gas-phase concentrations and surface activity within the anode functional layer. While this is a more realistic approach to modeling, it is computationally expensive. Since a study over a wide parameter space with complex carbonaceous fuel chemistry was desired here, the more computationally efficient 'fixed utilization thickness' model was used to study trends in the performance of the Ni/YSZ and Ni/CeO_2/YSZ anodes in this study. Another factor that justifies the use of 'fixed utilization thickness' model besides savings in computational effort is the high value (60%) of $\varphi_{g,anode}$ used to simulate syngas performance. DeCaluwe's model

[38, 58] shows that at high $\varphi_{g,anode}$ (around 57%), the model fits the experimental data from Zhao & Virkar [39] closely.

4.2.1 Mass and Species Conservation Equations

High operating temperatures of SOFCs allow the gas phase to be modeled as ideal gas. In this model, the mass and gas-phase species conservation equations are based on the partial differential equations as formulated here in Equations 4.1 and 4.2.

$$\varphi \frac{\partial \rho}{\partial \tau} = \sum_{k=1}^{k=k_{gas}} \left(-\nabla J_k + W_k \left(a_{cat} \dot{s}_{k,cat} + a_{elec} \dot{s}_{k,elec} \right) \right) \quad \text{Eq. 4.1}$$

$$\varphi\rho \frac{\partial Y_k}{\partial t} = -\nabla J_k + W_k \left(a_{cat} \dot{s}_{k,cat} + a_{elec} \dot{s}_{k,elec} \right) - Y_k \sum_{k=1}^{k=k_{gas}} \left(-\nabla J_k + W_k \left(a_{cat} \dot{s}_{k,cat} + a_{elec} \dot{s}_{k,elec} \right) \right)$$

Eq. 4.2

The gaseous state is defined by the user-specified temperature T, density ρ, and the gas-phase mass fractions Y_k. Term φ is the porosity, J_k are the gas-phase mass fluxes for gas-phase species k, the specific areas (area per unit volume) available for catalytic and electrochemical charge-transfer reactions are a_{cat} and a_{elec}, respectively and molecular weight for species k is W_k. K_{gas} represents the total number of gas-phase species and $\dot{s}_{k,elec}$ & $\dot{s}_{k,cat}$ are molar production rates of gas-phase species k by heterogeneous reactions on the catalyst and electrolyte surfaces respectively. Species

mass fractions are also subjected to the constraint that they all add up to 1. Equation 4.3 describes the conservation of surface species:

$$\frac{\partial \theta_{k,m}}{\partial t} = \frac{1}{\Gamma_m}\left(\dot{s}_{k.m} + \frac{l_{TPB}}{a_m} \dot{s}_{k,m,tpb} \right) \qquad \text{Eq. 4.3}$$

The surface coverages $\theta_{k,m}$ for species k on phase m (electrolyte or catalyst) depend on Γ_m, the available surface sites per unit area, $\dot{s}_{k,m}$ & $\dot{s}_{k,m,tpb}$ the surface production rates per unit area a_m and charge-transfer reaction rates per unit length of three-phase boundary l_{TPB}. Equation 4.4 describes the conservation of charge in phase m assuming that all charge-transfer reactions take place within a single finite volume adjacent to electrode/electrolyte interfaces:

$$C_{dl} \frac{\partial \Delta\Phi_{el}}{\partial t} - \frac{\partial}{\partial y}\left(\sigma_m^e \frac{\partial \Phi_m}{\partial y} \right) = \pm l_{TPB} . i_{Far} \qquad \text{Eq. 4.4}$$

The charge balance in this finite volume incorporates the sources and sinks due to the Faradaic current i_{Far} (depending upon which electrode is considered) and the current densities due to electric potential gradients. The electric-potential difference between the catalyst phase electric potential Φ_{cat} and the electrolyte phase electric potential $\Phi_{\mathrm{electrolyte}}$ is defined as $\Delta\Phi_{\mathrm{el}} = \Phi_{\mathrm{cat}} - \Phi_{\mathrm{electrolyte}}$. The effective conductivity of phase m per unit of geometric area is represented as σ_m^e. The double layer capacitance per unit

total volume C_{dl} [units of F/m^3] is a fitting constant in this model and its value can be extracted from equivalent circuit modeling of experimental data [47]. The value of C_{dl} does not have to be accurate as the model only uses this value in transient calculations of the electric potential difference and the steady state value is not affected. The Faradaic current density i_{Far} (the local charge-transfer rate between phases at the three-phase boundaries) is calculated from the charge-transfer reaction rates $\dot{s}_{k,m,tpb}$. The ± sign on the right side of Equation 4.4 depends on whether the particular phase in the composite electrode has a Faradaic current that is producing or consuming electrons.

As this model utilizes a fixed δ_{util}, under steady-state conditions therefore, electronic and ionic currents are non-existent (i_{Far} = 0 and i_{O2-} = 0) outside of the electrochemically active region, and hence $\partial \Phi_{electrolyte}/\partial y$ = 0. Thus, the electric potential in the catalyst phase reduces to Ohm's law according to Equation 4.5:

$$i_{ext} = \sigma_m^e \frac{\partial \Phi_m}{\partial y} \qquad \text{Eq. 4.5}$$

In the equation above, i_{ext} is the external current density, which is a user-specified boundary condition. In this model, σ_m^e for the porous electrode structures are calculated using a simple Bruggman correlation [68] where $\sigma_m^e = {\varphi_m}^{3/2}$. $\sigma_{m,bulk}$ in which φ_m is the volume fraction of conductive phase m and $\sigma_{m,bulk}$ is the bulk

conductivity of phase m. The user-specified i_{ext} determines the gradient in Φ_{cat} at the fuel/air chamber interface. Application of Equation 4.5 over the entire volume of the electrode requires that the ionic current (i_{O2-}) at the electrode/electrolyte interface matches i_{ext}.

For this model where the utilization thickness is constant, integrating equation 4.4 in the utilization thickness volume and then enforcing the boundary condition given by equation 4.5 throughout the entire volume of the electrodes and electrolyte for sufficiently long time determines the cell potential at steady state, $V_{cell} = \Phi_{cathode,int} - \Phi_{anode,int}$ the subscript *'int'* refers to the interface between the fuel/air flow channels and the respective electrode surfaces.

This model assumes that the electrolyte processes have a very fast equilibration time relative to the electrode processes. Hence, the transient changes in the local bulk electrolyte composition can be neglected. This assumption is corroborated by the fact that impedance spectroscopy data show that the bulk resistance (contributed by the electrolyte) matches the high frequency impedance obtained by the intercept of the high frequency arc on the real impedance axis.

4.2.2 Gas Phase Transport Equations

Within the porous electrode matrix, the gas phase mean-free-path length can be comparable to the average pore diameter of the porous electrode and hence, the effects of Knudsen diffusion and Darcy flow must be considered. DGM mentioned in the introduction to this chapter describes an implicit relationship among the gas-phase

molar concentrations, concentration gradients, molar fluxes, and the pressure gradient. As reported by Zhu & Kee [59], this relationship can be inverted to provide the gas-phase species mass flux j_k as the following:

$$J_k = -W_k \left[\sum_l \left(D_{DGM,kl} \frac{\partial [x_l]}{\partial y} \right) + \sum_l \left(\frac{D_{DGM,kl} [x_l]}{D^e_{kn,l}} \right) \frac{B_g}{\mu} \frac{\partial P}{\partial y} \right] \qquad \text{Eq. 4.6}$$

In this equation, $[X_l]$ is the molar concentration of species l, B_g is the permeability (evaluated according to the Cozeny–Karman relationship [59]), μ is the mixture dynamic viscosity, P is the pressure, and $D^e_{kn,l}$, is the effective Knudsen diffusion coefficient for species l. The effective DGM diffusion coefficients are determined as a matrix inverse $D_{DGM,kl} = H^{-1}$, where the elements of the matrix H are:

$$h_{kl} = \left[\frac{1}{D^e_{kn,k}} + \sum_m \frac{x_m}{D^e_{km}} \right] \delta_{kl} + (\delta_{kl} - 1) . \frac{x_k}{D^e_{kl}} \qquad \text{Eq. 4.7}$$

The effective ordinary multi component diffusion coefficients are calculated according to Equation 4.8 and the effective Knudsen diffusion coefficients are evaluated according to Equation 4.9:

$$D_{km}^{e} = \frac{\varphi}{\tau} D_{km} \qquad \text{Eq. 4.8}$$

$$D_{kn,k}^{e} = \frac{2}{3} . \frac{\varphi}{\tau} r_p \sqrt{\frac{8\bar{R}T}{\pi W_k}} \qquad \text{Eq. 4.9}$$

r_p is the pore radius and $\bar{R}$ is the universal gas constant. It should be noted that both the ordinary and Knudsen diffusion coefficients are modified by the ratio φ/τ to reflect the impact of the porous media on diffusion velocities.

Equations 4.1 & 4.2 form a boundary-value problem whose solution requires 2 boundary conditions: one with the dense electrolyte interface and the other with bulk-gas channels (for each electrode). Since this model assumes the electrolyte to be a dense structure, $j_k = 0$ at the electrode–electrolyte interfaces. At channel electrode interfaces, mass transfer is determined by considering gas-phase mass-transfer boundary layer in the bulk gas. Flux-continuity at the interface is expressed as:

$$j_{k,\text{int}} - Y_{k,\text{int}} \sum_l j_{l,\text{int}} = \frac{Sh_k D_{k,mix}}{\delta_{ch}} \left(\rho_{ch} Y_{k,ch} - \rho_{\text{int}} Y_{k,\text{int}} \right) \qquad \text{Eq. 4.10}$$

In the above expression, the subscript '*int*' indicates the electrode/gas-channel interface and the subscript '*ch*' indicates the gas composition in the flow channel far from the interface. The mixture-averaged diffusion coefficient of species *k* with

respect to the mixture composition in the gas compartment is given by $D_{k,\mathrm{mix}}$. The Sherwood numbers Sh_k for each of the species are related to the flow field. The characteristic length scale δ_{ch} may be taken as the distance between the centre of the flow channel and the electrode interface. In this model, the resistance to gas transport in the bulk-gas boundary layer is small compared to the porous-media resistance and hence the results are found to be insensitive to the Sherwood number. Moreover, the interface composition is nearly equal to the bulk-gas composition.

4.2.3 Surface and Electrochemical Reaction Rates

This model simulates the surface reactions (for the species absorbed on the electrode surfaces) and the edge reactions (responsible for charge transfer along the three phase boundary length). All the reactions are simulated as reversible reactions, with rates calculated using the Cantera software package according to mass-action kinetics [60]. For reversible reactions, Cantera uses user-specified forward-reaction rate coefficients and thermodynamics to evaluate the reverse reaction rate coefficients. For adsorption–desorption reactions, forward (adsorption)-rate coefficients are calculated as sticking coefficients.

$$k_{fwd} = \frac{s_0}{\Gamma_m^v}\sqrt{\frac{\overline{R}T}{2\pi W_k}} \qquad \text{Eq. 4.11}$$

In the above expression, s_0 is the sticking probability and ν is the sum of the surface adsorbates' stoichiometric coefficients. The forward-rate expressions for other surface reactions are described in Arrhenius form as:

$$k = AT^{\beta} \exp\left(\frac{-E_a}{\overline{R}T}\right) \quad \text{Eq. 4.12}$$

According to Bessler et al. [34], the rate expressions for edge reactions involving charge transfer follow from mass-action kinetics as:

$$k_{fwd} = k^*_{fwd} \exp\left(\frac{-\alpha_{fwd} n_{el} F \Delta\Phi_{el}}{\overline{R}T}\right) \quad \text{Eq. 4.13}$$

$$k_{bwd} = k^*_{bwd} \exp\left(\frac{-\alpha_{bwd} n_{el} F \Delta\Phi_{el}}{\overline{R}T}\right) \quad \text{Eq. 4.14}$$

The thermal components of the rate expressions, k^*_{bwd} and k^*_{fwd}, are expressed in Arrhenius form, as in Equation 4.12. The Faraday constant is given by F. The forward and backward charge transfer coefficients are α_{fwd} and α_{bwd}.which follow the stipulation for elementary reactions that $\alpha_{fwd} + \alpha_{bwd} = 1$. The number of electrons transferred in a reaction is given as n_{el}.

The reaction rate of progress can then be evaluated as follows:

$$q_i = k_{i,fwd} \prod_k^{ktot} [X_k]^{\nu'_{ik}} - k_{i,bwd} \prod_k^{ktot} [X_k]^{\nu''_{ik}} \quad \text{Eq. 4.15}$$

In the expression above, ν'_{ik} and ν''_{ik} are the stoichiometric coefficients of species *k* for reaction *i* in the forward and backwards directions, respectively, and $[X_k]$ is the generalized activity of species *k*. The generalized activity for gas-phase species is the molar concentration, and the activity for surface species is the site density. That is, for surface species where ζ_k is the number of sites occupied by species *k*. In the present study, each surface species occupies one site, $\zeta_k = 1$.

$$[X_k] = \frac{\theta_k \Gamma_m}{\zeta_k} \quad \text{Eq. 4.16}$$

The net rate of species production $\dot{s}_k$ depends upon summing the rate-of-progress q_i over all reactions, where $\nu_{i,k} = \nu'_{ik} - \nu''_{ik}$ is the net stoichiometric coefficient of species *k* in reaction *i*

$$\dot{s}_k = \sum_i \nu_{i,k} q_i \quad \text{Eq. 4.17}$$

As far as the non-electrochemical reactions on the Ni anode catalyst are concerned, kinetic rate parameters are adopted from Janardhanan and Deutschmann

[36]. The forward kinetic parameters and thermodynamics for charge-transfer reactions on a Ni/YSZ anode and for surface reactions on the YSZ surface are taken from Goodwin and Bessler's work [33, 34, 61]. Finally, the kinetic rate parameters for O_2 reduction on an LSM–YSZ cathode are derived from fitting data reported by Jiang et. al. [46] and tabulated in DeCaluwe et al. [38].

Simulation of an SOFC LSV curve required a series of steady-state calculations for a range of user specified current densities i_{ext}. In transient form and after finite-volume discretization of the spatial operators, the system of governing equations and boundary conditions forms a system of differential-algebraic equations (DAEs). The DAE system is solved using Matlab's stiff ordinary differential solver function ode15s. For each i_{ext} the solution is determined by integrating the transient system to a steady state. For the baseline set of 'fixed δ_{util} model' parameters, the simulation completed a sweep of 30 steady-state calculations, with the maximum i_{ext} of 1.2 A/cm^2, in a time range of 25 minutes – 30 minutes (depending on the particular case of fuel inlet conditions) on a 3.0 GHz dual core processor.

4.3 Leakage Model

Although the 'through the MEA' model incorporates porous composite electrodes and electrochemical charge transfer reactions in the three phase boundary region near the dense electrolyte, it tends to over-predict the performance particularly when it comes to the open circuit voltage. Since the model assumes a 'dense' electrolyte, the fuel and oxidant remain in their respective electrode functional layers and undergo oxidation and reduction respectively without any leakage across the

electrolyte. In reality, this is not the case; the sintering of the electrolyte typically can leave pores in the structure, called “pinholes”. During operation, reactants can leak through theses pinholes. In the current study, the higher flow rates on the cathode side tend to result in a higher pressure on the cathode resulting in oxidant leaking from the cathode to the anode side. Figure 4.3 shows the SEM image of the cross section of electrolyte with pinholes. On the left side of the electrolyte is the cathode and on the right side is the anode functional layer.

The leakage of oxygen to the anode leads to direct combustion of fuel and production of steam and CO_2 in the anode pores. The combustion lowers the measured OCV since the partial pressure of the reactants is reduced and simultaneously the partial pressure of products increases. According to Nernst equation, this results in a decrease in the OCV, as seen from the experimental data.

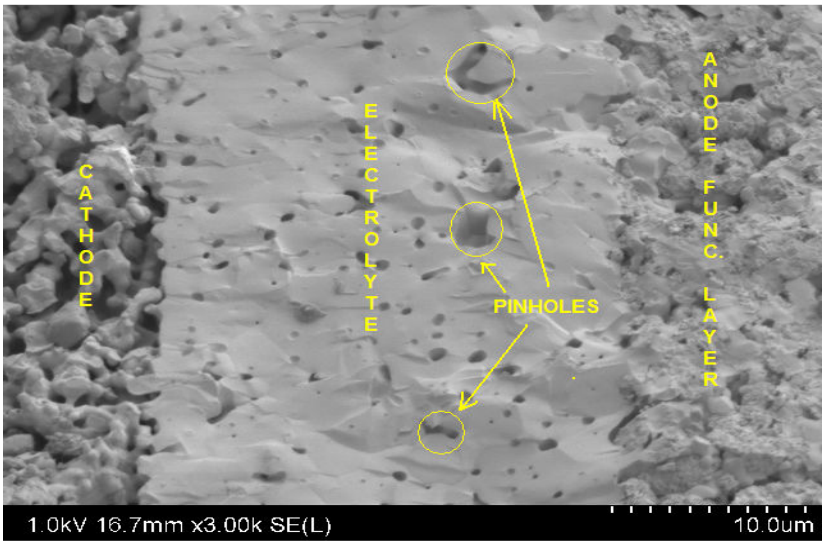

Figure 4.3 SEM image of the Ni/YSZ cell microstructure post testing showing pinholes in the dense electrolyte.

Gas leakage across the electrolyte pinholes was incorporated into the MEA model to account for the difference in OCVs in experimental data. A number of simulations were first run with the MEA model without accounting for any gas leakage by changing the micro-structural parameters of porosity, tortuosity, three phase boundary length and catalyst specific area for each electrode for the case of 1:1 H_2:Ar with 3% H_2O. The fit that was the closest to the experimental data (neglecting the difference in OCV, so that the experimental data and the model curves were almost parallel) was isolated. The cathode and anode overpotentials of this fit were added to find the total concentration overpotential, η_{conc}. As explained earlier, the leakage will further increase η_{conc}. Hence, the difference in measured and modeled OCV is matched to the value of η_{conc} at zero current which is attributed entirely to the leakage across the electrolyte. An effective current density needed to create the calculated value of η_{conc} is defined as the "leakage current". The leakage current defines an effective flux of oxygen through the electrolyte pinholes which is modeled effectively as a diffusive flux with an effective diffusion coefficient as calculated here in Equation 4.18:

$$\frac{D_{pinhole}}{\delta_{elec}} = \frac{i_{leak}}{4F} \frac{\overline{RT}}{\Delta P_{O_2,elec}} \qquad \text{Eq. 4.18}$$

Here, D_{pinhole} is the effective diffusion coefficient of oxygen through the electrolyte pinhole, δ_{elec} is the electrolyte thickness, i_{leak} is the leakage current, and $\Delta P_{\text{O2,elec}}$ is the oxygen partial pressure difference across the electrolyte (difference between either electrode layers adjacent to the electrolyte). From the fit obtained by running the no-leakage MEA model, $\Delta P_{\text{O2,elec}}$ term can be obtained. The anode side will consume all oxygen diffusing across the pinholes to start with, $P_{\text{O2,anode}}$ approaches 0. (Equilibrium $P_{\text{O2,anode}}$ for typical fuel/combustion product mixtures are on the order of 10^{-21} bar.) Thus, the $\Delta P_{\text{O2,elec}}$ term can easily be approximated as the $P_{\text{O2,cathode}}$ at the cathode/electrolyte interface. Once the diffusion coefficient is known, the molar flux of oxygen to the anode side can be calculated via the following equation:

$$\dot{n}_{O_2} = \frac{D_{pinhole}}{\delta_{elec}} \cdot \frac{\Delta P_{O_2,elec}}{\overline{R}T} \qquad \text{Eq. 4.19}$$

This molar flux is then used to adjust the partial pressures on the anode and cathode sides. Since each mole of O_2 that leaks over to the anode side combines with 2 moles of H_2 to produce two moles of H_2O, the source terms for species production are appropriately adjusted in the electrochemically active layer of each electrode. Figure 4.3 shows the discrepancy in OCV in the no-leakage model and the experiment and how the leakage model accounts for this discrepancy.

The effects of oxygen leakage have been modeled as a gas phase reaction in this model. It was initially thought that oxygen could just be allowed to leak through

to the anode and given time to be adsorbed on the catalyst surface, which would then undergo electrochemical reaction with the adsorbed fuel. But it was found that this resulted in the voltages corresponding to initial lower current densities to increase slightly more the OCV and then follow a steady decline (for higher current densities. It also resulted in slightly inferior fits compared to if the leakage was modeled as a gas phase reaction in which the fuel and the leaked oxygen underwent combustion instantly, a valid assumption given the operating temperatures of ~ 800 °C. This resulted in the fits produced by the leakage model to match better with the experimental data and the voltages decreased monotonically with all current densities following the OCV.

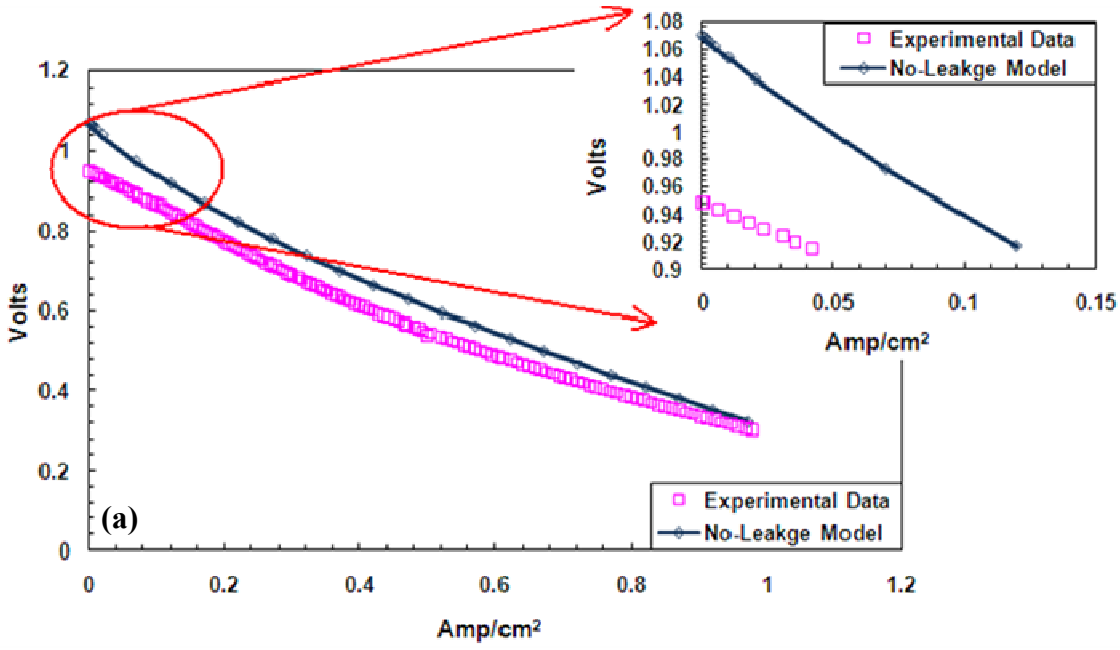

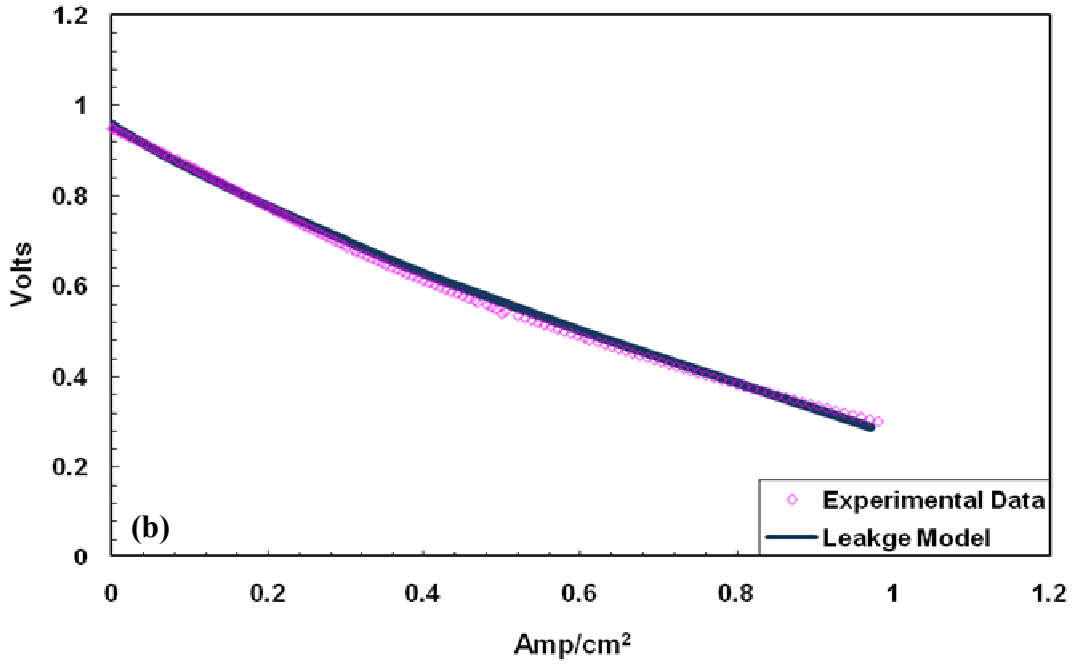

Figure 4.4: Comparison of VI curves for the experimental data and the model results for the case of 1:1 H_2:Ar with 3% H_2O. a) shows the difference in OCV between the two sets by using the no-leakage model and b) shows the effect of the leakage model in matching the OCVs for both sets. T_{cell} for this simulation was 800 °C.

The task of arriving at the microstructure for the fits that matched the measured performance closely (within $\chi^2 = 0.03$) was challenging. The reason for this was that a particular simulation for the no-leakage model (with a set of micro-structural parameters) would provide a particular value of the leakage current.. However, in order to fine tune the fits to match the experimental data closely, one or more of the micro-structural parameters would be changed. This would imply that one had to go back to the no-leakage model with this new set of parameters to obtain

a new leakage current. This procedure was continued until a particular value of leakage current provided the fits which were in close agreement with the experimental data through the use of leakage model. The quality of the fits was quantitatively described as the chi-squared statistic:

$$\chi^2 = \sum_{i=0}^{i=i_{\max}} \frac{\left\{V_{model}(i) - V_{expt}(i)\right\}^2}{V_{model}(i)} \qquad \text{Eq. 4.20}$$

In Equation 4.20 above, χ is the quality of the fit, $V_{model}(i)$ is the value of the voltage obtained from the leakage model for a particular current density i, $V_{expt}(i)$ is the value of the voltage obtained from experimental data for the same current density i, and i_{max} is the maximum current density obtained in the experiment for a particular case of flow conditions. The fits for various flow conditions and the effects of parameters on the performance of the cell are discussed in the following section.

4.3.1 Results of the leakage model

The following figures show the results of the leakage model when run using the fuel conditions for H_2/Ar flow and syngas conversions as listed in Table 3.1. The fits are shown along with the corresponding experimental data to show the chi-squared goodness of the fits. Following the procedure described in the section above on 'leakage model', a particular micro-structure was predicted by the model for all

the following fits. The micro-structural parameters were: porosity, $\varphi = 0.6$; tortuosity, $\tau = 3.5$; cathode three phase boundary length, $l_{TPB,cathode} = 6*10^{12}$ m/m^3 of the electrode; and the specific areas of catalysts for both cathode and anode, $a_{cat,anode}$ and $a_{cat,cathode} = 1*10^7$ m^2/m^3.

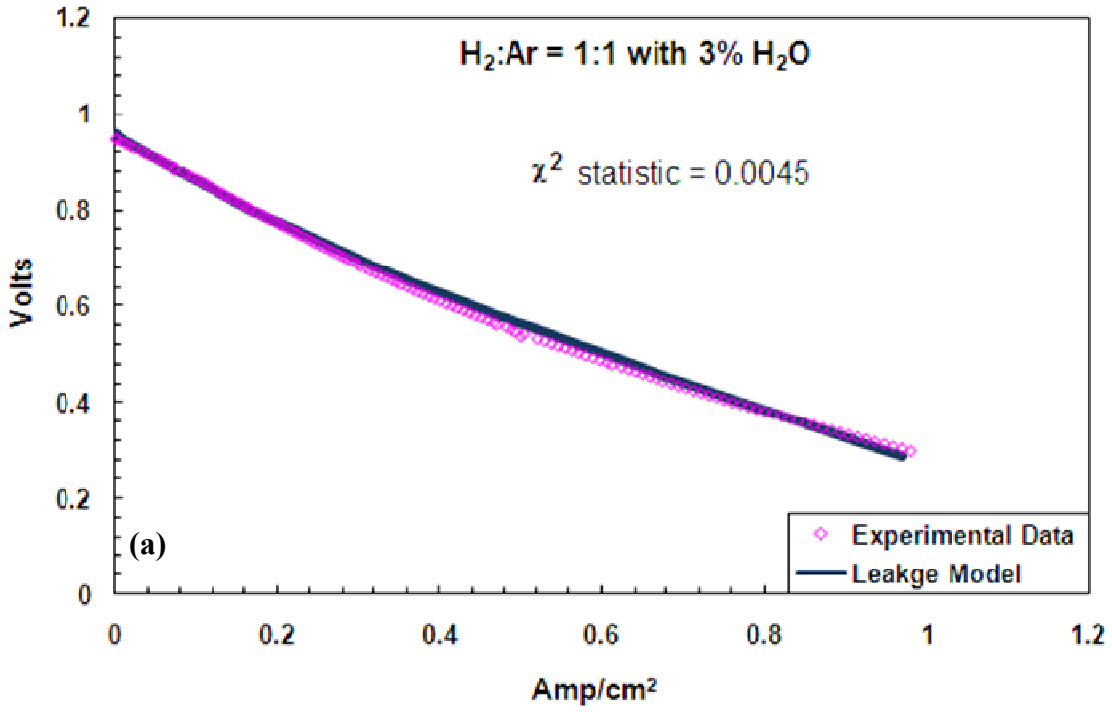

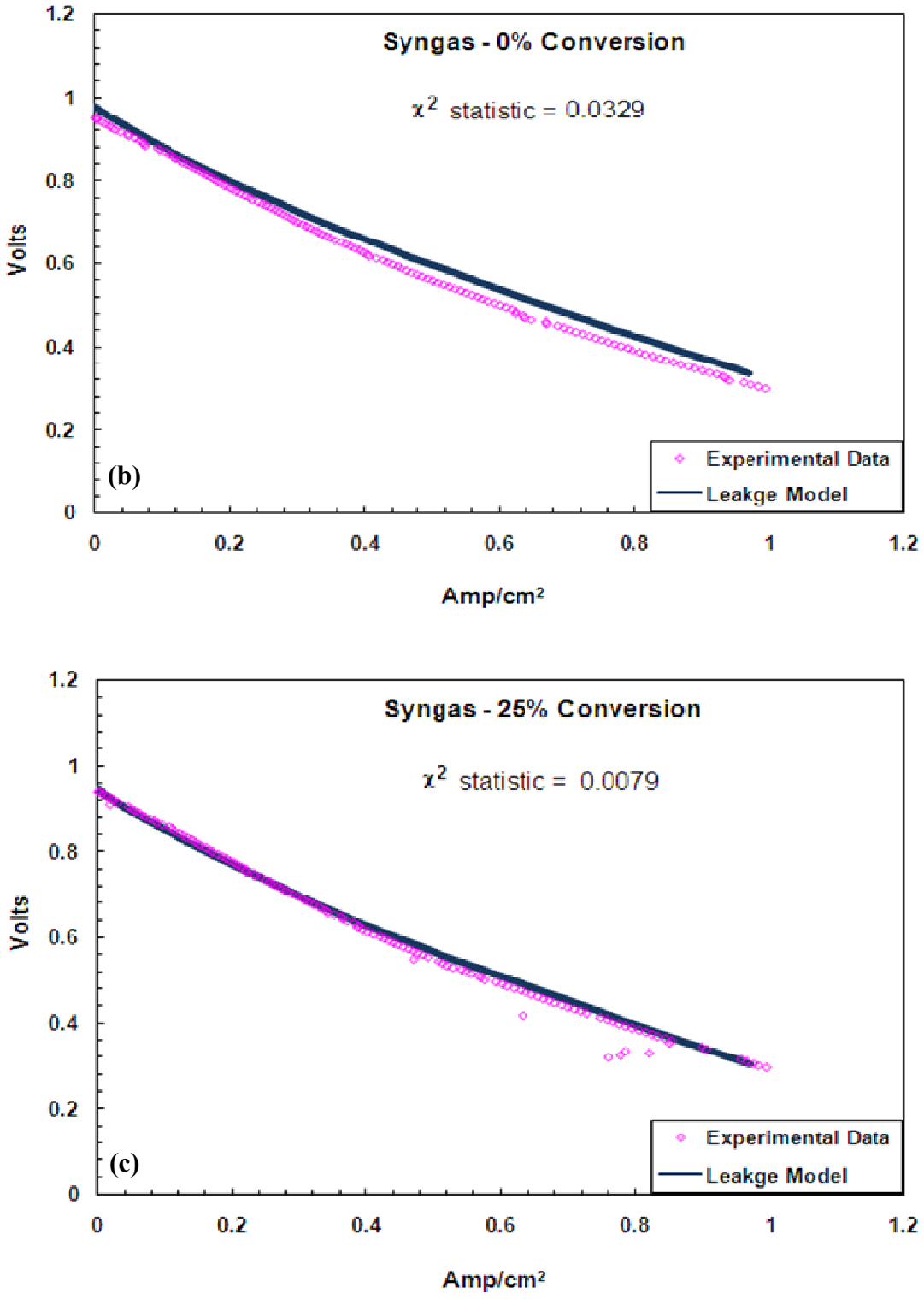

Figure 4.5 Comparison of the experimental data with the fits from 'leakage model' along with χ^2 statistics to show the quality of fits for: a) 3% humidified H_2/Ar (1:1);

(b) syngas with 0% conversion and (c) syngas with 25% conversion. T_{cell} = 800 °C for all cases.

4.3.2 Effects of micro-structural parameters on performance

It was one of the aims of this study to use the model as a guide in designing micro-architectures that would provide reasonable power densities for MEAs during testing. Two parameters each for either electrode ($\varphi_{g,anode}$ & $\tau_{g,anode}$ of the support layer and two cathode parameters $l_{TPB,cathode}$ and the $a_{cat,cathode}$) were chosen out of all the user provided parameters listed in Table 4.2 because they have the largest impact on $\eta_{conc,anode}$ and $\eta_{act,cathode}$. These two overpotentials are the most significant overpotentials for anode and cathode respectively. Since nickel has a significantly high catalytic activity, it is reasonable to assume that the activation overpotential (particularly for fuels such as H_2) is negligibly small as shown in Figure 4.6 (a). Hence, the total anode overpotential is almost entirely contributed by $\eta_{conc,anode}$. Since diffusion resistance is controlled by $\varphi_{g,anode}$ and $\tau_{g,anode}$ as explained through Equations 4.8 and 4.9, these two parameters are chosen as parameters that are most likely to impact the performance of the anode. Figure 4.6 shows the breakup of total overpotentials for either electrode in terms of activation and concentration overpotentials. As for the cathode, $\eta_{act,cathode}$ dominates the total cathode overpotential. Figure 4.6 (b) shows that this is indeed the case. The diffusion resistance encountered by the oxidant is very small since the cathode layer is extremely thin (~50 μm). This validates the assumption that the contribution of the cathode to the concentration overpotential is quite small. In the low current density

regime (i_{ext} < 0.3 A/cm^2) however, the activation overpotential for the cathode is quite significant. DeCaluwe's work [58] mentions that LSM is not a particularly good MIEC (mixed ionic electronic conductor) and there are high resistances associated with the O_2 reduction reactions. DeCaluwe's models [38] drawn from the work by Jiang et al. [46] use 160 kJ/mol for the activation energy associated with the charge transfer reactions over the LSM/YSZ TPB which is quite high. This further validates the assumption that the cathode parameter that is the likeliest to be used as a fitting parameter must be $l_{TPB,cathode}$. Another parameter that could likely influence $\eta_{act,cathode}$ is the catalyst loading in the functional layer, or $a_{cat,cathode}$ as explained in section 4.2.1 above.

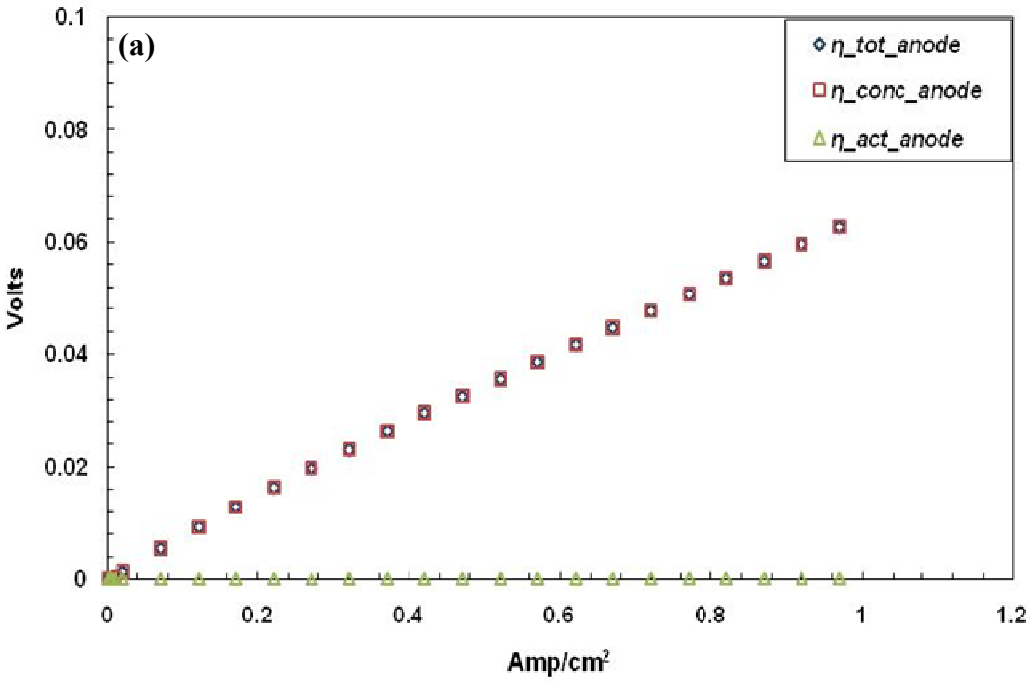

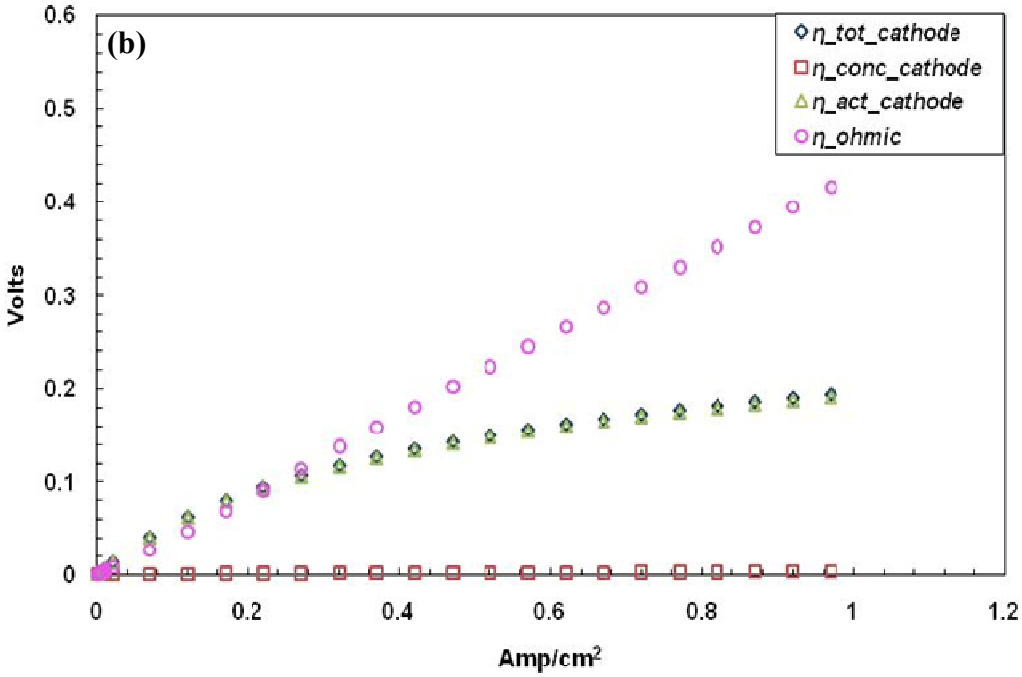

Figure 4.6: Overpotentials calculated by the model broken down into activation and concentration components for: (a) anode and (b) cathode. Also shown in part (b) is the η_{ohm} contributed by the electrolyte for comparison. T_{cell} = 800 °C for both part (a) & (b).

Modeling results in Figure 4.7 show how each of these parameters impact the cell performance and to what degree. It will be apparent that some parameters (like $l_{TPB,cathode}$ have a more significant impact than others (like $a_{cat,cathode}$). Since the model takes in these parameters as user-provided variables, a parametric study was carried out with syngas with 0% conversion as the baseline flow condition for studying the impact of micro-structural parameters on performance. The anode flow conditions are mentioned in Table 3.1. For cathode, air was used as oxidant. T_{cell} was maintained at 800 °C.

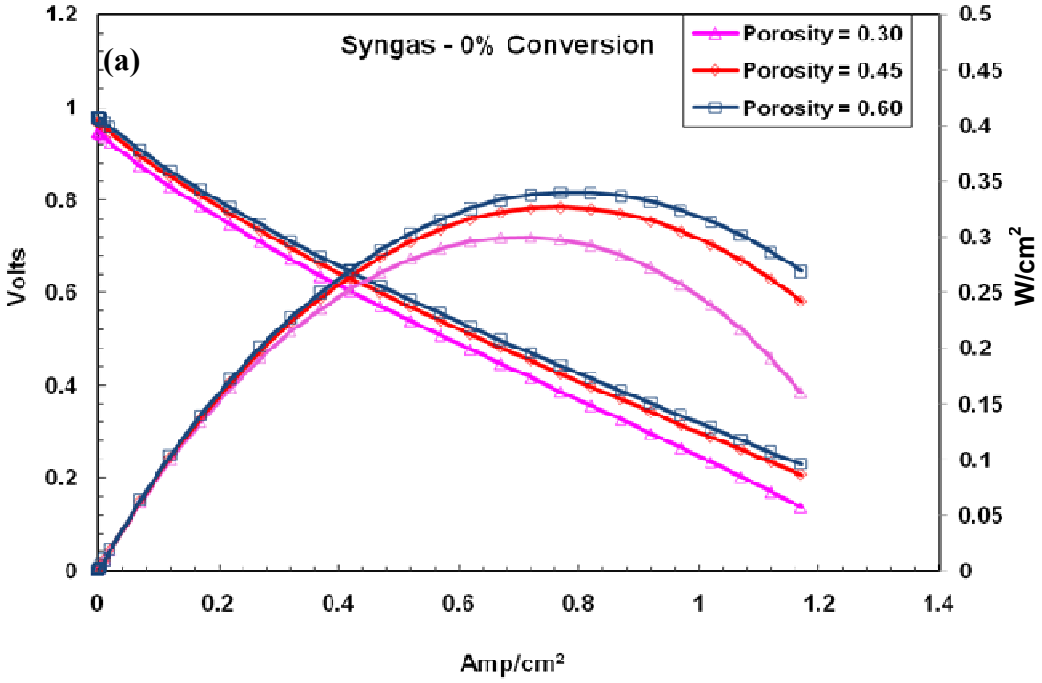
(a)
Syngas - 0% Conversion
Porosity = 0.30
Porosity = 0.45
Porosity = 0.60
Volts
W/cm2
Amp/cm2
0
0.2
0.4
0.6
0.8
1
1.2
1.4
0.05
0.1
0.15
0.25
0.3
0.35
0.45
0.5

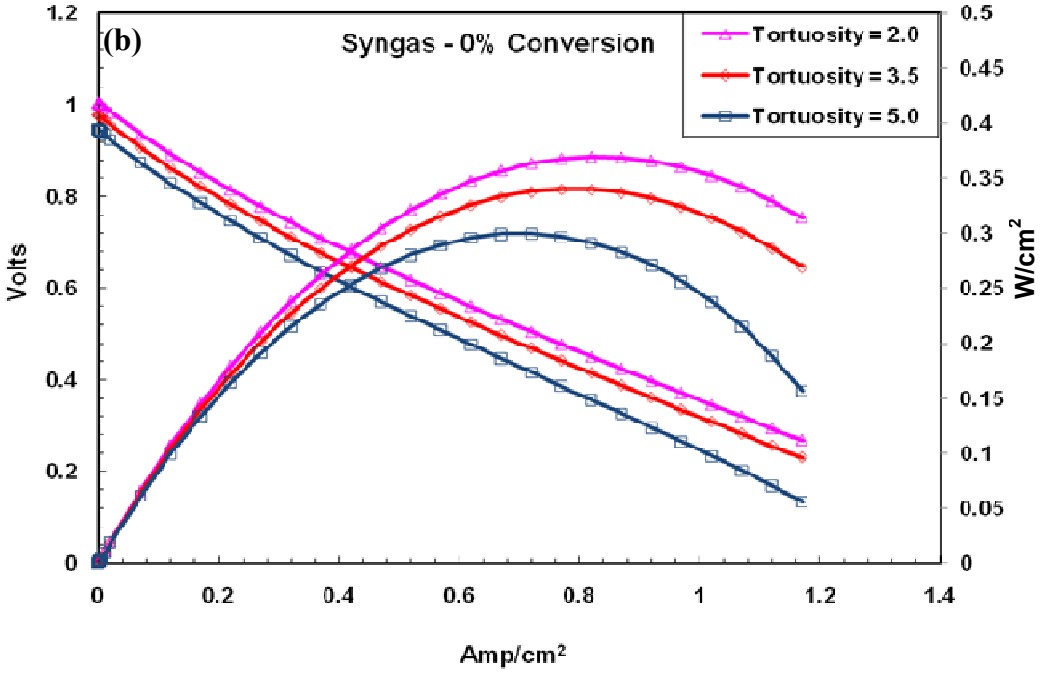
(b)
Syngas - 0% Conversion
Tortuosity = 2.0
Tortuosity = 3.5
Tortuosity = 5.0
Volts
W/cm2
Amp/cm2
0
0.2
0.4
0.6
0.8
1
1.2
1.4
0.05
0.1
0.15
0.25
0.3
0.35
0.45
0.5

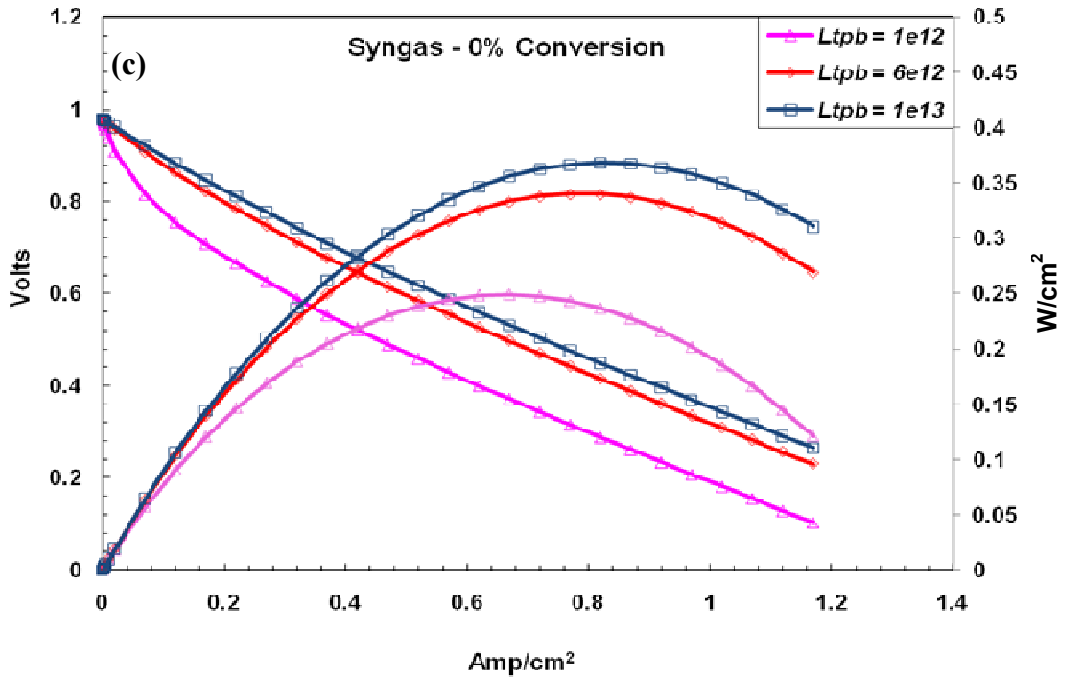
(c)
Syngas - 0% Conversion
Ltpb = 1e12
Ltpb = 6e12
Ltpb = 1e13
Volts
W/cm2
Amp/cm2
0
0.2
0.4
0.6
0.8
1
1.2
1.4
0.05
0.1
0.15
0.25
0.3
0.35
0.45
0.5

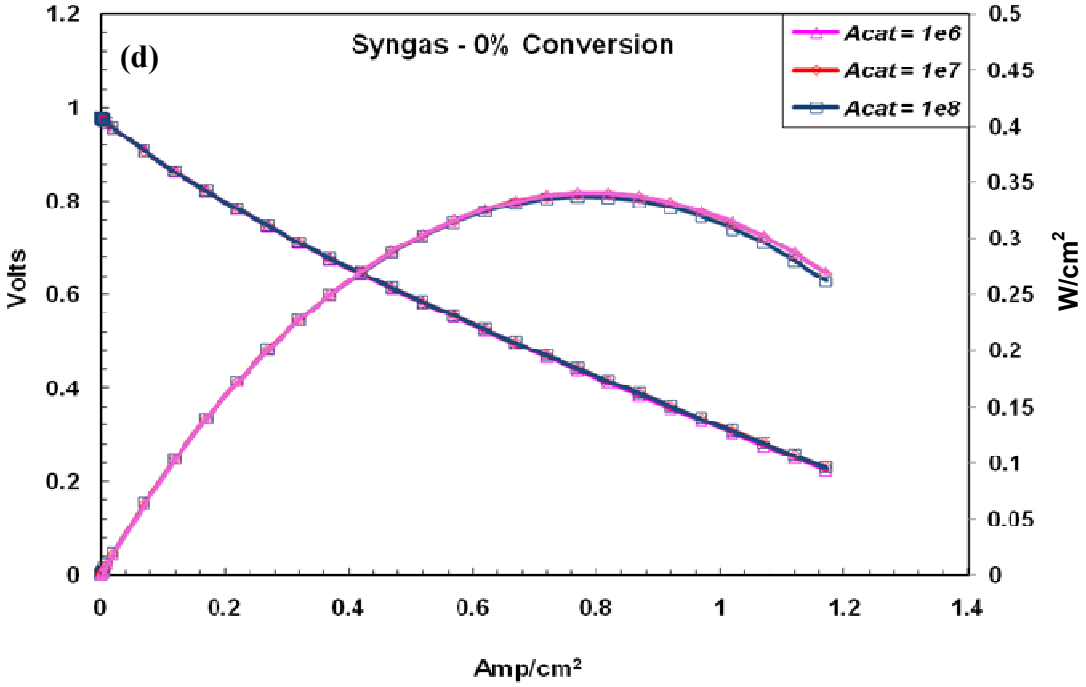
(d)
Syngas - 0% Conversion
Acat = 1e6
Acat = 1e7
Acat = 1e8
Volts
W/cm2
Amp/cm2
0
0.2
0.4
0.6
0.8
1
1.2
1.4
0.05
0.1
0.15
0.25
0.3
0.35
0.45
0.5

Figure 4.7 Effects on performance of various micro-structural parameters: (a) Porosity of anode support layer, (b) Tortuosity of anode support layer, (c) TPB (cathode) and (d) Catalyst Specific Area (cathode) (m^2/m^3 of electrode). T_{cell} for all cases was 800 °C. All simulations performed for syngas at 0% conversion.

The results of the leakage model, run at the leakage current i_{leak} of 0.6 A/cm^2 for the baseline values of $\varphi_{g,anode}$= 0.6, τ = 3.5, $l_{TPB,cathode}$ = 6*10^{12} m/m^3 and $a_{cat,cathode}$ = 1*10^7 m^2/m^3 (for instance, when one of these parameters was changed at a time, the other three were kept at their baseline values) shown in Figure 4.7 (a) show the impact of varying $\varphi_{g,anode}$ from 0.30 to 0.60, a range that is typical of practical MEA architectures [39, 52, 53]. Figure 4.7 (a) shows a relatively weak dependence on φ alone. Changing the porosity from 0.30 to 0.60 changes the maximum power density from 0.3 W/cm^2 to 0.34 W/cm^2 (an increase of around 13%). Figure 4.7 (b) shows a similar trend for τ when changed from 2.0 to 5.0, again a typical range encountered in practical MEAs [62]. A more tortuous path for the gas phase reactants to reach the electrochemically active regions would affect the performance negatively, which is what is observed in the model results. A decrease of about 19% in the maximum power density (from 0.37 W/cm^2 to 0.3 W/cm^2) is seen when increasing the tortuosity from 2.0 to 5.0. It may be noted that the OCV is also being affected by the change in tortuosity. This could be explained by the fact that the leakage current depends strongly on tortuosity (higher the tortuosity, higher is the i_{leak}). The above results however have all been simulated for a fixed i_{leak} (and hence the discrepancy in OCV). Figure 4.7 (c) shows how important the TPB for cathode is with regard to cell

performance. A strong dependence of the activation overpotential on the TPB length affects the cell performance drastically. Increasing $l_{TPB,cathode}$ from $1*10^{12}$ m/m^3 to $1*10^{13}$ m/m^3 boosts the performance by 48% (an increase from 0.25 W/cm^2 to 0.37 W/cm^2). Lastly, catalyst loading on the cathode seems to have almost no impact on the performance, as reveled by Figure 4.7 (d). This seems to suggest that the values for $a_{cat,cathode}$ used in this model [38] are sufficient in magnitude to not impact performance in spite of a change (increase or decrease) by an order of magnitude. Parameters utilized for calculating the values of a_{cat} (for either electrode) are consistent with predictions from random-packing numerical studies of composite SOFC electrodes [63].

It must be noted that these parameters are inter-related and changing of one parameter impacts another. For example, there is a negative correlation between $\tau_{g,anode}$and $\varphi_{g,anode}$ as reported by Williford et. al [62]. Distributed electrochemistry model with varying utilization thickness by DeCaluwe et. al. [38] shows that tortuosity must increase with decreasing porosity (and vice versa). It does follow intuitively, that removing solid particles to increase the void fraction should decrease the average path length of diffusing molecules. Their work also shows that the utilization thickness parameter δ_{util} for the anode may also tend to vary with changes in $\varphi_{g,anode}$.

Table 4.1 lists all the model parameters and their values used for the baseline case (1:1 H_2:Ar with 3% H_2O) which formed the basis of all the subsequent fits (for syngas) by zeroing in on a particular micro-architecture.

Table 4.1 Model parameters for baseline fit (humidified H_2/Ar with 3% H_2O)

	Anode	Cathode
TPB length, l_{TPB} [m^{-2}]	3e13	6e12
Average pore radius, r_p [μm]	0.5	0.5
Average particle diameter, d_p [μm]	2.5	2.5
Utilization thickness, δ_{util} [μm]	5	5
Support layer thickness [μm]	1000	50
Support layer porosity, φ_g	0.60	0.26
Support layer tortuosity, τ_g	3.5	2.9
Functional layer thickness [μm]	20	-
Functional layer porosity, $\varphi_{g,int}$	0.23	-
Functional layer tortuosity, $\tau_{g,int}$	4.5	-
Catalyst fraction of solid phase	0.6	0.47
Catalyst surface site density, Γ_{cat} [mol/cm^2]	1.66e-9	1.66e-9
Catalyst surface area a_{cat} [m^{-1}]	1e7	1e7
Electrolyte surface site density, Γ_{elec} [mol/cm^2]	1e-9	1e-9
Electrolyte surface area, a_{elec} [m^{-1}]	1e7	1e7
Double layer capacitance, C_{dl} [F/m^3]	0.003	0.2

4.4 Non Isothermal Model

When it comes to large scale systems like SOFC stacks, the issue of heat management and the heat generation (or consumption) over the entire stack assumes importance. This is especially important in case of hydrocarbon steam reforming which is endothermic in nature and can impact performances significantly, especially down the channel of the flow direction. Modeling studies by Janardhanan and Deutschmann [37] show that the variation in temperature from the inlet of the fuel cell channel to the exit along the axial direction can be as much as 50 K in case of

humidified (3% H_2O) methane. According to the authors, Within the MEA structure the resulting temperature profile is the net effect of heat absorbed or released as a result of heterogeneous chemical reactions, heat release due to the electrochemical reaction at the TPB, resistive heating within the electrolyte, convective heat transfer to and from the channels, and the radiative heat transfer with the interconnects. Near the inlet section, the temperature drops as a result of endothermic reforming reaction. However, further downstream the unit cell the temperature starts to increase as a result of exothermic cell reactions.

The above study also indicates the effects of the varying temperature profile down the channel on the reversible cell voltage and the current density. An increase of open circuit potential is seen with decreasing temperature, which is typical for hydrogen oxidation mechanism. However, down the unit cell length the reversible potential drops due to the increase in temperature as well as the increased fuel dilution due to the production of H_2O at the TPB. The current density begins to increase near the inlet, however, starts to decrease as temperature drops and as the temperature increases the current density also increases. These effects suggest the importance of incorporating the energy equations in any realistic SOFC model to include the non-isothermal effects, particularly in case of a down the channel configuration. This section, therefore deals with the effects of non isothermality in the button cell model discussed in the previous sections of this chapter.

In addition to the gas transport and species conservation equations described in section 4.1, the energy equation described by Equation 4.21 is incorporated in the solution vector of the DAE equations.

$$\overline{\rho C_p}\frac{\partial T}{\partial t} = -\sum_{k=1}^{k=k_{tot}}\left\{W_k\left(a_{cat}\cdot\dot{s}_{k,cat}\cdot h_k + a_{elec}\cdot\dot{s}_{k,elec}\cdot h_k\right) - \frac{\partial j_k h_k}{\partial y}\right\} + \frac{\partial}{\partial y}\left\{\left(\varphi\lambda_{gas} + (1-\varphi)\lambda_{solid}\right)\frac{\partial T}{\partial y}\right\} \quad \text{Eq. 4.21}$$

The above equation incorporates the effects of heat absorbed or released as a result of heterogeneous chemical reactions, heat release due to the electrochemical reactions at the TPB, heat diffusion through the electrode GDLs, conduction heat transfer through the GDL and the electrolyte and the resistive heating due to ionic and electronic flow inside the electrolyte and the electrodes. $\overline{\rho C_p}$ term is the effective specific heat capacity of the combined solid (catalyst surface and bulk) and gas-phase materials in each cell of the GDL. Other terms in the equation mean the same as they do in Equations 4.2 & 4.5 and h_k is the enthalpy (on a mass basis) of the species k. λ_{gas} is the thermal conductivity (in W/m-K) of the gaseous species combined and λ_{solid} is the thermal conductivity of the catalyst substance. The following boundary condition in Equation 4.22 closes out the system of equations:

$$-\lambda_{gas}\frac{\partial T}{\partial y} = \frac{Nu\cdot\lambda_{\text{int}}(T_{ch} - T_{\text{int}})}{d_{ch}} \quad \text{Eq. 4.22}$$

This boundary condition effectively states that the heat conduction inside the first discretized layer of the GDL is provided by the heat transfer from the electrode

channel through *Nu* number. Various *Nu* numbers were tried in this model and their effect was found to be negligible to the final results. A value of *Nu* = 4 is used in this study. λ_{int} is effective conductivity at the interface between the flow channel and the first GDL layer. This boundary condition suffices because the mass fluxes are defined at the interfaces of the GDLs. This automatically implies that the heat fluxes match across the channel-GDL interface (a condition ensured by the boundary condition for the mass flux Equation 4.2). Figure 4.8 below shows the non-isothermal effects for humidified hydrogen and humidified methane.

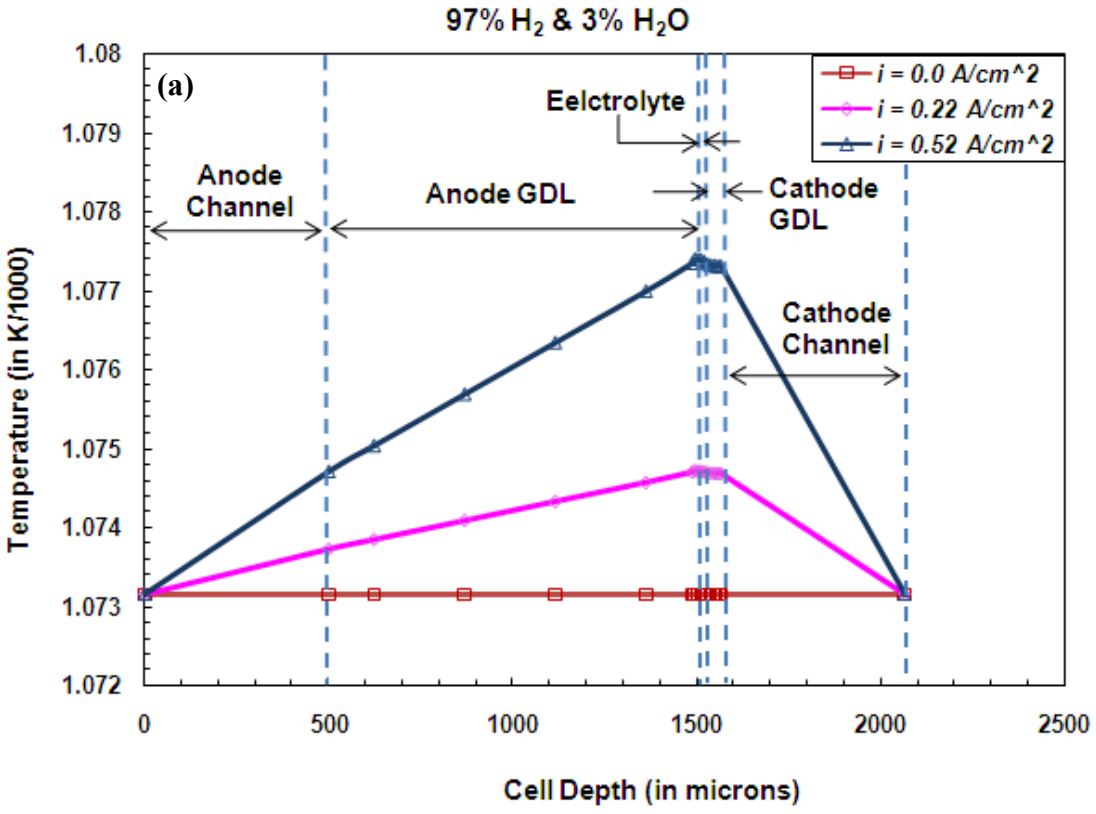

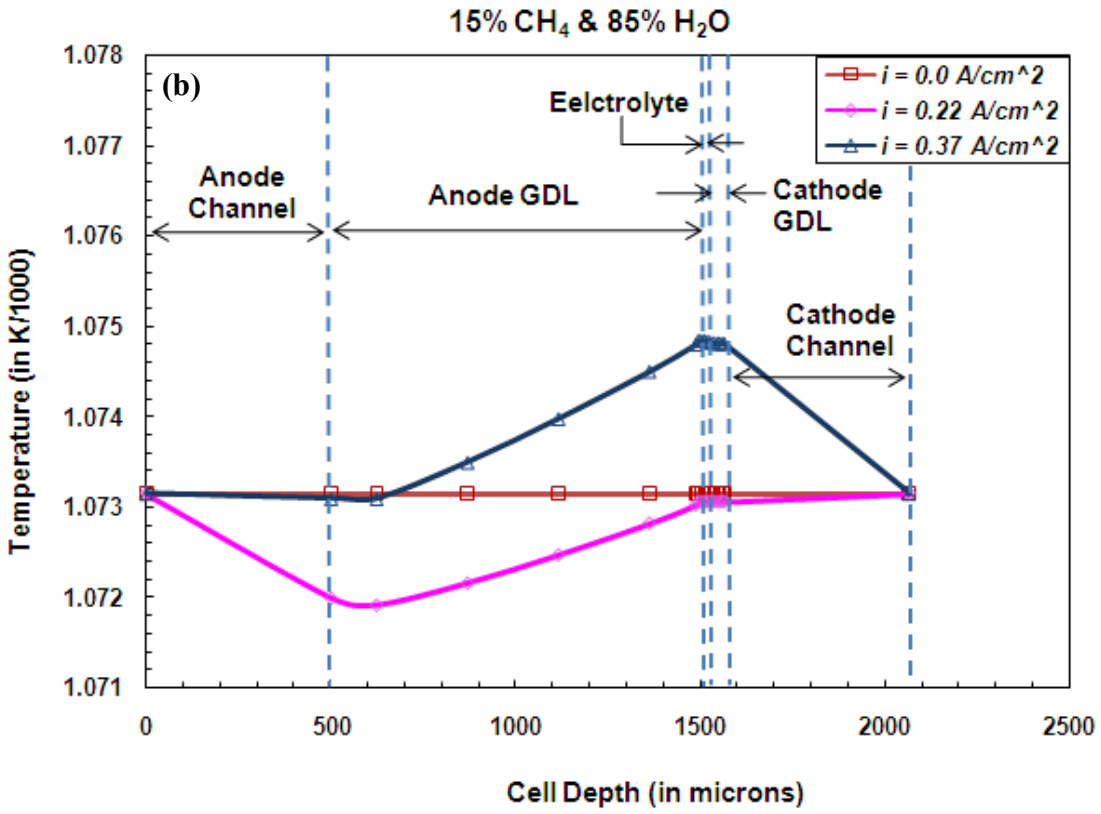

Figure 4.8 Temperature distribution through the MEA of the button cell SOFC starting from the mid-point of anode flow channel all the way through to the mid-point of cathode flow channel for three different current densities: (a) for humidified H_2 (3% H_2O) anode feeds and (b) for humidified CH_4 (85% H_2O) anode feeds.

As seen from the above figure, the effect of steam reforming is seen in that the temperature through the MEA is lowered initially (at lower current densities) and as methane is reformed to hydrogen, the temperature starts to rise (as seen in Figure 4.7) at higher current densities with more and more reforming going on.

One particular assumption that was used in this model for the effects of heat absorbed or released as a result of heterogeneous chemical reactions is that the surfaces were assumed to have equilibrated rapidly. This avoided the need for having a transient term for heat release due to surface reactions on the catalyst and electrolyte phase surfaces. It was found that the temperature gradients spiked to unreasonable values due to the inclusion of these transients and hence, the assumption mentioned here was used in order to achieve the steady state temperature profiles through the MEA. The simulation, however, slowed down considerably due to the non-isothermal effects. One sweep of 25 steady-state simulations (with the maximum i_{ext} of 0.97 A/cm^2) took almost 10 hours on a 3.0 GHz dual core processor.

Although the above temperature profiles may not be significant enough to affect performance (~ 1-2 K temperature difference due to reforming) through the MEA of a button cell, the importance of the non-isothermal model is highlighted when analyzed in two dimensional and stack models as discussed before. The almost non significant temperature profile in a 1-D model is expected as the cell geometries are such that a thickness of a mere millimeter through the depth of the MEA renders the conditions almost isothermal. Similar observation has been recorded by Zhu & Kee [55] where they report temperature differences through the MEA of the order of 1-2 K as well.

4.5 Summary of Results

Results obtained from the through-the-MEA model by adapting it for syngas provide a basis for understanding the effects of C-H-O microkinetics on Ni/YSZ

anodes. This helps in characterizing the performance of the cells observed during experiments. The model also lays the foundation for incorporating hydrocarbon reforming chemistry for smaller hydrocarbons like butane. Development of a 'leakage mechanism' allows the model to account for discrepancies observed in the OCV between experiments and the through-the-MEA model that assumes a perfectly dense electrolyte. Fits obtained from the leakage model have been shown to be in good agreement with the experimentally observed data (within χ^2 values of 0.03), thereby further enhancing the efficacy of the model to realistically predict the observed performance.

Study of the effects of micro-structural parameters like $\varphi_{g,anode}$, $\tau_{g,anode}$, and $l_{TPB,cathode}$ on performance provides a means of using the model as a design tool for fabricating MEAs that can provide acceptable power densities. Results of the parametric study indicate the importance of porous media transport with regard to the cell performance. Analysis of the polarization curve at the two extremes (near the OCV region and near the high current density regime (i_{ext} > 1 Amp/cm^2)) provides insight on which micro-structural parameters can contribute to the activation and polarization overpotentials. For example, higher $\varphi_{g,anode}$ and lower $\tau_{g,anode}$ can have a positive impact on the total activation overpotential. Likewise, greater $l_{TPB,cathode}$ positively impacts the cell performance by reducing the total concentration overpotential.

Chapter 5: Conclusions and Future Recommendations

The potential for SOFCs to operate on a variety of fuels including more conventional carbonaceous fuels coupled with SOFCs ability to achieved high energy conversion efficiency makes them an attractive option for many stationary and distributed power applications. However, commercialization of SOFCs requires adequate stability for long term operation (on the order of several 1000 hours) without significant degradation in performance. This requirement combined with the need to reduce cost for manufacturing / assembly presents a challenge for scientists and engineers working on their advancement. Conventional Ni/YSZ cermet anodes used in many current-day SOFC stacks are prone to carbon deposition inside the pores of the anode, and this leads to substantial degradation in performance. At operating temperatures of 700 to 800 °C, carbon deposition in Ni/YSZ anodes compromises the ability for SOFCs to operate with internal reforming of hydrocarbons fuels and perhaps even some syngas compositions with high carbon content. Therefore, a need to develop alternative material sets for SOFC anodes that can resist carbon build up inside the pores of the anode assumes great importance. CeO_2–containing anodes have gained much attention in this regard over recent years as a possible solution to the carbon-deposition and related stability problems. This chapter summarizes the results observed in the present study which aimed at exploring the impact on performance of Ni/CeO_2/YSZ anodes and provides conclusions and recommendations for future exploration in this subject.

5.1 Summary of Results

5.1.1 Experimental Results

With the fabrication protocols described in detail in chapter 2 and modified slightly from the earlier work of Jawlik [4], Ni/YSZ and Ni/CeO_2/YSZ anode support layers in SOFC button cells were made with repeatable micro-architectures and tested for various fuel compositions as described in chapter 3. The experimental rig set up was modified from the previous configurations tested by Jawlik [4] and success was demonstrated in achieving the results with good repeatability without the cells cracking (observed much more frequently in earlier configurations). The results obtained provide a basis for comparison between Ni/YSZ cells and their ceria-doped counterparts. Microstructures of these two types of cells were kept similar (especially electrolyte thickness, porosity, etc.) to facilitate comparison. It was found that the presence of CeO_2 in Ni/YSZ anode support layer led to higher power densities (by almost 20%) and reduced polarization resistances at high current densities when operating on syngas and direct butane/steam feeds (with internal reforming). With ceria added in the anode support layer, cell performance at current densities > 0.3 A/cm^2 improved due to a significant reduction in the polarization resistance by about 15% at total cell overpotential of 300 mV (as indicated by the reduction in slope of the *V-i* curves) compared to Ni/YSZ cell. The cause for this change in R_{pol} can be explained by a possible acceleration of water-gas-shift kinetics due on the ceria addition. Ceria/nickel composite promotes water-gas-shift at higher current densities, increasing the availability of H_2, thereby increasing cell performance. In addition to reduced R_{pol}, ceria doped cell showed a higher OCV compared to the Ni/YSZ cell,

although this could be caused due to more leakage is Ni/YSZ than in the ceria doped cell.

Long term stability tests with the direct butane/steam feeds were performed for cells with and without CeO_2 added to the anode support layer. For a fixed overpotential, the cells with CeO_2 addition showed much slower degradation along with improved performance. The ceria-containing cells showed superior resistance towards carbon deposition, and testing with direct butane/steam feeds of the ceria-containing cells for over 40 hours showed greatly reduced reduction in the observed current density for a fixed value of overpotential. Whereas Ni/YSZ anodes showed almost no power dentistry after 20 hours of constant overpotential with direct butane feeds, the Ni/CeO_2/YSZ continued to provide power with loss after 40 hours of testing. Post-test characterization showed that Ni/YSZ anodes suffered severe structural degradation likely due to carbon build-up within the pores. Such degradation was not observed in case of the ceria-containing cells. SEM imaging and depth profiling with Raman Spectroscopy revealed that the ceria greatly reduced penetration depth of graphite into the porous support layer. XRD showed furthermore the presence of cerium zirconates which have been reported to be stable and catalytically active under redox conditions at high temperatures [44].

5.1.2 Modeling Results

A “through the MEA” model with detailed electrochemistry and porous media multi-species gas transport developed by Decaluwe et al. [38] was modified and expanded in this study to simulate syngas flow conditions used in the experimental

studies described in chapter 3. The model, described in more detail in chapter 4, was modified to include charge transfer reactions for CO electrochemical oxidation in the TPB region in addition to H_2. A "leakage model" mechanism was developed inside the existing code to account for the discrepancies observed in the OCV between the experimental results and what the model predicted (based on the assumption that the electrolyte was fully dense with no leakage). A "pinhole" mechanism was developed that simulates the leakage of oxygen from the cathode to the anode functional layer where direct oxidation results in lower reactant and increased product partial pressures. This allows for the model to match the OCV observed during experiments.

In order to fit the experimental data, a number of micro-structures were explored through the model by changing parameters like anode support layer tortuosity, porosity and the cathode functional layer parameters like the three phase boundary length and the catalyst loading. A baseline fit was run for the case of H_2:Ar (1:1) ratio) with 3% H_2O and a particular geometry was arrived at. This formed the basis for fitting syngas data. The results predicted by the model are in good agreement with the experimental data.

The model was also modified to include energy equations to explore the non-isothermal effects of steam reforming for methane. For these 1-D simulations, results indicate an isothermal temperature profile (to within ± 2 °C) through the ~ 1 mm thick MEA. The importance of the non-isothermal model will only be borne in axial gradients in a down the channel 2-D configuration, where a significantly varying temperature profile can affect the performance of the cell.

5.2 Future Recommendations

It has been demonstrated that the cell MEAs with relatively high porosities (~ 60% for the anode support layer) can be tested without cells cracking during the experiments with the setup in this study for several days of testing. With the cells performing as expected for various fuel compositions, the framework is in place for long term stability testing of these MEAs. Results observed in this study indicate that it is of critical importance to maintain steady steam flows with good humidifier temperature control when using direct hydrocarbon/steam feeds for SOFC anodes. Inability of the current equipment to do so and the possibility of steam condensation inside the gas supply lines leading to anode feed tube results in steam being supplied in bursts. This is manifested as periodic oscillations of current density (for a fixed overpotential). Also, the temperature fluctuations (± 2 °C) from the desired temperature values result in variable S/C ratio during stability testing. It is therefore imperative that the humidifiers be maintained at constant temperatures (and with adequate insulation) to be able to conduct stability tests over long time periods.

For the non-isothermal model is concerned, the need to extend the existing model into a down the channel model is critical in understanding how the endothermic steam reforming of hydrocarbons impacts the cell performance (and carbon deposition). With the energy equations implemented in the current 1-D model, the framework is in place to extend the domain into 2-D down the channel configuration.

Finally, as the motivation for this study is derived from the possible use of petroleum off gases as fuel in the SOFC MEAs, it is logical to extend the current

testing protocols to incorporate impurities in the fuel stream such as sulfides and chlorides (which exist in small but significant quantities in off-gases) and study their impact on performance. Role of ceria in the SOFC anode (both support layer as well as functional layer) can be further substantiated if such tests indicate how ceria can provide both carbon and sulfur tolerant anodes that can function with minimal degradation over long periods of time.

Glossary of Symbols

A	Pre-exponential
B_g	Porous electrode permeability
an	Subscript used to denote the anode
a_m	Surface area of phase m (catalyst or electrolyte) per unit volume
ca	Subscript used to denote the cathode
C_{dl}	Double layer capacticance for composite electrode, per unit total volume.
$D_{DGM,kl}$	Effective binary Dusty Gas Model diffusion coefficients
$D^e_{kn,l}$	Effective Knudsen diffusion coefficient for species l
D^e_{kl}	Effective multi-component binary diffusion coefficient for species k and l
$D_{k,mix}$	Mixture-averaged diffusion coefficient for gas-phase species k
$D_{pinhole}$	Effective diffusion coefficient of oxygen through the electrolyte Pinhole
d_p	Average particle diameter of porous electrode
δ_m	Total thickness of element m
δ_{util}	Utilization thickness
E_a	Activation energy
F	Faraday's constant
G_k	Gibbs free energy for species k
$G°$	Standard-state Gibbs free energy

ΔG_f^o	Gibbs free energy of formation at atmospheric pressure
H	Enthalpy
h^0_k	Standard-state molar enthalpy of species k
i	Current density
i_o	Exchange current density
i_{O2-}	Ionic current due to oxide ion transport in ceria bulk
i_{leak}	Leakage current
i_l	Limiting current density
i_{Far}	Faradaic current
$J_{g,k}$	Diffusive mass flux of gas-phase species k
Kn	Knudsen number
l_{TPB}	Length of three-phase boundary, per unit total electrode volume
Nu	Nusselt number
n_{el}	Number of electrons exchanged in a specified reaction
$\dot{n_{O_2}}$	Molar flux of O_2
P_k	Partial pressure of species k
ρ	Density
φ_g	Porosity
ϕ	Phase difference between voltage and current signals
Φ_{cell}	Cell electric potential
Φ_{cat}	Electric potential of local catalyst phase
$\Phi_{electrolyte}$	Electric potential of local electrolyte phase

$\Delta\Phi_{el}$	Electric potential difference between local catalyst and electrolyte phases
$\theta_{k,m}$	Surface coverages for species k on phase m (electrolyte or catalyst)
$\bar{R}$	Universal gas constant
r_p	Average pore radius of porous electrode
R_{bulk}	Bulk resistance
R_{pol}	Polarization resistance
S	Entropy
Sh	Sherwood number
$\dot{s}_{k,m}$	Net molar production rate of gas-phase species k from heterogeneous surface reactions on phase m
σ_{elec}	Electronic conductivity
σ^e	Effective conductivity
t	Time
T	Temperature
T_{cell}	Cell Temperature
Γ_m	Available surface sites per unit area of phase m
τ_g	Tortuosity
V_{rev}	Nernst Voltage
V_{cell}	Cell Operating Voltage
V_{OCV}	Open Circuit Voltage
W_k	Molecular weight of species k
ν_k	Net stoichiometric coefficient for species k for the global half-cell

	reaction
$v_{i,k}$	Net stoichiometric coefficient for species *k* for reaction *i*
$v'_{i,k}$	Stoichiometric coefficient for species *k* in forward reaction *i*
$v''_{i,k}$	Stoichiometric coefficient for species *k* in reverse reaction *i*
q_i	Rate-of-progress for reaction *i*
X_k	Mole fraction of species *k*
$[X_l]$	Molar concentration of species *l*
Z	Impedance
Z_0	Magnitude of the Impedance
Z'	Real component of the impedance
Z''	Imaginary component of the impedance
β_f	Forward reaction charge transfer coefficient
β_r	Reverse reaction charge transfer coefficient
η_{act}	Activation overpotential
η_{conc}	Concentration overpotential
η_{ohm}	Ohmic overpotential
η_{tot}	Total overpotential
ζ_k	Number of surface sites occupied by species k
μ	Mixture dynamic viscosity
λ_{gas}	Thermal conductivity of the gas phase
λ_{solid}	Thermal conductivity of the catalyst substance
λ_{int}	Effective conductivity at the interface between the flow channel and the first GDL layer

Bibliography

1. R. N. Singh, *Sealing Technology for Solid Oxide Fuel Cells*; International Journal of Applied Ceramic Technology, 2007, 4(2)
2. Sasaki et al., *Fuel Impurity Tolerance of Solid Oxide Fuel Cells;* 10th International Symposium on Solid Oxide Fuel Cells (SOFC-X), 2007, 7(1)
3. Larminie and Dicks, *Fuel Cell Systems Explained*; 2nd Edition John Wiley & Sons, 2003
4. Paul Jawlik, *EFFECTS OF CERIA ADDITION ON NICKEL/YSZ ANODES IN SOLID OXIDE FUEL CELLS OPERATING ON HYDROGEN AND SYNGAS FUEL FEEDS*; University of Maryland (2008)
5. Koh, Y.H., *Design and fabrication of three-dimensional solid oxide fuel cells*; Journal of Power Sources, 2006, 161(2)
6. Han et al., *Fabrication and properties of anode-supported solid oxide fuel cells;* Solid State Ionics, 2008, 179
7. Várez et al., *Microstructure, mechanical and electrical properties of Ni-YSZ anode supported solid oxide fuel cells;* Archives of Materials Science and Engineering, 2008, 32 (1)
8. Chang et al, *Characterization of warpage behaviour of Gd-doped ceria/NiO–yttria stabilized zirconia bi-layer samples for solid oxide fuel cell application;* Journal of Power Sources, 2008, 185
9. Armstrong, T.J. and J.G. Rich, *Anode-supported solid oxide fuel cells with La0.6Sr0.4CoO3-lambda-Zr0.84Y0.16O2-delta composite cathodes fabricated by an infiltration method;* Journal of The Electrochemical Society, 2006, 153(3)
10. M. B. Pomfret, J. Marda, G. S. Jackson, B. W. Eichhorn, A.M. Dean, R.A. Walker, *Hydrocarbon Fuels in Solid Oxide Fuel Cells: In Situ Raman Studies of Graphite Formation and Oxidation;* J. Phys. Chem. C, 2008, 112
11. R.J. Kee, H. Zhu, A.M. Sukeshini, G.S. Jackson, *Solid Oxide Fuel Cells: Operating Principles, Current Challenges, and the Role of Syngas;* Combustion Science and Technology, 2008, 180(6)
12. R. J. Gorte, J. M. Vohs, *Novel SOFC anodes for the direct electrochemical oxidation of hydrocarbons;* Journal of Catalysis, 2003, 216(1-2)
13. S. F. Corbin, R. M. Clemmer, Q. Yang, *Development and Characterization of SOFC NI-YSZ Anodes Using Highly Porous NI Foam;* Ceramic Engineering and Science Proceedings, 2008, 26(4),
14. Z. Cheng and M.L. Liu, *Characterization of sulfur poisoning of Ni–YSZ anodes for solid oxide fuel cells using in situ Raman microspectroscopy;* Solid State Ionics, 2007, 178, (13-14)
15. Yoshio and I. Yasuda, *The poisoning effect of sulfur-containing impurity gas on a SOFC anode: Part I. Dependence on temperature, time, and impurity concentration*; Solid State Ionics, 2000, 132(3-4)
16. A. Atkinson, S. Barnett, R.J. Gorte, J.T.S. Irvine, A.J. McEvoy, M. Mogensen, S. Singhal, and J. Vohs, *Advanced anodes for high-temperature fuel cells*; Nat. Mater., 2004, 3

17. R. Ormerod, *Fuels and Fuel Processing, in High Temperature Solid Oxide Fuel Cells: Fundamentals, Design, and Applications;* S.C. Singhal and K. Kendell, Editors, 2003, Elsevier Ltd.: Bodmin.
18. Lin et al., *Direct operation of solid oxide fuel cells with methane fuel;* Solid State Ionics, 2005, 176(23-24)
19. E. Perry Murray, T. Tsai, and S.A. Barnett, *A direct-methane fuel cell with a ceria-based anode;* Nature, 1999, 400
20. S. Park, J.M. Vohs, and R.J. Gorte, *Direct oxidation of hydrocarbons in a solid-oxide fuel cell;* Nature, 2000, 404
21. K. Haga, S. Adachi, Y. Shiratoria, K. Itoha and K. Sasaki, *Poisoning of SOFC anodes by various fuel impurities*; Solid State Ionics, 2008, 179(27-32)
22. D. Dees, U. Balachandran, S. Doris, J. Heiberger, C. McPheeter, J. Picciolo, *Electrochemical Society Proceedings of the First International Symposium on Solid Oxide Fuel Cells*, 89(11)
23. S. Zhab, Z. Chengb, J. Winnick, M. Liu, L. Aguilar, *A solid oxide fuel cell operating on hydrogen sulfide (H_2S) and sulfur-containing fuels*; Journal of Power Sources, 2004, 135
24. O.A. Marina, L.R. Pederson, in: J. Huijsmans (Ed.), *Fifth European Solid Oxide Fuel Cell Forum, European Fuel Cell Forum*, Oberrohfdorf, Switzerland, 2002
25. Gorte et al., *Enhanced Thermal Stability of SOFC Anodes Made with CeO2-ZrO2 Solutions*; Electrochemical and Solid-State Letters, 2005, 8(8)
26. Suna & Stimming, *Recent anode advances in solid oxide fuel cells;* Journal of Power Sources, 2007, 171
27. C.W. Sun, J. Sun, G.L. Xiao, H.R. Zhang, X.P. Qiu, H. Li, L.Q. Chen, J. Phys. Chem. B 110 (2006)
28. N.V. Skorodumova, S.I. Simak, B.I. Lundqvist, I.A. Abrikosov, B. Johansson, Phys. Rev. Lett. 89 (2002)
29. Gorte, et al., *Anodes for direct oxidation of dry hydrocarbons in a solid oxide fuel cell;* Advanced Materials, 2000, 12(19)
30. Park et al., *Direct oxidation of hydrocarbons in a solid oxide fuel cell I. Methane oxidation;* Journal of The Electrochemical Society, 1999, 146(10)
31. Z.L. Zhan and S.A. Barnett, *An Octane-Fueled Solid Oxide Fuel Cell;* Science, 2005, 308
32. B.D. Madsen and S.A. Barnett, *Effect of fuel composition on the performance of ceramic-based solid oxide fuel cell anodes;* Solid State Ionics, 2005, 176
33. H. Zhu, R.J. Kee, V. Janardhanan, O. Deutschmann, D. Goodwin, *Modeling Elementary Heterogeneous Chemistry and Electrochemistry in Solid-Oxide Fuel Cells*; Journal of The Electrochemical Society, 2005, 152(12)
34. Bessler, Warnatz & Goodwin, *The influence of equilibrium potential on the hydrogen oxidation kinetics of SOFC anodes*; Solid State Ionics, 2007, 177
35. Morel, Laurencin, Bultel, Lefebvre-Jouda, *Anode-Supported SOFC Model Centered on the Direct Internal Reforming*; Journal of The Electrochemical Society, 2005, 152(7)

36. V. Janardhanan, O. Deutschmann, *CFD analysis of a solid oxide fuel cell with internal reforming: Coupled interactions of transport, heterogeneous catalysis and electrochemical processes*; Journal of Power Sources, 2006, 162(2)
37. V. Janardhanan, O. Deutschmann, *Numerical study of mass and heat transport in solid-oxide*; Chemical Engineering Science, 2007, 62
38. S. DeCaluwe, H. Zhu, R.J. Kee, G.S. Jackson, *Importance of Anode Microstructure in Modeling Solid Oxide Fuel Cells*; Journal of The Electrochemical Society, 2008, 155(6)
39. F. Zhao, A.V. Virkar, *Dependence of polarization in anode-supported solid oxide fuel cells on various cell parameters;* Journal of Power Sources, 2005, 141(1)
40. www.eia.doe.gov/emeu/cabs/Kuwait/Full.html
41. X. Wang and R.J. Gorte, *Steam reforming of n-butane on Pd/ceria*; Catalysis Letters, 2001, 73(1)
42. Sammes, Boersma & Tompsett, *Micro-SOFC system using butane fuel*; Solid State Ionics, (2000), 135
43. He, Vohs & Gorte, *Effect of Synthesis Conditions on the Performance of Cu-CeO2-YSZ Anodes in SOFCs*; Journal of the Electrochemical Society, 2003, 150(11)
44. M. Mogensen, *Ceria-based Electrodes, in Catalysis by Ceria and Related Mateials*, A. Trovarelli, Editor. (2002), London: Imperial College Press
45. Terribile et al., *Catalytic combustion of hydrocarbons with Mn and Cu-doped ceria–zirconia solid solutions*; Catalysis Today, 1999, 47
46. Y. Jiang, S.Z. Wang, Y.H. Zhang, J.W. Yan, and W.Z. Li, *Electochemical reduction of oxygen on a strontium doped lanthanum manganite electrode;* Solid State Ionics, 1998, 110(1-2)
47. S.B. Adler, *Factors governing oxygen reduction in solid oxide fuel cell cathodes;* Chem. Rev., 2004, 104(10)
48. K. Sasaki, and J. Maier, *Re-analysis of defect equilibria and transport parameters in Y2O3-stabilized ZrO2 using EPR and optical relaxation;* Solid State Ionics, 2000, 134(3-4)
49. K. Sasaki, and Y. Teraoka, *Equilibria in fuel cell gases - I. Equilibrium compositions and reforming conditions;* J. Electrochem. Soc., 2003, 150
50. Gorte et al., *An Examination of SOFC Anode Functional Layers Based on Ceria in YSZ;* Journal of The Electrochemical Society, 2007, 154(7)
51. Wang et al., *Improved SOFC performance with continuously graded anode functional layer;* Electrochemistry Communications, 2009, 11(6)
52. Suzuki et al., *Impact of Anode Microstructure on Solid Oxide Fuel Cells*; Science, 2009, 325
53. Lanzini et al., *Microstructural characterization of solid oxide fuel cell electrodes by image analysis technique;* Journal of Power Sources, 2009, 194
54. H. Zhu, A. M. Colclasure, R. J. Kee, Y. B. Lin, and S. A. Barnett, *Anode barrier layers for tubular solid-oxide fuel cells with methane fuel streams;* J. Power Sources, 2006, 161

55. Zhu & Kee, *Modeling Distributed Charge-Transfer Processes in SOFC Membrane Electrode Assemblies;* Journal of The Electrochemical Society, 2008, 155(7),
56. Adler et al., *Electrode Kinetics of Porous Mixed-Conducting Oxygen Electrodes;* J. Electrochem. Soc., 1996, 143(11)
57. Chan & Xia, *Anode Micro Model of Solid Oxide Fuel Cell;* Journal of The Electrochemical Society, 2001, 148 (4)
58. Steven Decaluwe, *QUANTIFYING THE ROLE OF CERIA AS A CATALYST IN SOLID OXIDE FUEL CELL ANODES*; University of Maryland (2009)
59. H. Zhu, R. J. Kee, *A general mathematical model for analyzing the performance of fuel-cell membrane-electrode assemblies*; Journal of Power Sources, 2003, 117
60. D. G. Goodwin, www.cantera.org
61. D. Goodwin, *Solid Oxide Fuel Cells IX.*, The Electrochemical Society Proceedings Series, 2005
62. Williford, Chick, Maupin, Simner and J. W. Stevenson, *Diffusion Limitations in the Porous Anodes of SOFCs*; Journal of the Electrochemical Society, 2003, 150(8)
63. Janardhanan, Heuveline & Deutschmann, *Three-phase boundary length in solid-oxide fuel cells: A mathematical model*; Journal of Power Sources, 2008, 178 (1)
64. Y. Jiang, *Fuel composition and diluent effect on gas transport and performance of anode-supported SOFC;* Journal of The Electrochemical Society, 2003, 150(7)
65. Marinsek et al., *Ni–YSZ SOFC anodes—Minimization of carbon deposition*; Journal of the European Ceramic Society, 2007, 27
66. Menzler et al., *Characterisation of Ni-YSZ-Cermets with Respect to Redox Stability*; Fuel Cells, 2007, 7(5)
67. R.J. Kee, H. Zhu, and G.S. Jackson, "Solid oxide fuel cells using syngas," in Gas synthesis combustion: fundamentals and applications, Eds., T.C. Lieuwen and V. Yang, Taylor and Francis, London, in press (2009)
68. R.E. Meredith, C.W. Tobias, *Advances in Electrochemistry and Electrochemical Engineering*, (2); Interscience Publishers, New York, 1962
69. A. M. Sukeshini, B. Habibzadeh, B. P. Becker, C. A. Stoltz, B. W. Eichhorn and G. S. Jackson, *Electrochemical Oxidation of H, CO, and CO/ H Mixtures on Patterned Ni Anodes on YSZ Electrolytes;* Journal of the Electrochemical Society, 2006, 153(4)